

Impact of Retarder-Induced Roughness on Shear Friction Capacity using
Conventional and High-Strength Reinforcement

Stephan Ahn

A thesis
submitted in partial fulfilment of the
requirements for a degree of

Master of Science in Civil Engineering

University of Washington
2020

Committee:

Paolo M. Calvi

Dawn E. Lehman

Marc O. Eberhard

Program Authorized to Offer Degree:
Civil and Environmental Engineering

© Copyright 2020
Stephan Ahn

University of Washington

Abstract

Impact of Retarder-Induced Roughness on Shear Friction Capacity using
Conventional and High-Strength Reinforcement

Stephan Ahn

Co-Chairs of the Supervisory Committee:

Paolo M. Calvi

Civil and Environmental Engineering

Dawn E. Lehman

Civil and Environmental Engineering

Shear friction is used to transfer shear forces between two reinforced concrete members or two members with dissimilar materials. Shear transfer across a plane represents a complex phenomenon that depends on the interactions between several variables, such as concrete surface condition and cohesion, concrete strength, and steel reinforcement strength and reinforcement ratio. Prior research has focused on surface condition as well as properties of the reinforcing steel. However, these data have not provided conclusive results. Although it is clear that roughening the interface of a cold-joint contributes to increase its the shear-transfer capacity, the roughening methods currently used in practice are labor intensive. In addition, the ACI code prohibits the use of high strength steel reinforcement. To investigate these parameters methodically, an experimental research program was undertaken. The test matrix included 24 cold-joint specimens. Of those, half had untreated (“or smooth”) interface, while half were intentionally roughened using a surface retarder. Different types of retarder were investigated

separately to ensure minimum roughness depth. The test series also investigated the impact of parameters such as steel reinforcement strength and reinforcement ratio. More specifically, for different specimens, varying amount of grade 60 and grade 80 steel reinforcing bar were used across the cold-joint interface. The experimental results indicated the following: (1) roughening the interface increases the shear-transfer capacity of the joint, (2) using the recommended retarder is an economical and structurally reliable method to achieve a roughened interface, (3) the reinforcement does not yield at the peak load and therefore, increasing the strength of the reinforcement does not provide a corresponding increase in shear-transfer capacity, and (4) increasing the reinforcement ratio has a more significant impact on the smooth-surface specimens. The results were compared with the shear friction design equations currently reported in the ACI code and in the American Association of State Highway Transportation Officials (AASHTO). The comparison indicated that both codes underestimate the shear friction capacity of cold-joint specimens with low reinforcement ratios, and that AASHTO code overestimates the shear friction capacity of roughened cold-joint specimens with high reinforcement ratios. Incorporating this data into a previously compiled shear-friction database, a new shear friction equation was proposed. The new equation has a separate cohesion term that separates the contributions of the steel reinforcement and cohesion and includes has higher strength upper limits for smooth-surface specimens and lower strength upper limits for roughened specimens.

Acknowledgements

I would like to first thank my advisors, Professor Paolo Calvi and Professor Dawn Lehman for their mentorship, sacrifice, support, and guidance throughout this research project. It was an incredible experience working with these two amazing advisors. I would also like to thank Professor Marc Eberhard for serving on of my committee and for giving me great feedback.

I would like to thank Vince Chaijaroen for making everything else possible. I was able to feel comfortable and fully enjoy my experience in the lab because of Vince. I am very grateful that I had the chance to get to know him personally. I would also like to thank Ken Sullivan, Danielle Voytko, Younis Riyami, Ben Terry, Alec Yeutter, Caleb Trapp, Sam Turner, Austin Anderson, Michelle Chang, and Chris Pyke for helping me in the lab. I was able to become great friends with all of them and that alone made this research experience worth it.

I would like to thank Concrete Research Council of American Concrete Institute for providing me with funding and project guidance.

Most importantly, I want to thank my family and friends for getting me to where I am today.

Table of Contents

Acknowledgements.....	5
List of Figures.....	8
List of Tables.....	16
Notation List.....	18
Chapter 1: Introduction.....	20
1.1 Research Impetus.....	20
1.2 Research Objectives and Approach.....	22
1.3 Overview of Report.....	23
Chapter 2: Current Shear Friction Provisions and Literature Review.....	24
2.1 Shear Friction Theory and Code Provisions.....	24
2.1.1 Shear Friction Theory.....	24
2.1.2 ACI Shear Friction Provision.....	27
2.1.3 AASHTO Shear Friction Provisions.....	29
2.2 Overview of Relevant Experimental Programs.....	31
2.2.1 Bass, Carrasquillo, and Jirsa (1989).....	33
2.2.2 Kono, Tanaka, and Watanabe (2000).....	36
2.2.3 Kahn and Mitchell (2002).....	38
2.2.4 Shaw and Sneed (2014).....	40
2.2.5 Harries, Zeno, and Shahrooz (2012).....	42
2.2.6 Barbosa, Trejo, and Nielsen (2017).....	43
2.3 Findings and Summary.....	45
Chapter 3: Experimental Design.....	46
3.1 Test Matrix.....	47
3.2 Specimen Design.....	49
3.2.1 Concrete Material Properties.....	54
3.2.2 Reinforcement Material Properties.....	54
3.3 Test Setup.....	55
3.4 Instrumentation.....	57
3.4.1 Strain Gauge.....	58
3.4.2 String Potentiometers and Duncan Potentiometers.....	59
3.4.3 Optotrak.....	60
Chapter 4: Experimental Results.....	62
4.1 Testing Procedure.....	64

4.2 Typical Specimen Behavior	64
4.3 Individual Specimen Behavior.....	65
4.3.1 Test Series 0: Specimens without Reinforcement	65
4.3.2 Test Series 60S: Specimens with 60 ksi Reinforcement Crossing a Smooth Interface.....	71
4.3.3 Test Series 80S: Specimens with 80 ksi Reinforcement Crossing a Smooth Interface.....	90
4.3.4 Test Series 60R:Specimens with 60 ksi Reinforcement Crossing a Roughened Interface	110
4.3.5 Test Series 80R: Specimens with 80 ksi Reinforcement Crossing a Roughened Interface	126
4.4 Summary of the Experimental Results	142
Chapter 5: Data Analysis	143
5.1 The Influence of Roughness	143
5.1.1 Peak Shear-Transfer Capacity.....	143
5.1.2 Slip Displacement and Crack Width.....	149
5.2 Influence of Reinforcement Ratio and Yield Strength	151
5.2.1 Peak Shear-Transfer Capacity.....	151
5.2.2 Post-peak Shear-Transfer Capacity.....	158
Chapter 6: Evaluation of ACI, AASHTO, and Proposed Shear Friction Provisions.....	160
6.1 Evaluation of the Current ACI and AASHTO Shear Friction Provisions with UW Specimens	161
6.2 Evaluation of the Current ACI and AASHTO Shear Friction Provisions with the Database	167
6.3 Evaluation of Other Shear Friction Models	170
6.4 Proposed Shear Friction Model	175
Chapter 7: Summary, Conclusion and Future Recommendation.....	178
7.1 Summary	178
7.2 Conclusions.....	179
7.3 Recommendations for Future Works: Interface Shear Transfer	181
References.....	182
Appendix A: Figures and Tables	184

List of Figures

Figure 1.1: Examples of interface shear transfer in a structure [21].....	20
Figure 2.1: Simplified shear friction mechanism originally drawn by Birkeland and Birkeland [8] (taken from Harries et al. [12])	25
Figure 2.2: Figure 2 from Davaadorj et al. [10]. Frequency distribution of tests as a function of main parameters.	32
Figure 2.3: Fig. 2 from Bass et al. [7]. Details of the specimen. Base-block and wall reinforcement.	34
Figure 2.4: Fig. 7 from Bass et al. [7]. Test frame.....	34
Figure 2.5: Fig 3.3 and 3.4 from Barbosa [6]. Test elevation for specimens No.4 (left) and No.5 (right) reinforcing bars.....	44
Figure 3.1: Drawing of a specimen with typical reinforcement details. Grey region in Section cut A-A is the interface region. Section cut B-B shows dimension of the interface reinforcement. ..	50
Figure 3.2: Specimen treated with Grade 15 retarder	51
Figure 3.3: Specimen treated with Grade 150 retarder	51
Figure 3.4: Photograph showing the first half of the specimen being casted and the interface being treated with surface retarders.	52
Figure 3.5: Photograph of an untreated surface.	52
Figure 3.6: Photograph of a surface treated with surface retarder.	53
Figure 3.7: Photograph of UW60R-8.....	53
Figure 3.8: Stress-strain plot of the steel reinforcement	55
Figure 3.9: Test Setup (Plan View).....	56
Figure 3.10: Test Setup (Elevation View, East side)	56
Figure 3.11: Picture of the test setup. The wide flange beam was anchored down with two C-channels.....	57
Figure 3.12: Photograph of the actuator head.	57
Figure 3.13: Drawing of the test setup with instrumentations (Elevation view, East side).	58
Figure 3.14: String potentiometer attached to the reaction block.....	59
Figure 3.15: Duncan potentiometers used during the test.....	59

Figure 3.16: Plot comparing the displacement readings from the Optotrak markers and string potentiometer.	60
Figure 3.17: Drawing of the test setup with Optotrak LED markers and designated marker numbers (Elevation view, West side).	61
Figure 3.18: Picture of a specimen with LED markers (West side)	61
Figure 4.1: UW0S load-slip displacement graph (top) and load-crack width graph (bottom). The letters in the graphs reference different stages and photographs in Figure 4.2.....	65
Figure 4.2: Photographs of UW0S during the test: a) start of test (top), and b) end of test (bottom).	66
Figure 4.3: Photograph of the interface after test (UW0S).....	67
Figure 4.4: UW0R load-slip displacement graph (top) and load-crack width graph (bottom). The letters in the graphs reference different stages and photographs in Figure 4.5.....	68
Figure 4.5: Photographs of UW0R during the test: a) start of test (top), and b) end of test (bottom).	69
Figure 4.6: Photograph of the interface after test (UW0R)	70
Figure 4.7: UW60S-2 load-count graph. The letters on the graph reference different stages and photographs in Figure 4.8.	71
Figure 4.8: Photographs of UW60S-2 at different stages of the tests: a) start of test b) peak c) residual d) end of test. The average strain-gauge value at peak load is included in the photographs.	72
Figure 4.9: Close up of the revealed reinforcement after test (UW60S-2 West side).	73
Figure 4.10: Close up of the revealed reinforcement after test (UW60S-2 East side).....	73
Figure 4.11: UW60S-4 load-slip displacement (top) and load-crack width graph (bottom). The letters in the graphs reference different stages and photographs in Figure 4.12.....	75
Figure 4.12: Photographs of UW60S-4 at different stages of the tests: a) start of test b) peak c) residual d) end of test. The average strain-gauge value at peak and at residual are included in the photographs.....	76
Figure 4.13: Close up of the revealed reinforcement after test (UW60S-4 East side).....	77
Figure 4.14: Close up of the revealed reinforcement after test (UW60S-4 West side).	77
Figure 4.15: UW60S-6 load-slip displacement (top) and load-crack width graph (bottom). The letters in the graphs reference different stages and photographs in Figure 4.16.....	78

Figure 4.16: Photographs of UW60S-6 at different stages of the tests: a) start of test b) peak load c) residual d) end of test. The average strain-gauge value at peak load and at residual are included in the photographs.....	79
Figure 4.17: Photograph of the revealed reinforcement after test (UW60S-6 East side).	80
Figure 4.18: Revealed reinforcement after test (UW60S-6 West side).	80
Figure 4.19: UW60S-6 load-slip displacement (top) and load-crack width graph (bottom). The letters in the graphs reference different stages and photographs in Figure 4.20.....	81
Figure 4.20: Photographs of UW60S-8 at different stages of the tests: a) start of test b) peak load c) residual d) end of test. The average strain-gauge value at peak load and at residual are included in the photographs.....	82
Figure 4.21: Close up of the revealed reinforcement after test (UW60S-8 East side).....	83
Figure 4.22: Close up of the revealed reinforcement after test (UW60S-8 West side).	83
Figure 4.23 UW60S-10 load-slip displacement (top) and load-crack width graph (bottom). The letters in the graphs reference different stages and photographs in Figure 4.24.....	84
Figure 4.24: Photographs of UW60S-10 at different stages of the tests: a) start of test b) peak c) residual d) end of test. The average strain-gauge value at peak and at residual are included in the photographs.....	85
Figure 4.25: Photograph of the revealed reinforcement after test (UW60S-10 East side).	86
Figure 4.26 UW60S-12 load-slip displacement (top) and load-crack width graph (bottom). The letters in the graphs reference different stages and photographs in Figure 4.27.....	87
Figure 4.27: Photographs of UW60S-12 at different stages of the tests: a) start of test b) peak c) residual d) end of test. The average strain-gauge value at peak and at residual are included in the photographs.....	88
Figure 4.28: Photograph of the revealed reinforcement after test (UW60S-12 East side).	89
Figure 4.29: UW80S-2 load-count graph. The letters in the graph reference different stages and photographs in Figure 4.30.	90
Figure 4.30: Photographs of UW80S-2 at different stages of the tests: a) start of test b) peak c) residual d) end of test. The average strain-gauge value at peak and at residual are included in the photographs.....	91
Figure 4.31: Photograph of the revealed reinforcement after test (UW80S-2 East side).	92
Figure 4.32: Close up of the revealed reinforcement after test (UW80S-2 West side).	92

Figure 4.33 UW80S-4 load-slip displacement (top) and load-crack width graph (bottom). The letters in the graphs reference different stages and photographs in Figure 4.34.....	94
Figure 4.34: Photographs of UW80S-4 at different stages of the tests: a) start of test b) peak c) residual d) end of test. The average strain-gauge value at peak and at residual are included in the photographs.....	95
Figure 4.35: Close up of the revealed reinforcement after test (UW80S-4 East side).....	96
Figure 4.36: Close up of the revealed reinforcement after test (UW80S-4 West side).	96
Figure 4.37: UW80S-6 load-slip displacement (top) and load-crack width graph (bottom). The letters in the graphs reference different stages and photographs in Figure 4.38.....	97
Figure 4.38: Photographs of UW80S-6 at different stages of the tests: a) start of test b) peak c) residual d) end of test. The average strain-gauge value at peak and at residual are included in the photographs.....	98
Figure 4.39: Close up of the revealed reinforcement after test (UW80S-6 West side).	99
Figure 4.40 UW80S-8 load-slip displacement (top) and load-crack width graph (bottom). The letters in the graphs reference different stages and photographs in Figure 4.41.....	100
Figure 4.41: Photographs of UW80S-8 at different stages of the tests: a) start of test b) peak c) residual d) end of test. The average strain-gauge value at peak and at residual are included in the photographs.....	101
Figure 4.42: Close up of the revealed reinforcement after test (UW80S-8 East side).....	102
Figure 4.43: Photograph of the revealed reinforcement after test (UW80S-8 West side).	102
Figure 4.44: UW80S-10 load-slip displacement (top) and load-crack width graph (bottom). The letters in the graphs reference different stages and photographs in Figure 4.45.....	103
Figure 4.45: Photographs of UW80S-10 at different stages of the tests: a) start of test b) peak c) residual d) end of test. The average strain-gauge value at peak and at residual are included in the photographs.....	104
Figure 4.46: Photograph of the revealed reinforcement after test (UW80S-10 East side).	105
Figure 4.47: UW80S-12 Load-slip displacement (top) and load-crack width graph (bottom). The letters in the graphs reference different stages and photographs in Figure 4.48.....	107
Figure 4.48: Photographs of UW80S-12 at different stages of the tests: a) start of test b) peak c) residual d) end of test. The average strain-gauge value at peak and at residual are included in the photographs.....	108

Figure 4.49: Photograph of the revealed reinforcement after test (UW80S-12 East side).	109
Figure 4.50: UW60R-4 Load-slip displacement (top) and load-crack width graph (bottom). The letters in the graphs reference different stages and photographs in Figure 4.51.....	111
Figure 4.51: Photographs of UW60R-4 at different stages of the tests: a) start of test b) peak c) residual d) end of test. The average strain-gauge value at peak and at residual are included in the photographs.....	112
Figure 4.52: Photograph of the revealed reinforcement after test (UW60R-4 East side).....	113
Figure 4.53: Photograph of the revealed reinforcement after test (UW60R-4 West side).	113
Figure 4.54: UW60R-6 Load-slip displacement (top) and load-crack width graph (bottom). The letters in the graphs reference different stages and photographs in Figure 4.55.....	114
Figure 4.55: Photographs of UW60R-6 at different stages of the tests: a) start of test b) peak c) residual d) end of test. The average strain-gauge value at peak and at residual are included in the photographs.....	115
Figure 4.56: Close up of the revealed reinforcement after test (UW60R-6 West side).....	116
Figure 4.57: Photograph of the visible damage after test (UW60R-6 East side).....	116
Figure 4.58: UW60R-8 Load-slip displacement (top) and load-crack width graph (bottom). The letters in the graphs reference different stages and photographs in Figure 4.59.....	117
Figure 4.59: Photographs of UW60R-8 at different stages of the tests: a) start of test b) peak c) residual d) end of test. The average strain-gauge value at peak and at residual are included in the photographs.....	118
Figure 4.60: Close up of the revealed reinforcement after test (UW60R-8 East side).	119
Figure 4.61: UW60R-10 Load-slip displacement (top) and load-crack width graph (bottom). The letters in the graphs reference different stages and photographs in Figure 4.62.....	120
Figure 4.62: Photographs of UW60R-10 at different stages of the tests: a) start of test b) peak c) residual d) end of test. The average strain-gauge value at peak and at residual are included in the photographs.....	121
Figure 4.63: Close up of the revealed reinforcement after test (UW60R-10 East side).	122
Figure 4.64 UW60R-12 Load-slip displacement (top) and load-crack width graph (bottom). The letters in the graphs reference different stages and photographs in Figure 4.65.....	123

Figure 4.65: Photographs of UW60R-12 at different stages of the tests: a) start of test b) peak c) residual d) end of test. The average strain-gauge value at peak and at residual are included in the photographs.....	124
Figure 4.66 Photograph of the revealed reinforcement after test (UW60R-12 East side).....	125
Figure 4.67: UW80R-4 Load-slip displacement (top) and load-crack width graph (bottom). The letters in the graphs reference different stages and photographs in Figure 4.68.....	127
Figure 4.68: Photographs of UW80R-4 at different stages of the tests: a) start of test b) peak c) residual d) end of test. The average strain-gauge value at peak and at residual are included in the photographs.....	128
Figure 4.69: Photograph of the revealed reinforcement after test (UW80R-4 East side).....	129
Figure 4.70: UW80R-6 Load-slip displacement (top) and load-crack width graph (bottom). The letters in the graphs reference different stages and photographs in Figure 4.71.....	130
Figure 4.71: Photographs of UW80R-6 at different stages of the tests: a) start of test b) peak c) residual d) end of test. The average strain-gauge value at peak and at residual are included in the photographs.....	131
Figure 4.72: Photograph of the revealed reinforcement after test (UW80R-6 East side).....	132
Figure 4.73: UW80R-8 Load-slip displacement (top) and load-crack width graph (bottom). The letters in the graphs reference different stages and photographs in Figure 4.74.....	133
Figure 4.74: Photographs of UW80R-8 at different stages of the tests: a) start of test b) peak c) residual d) end of test. The average strain-gauge value at peak and at residual are included in the photographs.....	134
Figure 4.75: Close up of the revealed reinforcement after test (UW80R-8 East side).	135
Figure 4.76: UW80R-10 Load-slip displacement (top) and load-crack width graph (bottom). The letters in the graphs reference different stages and photographs in Figure 4.77.....	136
Figure 4.77: Photographs of UW80R-10 at different stages of the tests: a) start of test b) peak c) residual d) end of test. The average strain-gauge value at peak and at residual are included in the photographs.....	137
Figure 4.78: Close up of the revealed reinforcement after test (UW80R-10 East side).	138
Figure 4.79: UW80R-12 Load-slip displacement (top) and load-crack width graph (bottom). The letters in the graphs reference different stages and photographs in Figure 4.80.....	139

Figure 4.80: Photographs of UW80R-12 at different stages of the tests: a) start of test b) peak c) residual d) end of test. The average strain-gauge value at peak and at residual are included in the photographs.....	140
Figure 4.81: Close up of the revealed reinforcement after test (UW80R-12 East side).	141
Figure 5.1: Peak shear load-theoretical clamping stress plot. Specimens are separated into two group: smooth and roughened. This plot does not include specimens that did not have roughened counterparts (i.e. UW60S-2 and UW80S-2).....	144
Figure 5.2: Drop in applied load from peak load to the residual load plotted for each specimens. The averages drop in load are shown. Specimen UW60S-2 and UW80S-2 are greyed out to note that these two specimens were not included in the average.....	148
Figure 5.3: Slip displacement-theoretical clamping force plot. UW80S-6 and UW80R-6 are highlighted	149
Figure 5.4: Crack width-theoretical clamping stress plot with UW60S-6, UW60R-6, UW80S-8, and UW80R-8 highlighted.....	150
Figure 5.5: Peak shear load-theoretical clamping stress plot of smooth specimens.....	152
Figure 5.6: Peak shear load-theoretical clamping stress plot of roughened specimens.....	153
Figure 5.7: Peak-shear load-reinforcement ratio plot of the smooth specimens. 60 ksi specimens and 80 ksi specimens are marked differently.....	154
Figure 5.8: Peak-shear load-reinforcement ratio plot of the roughened specimens. The 60 ksi specimens and 80 ksi specimens are marked differently.	155
Figure 5.9: Peak shear load-theoretical clamping stress plot include all specimens.	157
Figure 5.10: Close up of the revealed reinforcement after test (UW80S-6 West side).	159
Figure 6.1: Charting the measured-to-predicted strength ratio of ACI and AASHTO models with UW specimens	164
Figure 6.2: Peak-shear stress-theoretical clamping stress plot with UW specimens and ACI and AASHTO upper stress limits (smooth specimens only).....	165
Figure 6.3: Peak-shear stress-theoretical clamping stress plot with UW specimens and ACI and AASHTO upper stress limits (roughened specimens only).....	166
Figure 6.4: Peak shear stress-theoretical clamping stress plot for all smooth specimens.....	168
Figure 6.5: Peak shear stress-theoretical clamping stress plot for all roughened specimens	169

Figure 6.6: The average measured-to-predicted strength ratio of the model from ACI318-11 (UW specimens only)	171
Figure 6.7: The average measured-to-predicted strength ratio of the model from Davaadorj [9] (UW specimens only)	174
Figure 6.8: Chart showing the average measured-to-predicted strength ratio using the proposed model.....	177

List of Tables

Table 2-1: Table 22.9.4.2 from ACI 318-19 [3] recreated. The value of λ is dependent on the concrete type. $\lambda = 1.0$ for normal-weight concrete, and $\lambda = 0.75$ for lightweight concrete.	28
Table 2-2: Table 22.9.4.4 from ACI 318-19 recreated	29
Table 2-3: AASHTO Prescribed values for cohesion factor, coefficient of friction and limit states	30
Table 2-4: Test Matrix from Bass, Carrasquillo, and Jirsa [7], including the ultimate shear load.	35
Table 2-5: Test matrix from Kono et al. [15] including the ultimate shear load of each specimens.	37
Table 2-6: Test Matrix from Kahn and Mitchell [14], including the ultimate shear load.	38
Table 2-7 Test matrix from Shaw and Sneed [22], including the ultimate shear load.	41
Table 2-8 Test Matrix from Harries at al. [12], including the ultimate shear load.	42
Table 2-9 Test Matrix from Barbosa [6], including the ultimate shear load.	44
Table 3-1: Test matrix.....	48
Table 3-2: Concrete compression strengths over time.....	54
Table 3-3: Steel reinforcement material properties	54
Table 4-1: Summary Table	63
Table 5-1: Comparison of the peak shear load between smooth and roughened specimens.....	145
Table 5-2: Tables exploring the additive qualities of cohesion and roughness. Letters indicating the surface condition of the specimen in the specimen labels (S and R) are disregarded in this table.	146
Table 5-3: Comparing the difference in applied load at peak and at residual between specimens. Specimen UW60S-2 and UW80S-2 are bolded to note that these two specimens were not included in the average.	147
Table 5-4 Average Strain and A at peak.....	156
Table 5-5 Average residual load with respect to the reinforcement ratio.....	158
Table 6-1: Table 22.9.4.4 from ACI 318-14 recreated	161
Table 6-2: AASHTO Prescribed values for cohesion factor, coefficient of friction and limit states	162

Table 6-3: Table comparing test results with ACI's and AASHTO's predictions. Bolded numbers indicate the upper stress limits. Underline numbers highlight the ratios that fall below 1.0.....	163
Table 6-4: Comparison of average measured-to-predicted strength ratio of UW specimens. Coefficients of variance are also tabulated.	167
Table 6-5: Comparing ACI and AASHTO to the database, with and without UW specimens..	168
Table 6-6: Average measured-to-predicted strength ratio of the model from ACI318-11	170
Table 6-7: Prescribed values for cohesion factor, coefficient of friction and limit states for Eq. 6.4	173
Table 6-8: Average measured-to-predicted strength ratio of the model from Davaadorj [9]	173
Table 6-9: Prescribed values for cohesion factor, coefficient of friction and limit states for Eq. 6.5	176
Table 6-10 Table showing the measured-to-predicted strength ratio of the current ACI model and the proposed model.	176
Table 7-1: Prescribed values for cohesion factor, coefficient of friction and limit states for Eq. 6.5	180

Notation List

A_{vc} = Area of concrete of the interface

A_{vf} = Area of reinforcement crossing an interface

c = Cohesion factor

CJ = Cold joint

CV = Coefficient of variation

f_y = Yield strength of steel

f'_c = Concrete compressive strength

H_{avg} = Root mean square height

H_{rms} = Average height

K_1 = Varies depending on the equation

K_2 = Varies depending on the equation

K_3 = Varies depending on the equation

K_4 = Varies depending on the equation

LED = Light-emitting diode

P_c = Externally applied force

PTFE = Polytetrafluoroethylene

R = Notation for roughened interface

R_k = Core roughness depth

S = Notation for untreated (or “smooth”) interface

UW = University of Washington

V = Shear load

V_n = Nominal shear load

V_{peak} = Peak shear load

$V_{peak,S}$ = Peak shear load of smooth specimen

$V_{peak,R}$ = Peak shear load of roughened specimen

$V_{residual}$ = Residual shear load

ΔV_{surf} = Difference in peak shear load due to different interface conditions

$\Delta V_{residual}$ = Difference between the peak shear load and the residual shear load

w_{peak} = Interface opening (i.e. interface crack width) at peak shear load

Δ_{peak} = Slip displacement at peak shear load

λ = Concrete type factor

μ = Coefficient of friction

ρ = Reinforcement ratio (A_{vf}/A_c)

σ = Standard deviation

θ = Angle of travel between two interfaces

τ = Shear stress

τ_{ACI} = Predicted shear stress based on American Concrete Institute shear friction provisions

τ_{AASHTO} = Predicted shear stress based on American Association of State Highway Transportation
Officials shear friction provisions

$\tau_{measured}$ = Measured shear stress

$\tau_{predicted}$ = Predicted shear stress

τ_{peak} = Peak shear stress

Chapter 1: Introduction

1.1 Research Impetus

Shear often needs to be transferred across an interface joining two discontinuous members such as joints between precast and cast-in-place concrete parts (i.e. cold joint), connections between vertical and horizontal elements (i.e. slab-to-shear walls connections) and connections between precast and cast-in-place concrete elements and structural steel or other structural components. Figure 1.1 below shows some structural elements requiring interface shear strength.

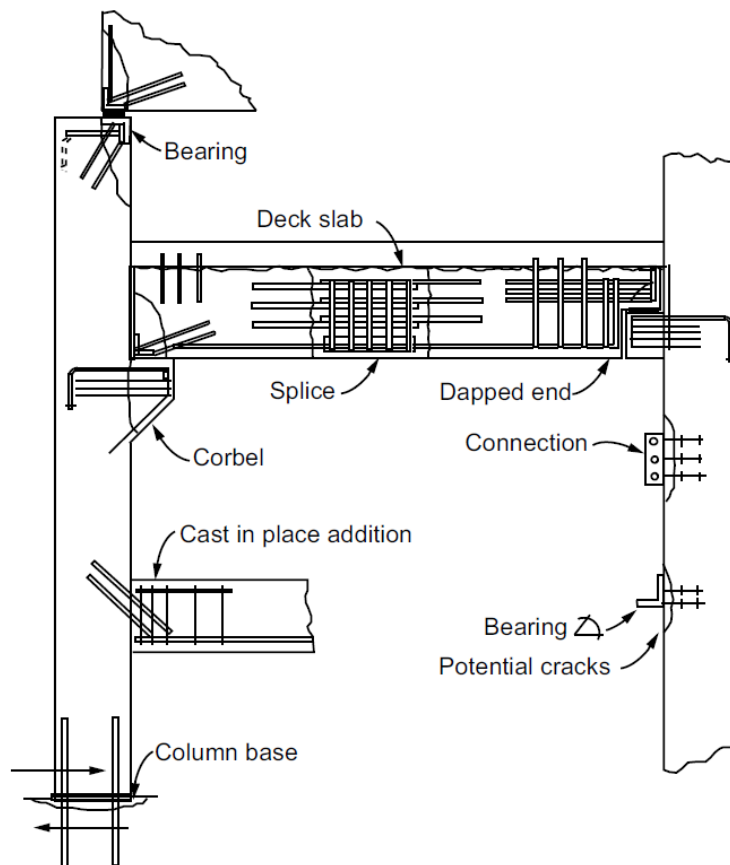


Figure 1.1: Examples of interface shear transfer in a structure [21]

Hanson [11] first tested specimens constructed to simulate common interface conditions. Since then, there are eight main variables that have been identified and investigated in past experimental studies: interface type, concrete strength and weight, shear interface area, aggregate size, reinforcement ratio, reinforcement yield strength and theoretical clamping stress. How some these variables affect the interface shear strength is still uncertain even after 60 years of research. Many

design equations were created to predict the interface shear strength and buildings codes have since adopted some these equations. However, with new experimental results and a better understanding of how individual variables affect the interface shear strength, these models need to be reevaluated and updated.

Aside from improving the current existing models, there are interests in improving how the interfaces are being designed and constructed. First, it is commonly recognized that roughening the interface increases the shear-transfer capacity at a cold joint. However, the current methods used to roughen the interface is very labor intensive. For that reason, many contractors and practicing engineers have gained interest in using surface retarders, which is a chemical that exposes aggregate by reacting with the cement. Even though surface retarders are commonly used for architectural finishing, their structural applications are lesser known. Second, because of different design limits and requirements, joints and connections are often affected by reinforcement congestion. One of many ways to reduce reinforcement congestion is using high strength steel reinforcement. Currently, due to lack of testing, the use of high strength steel reinforcement is prohibited in building codes. An experimental program focused on these design variables is proposed and forms the basis of this experimental program.

1.2 Research Objectives and Approach

The overall research objective was to study both untested and lightly tested parameters on cold-joint specimens to extend or modify existing design equations for interface shear strength. Utilizing prior research and design equations, presented in Chapter 2, several design variables were identified for further study including: 1) new techniques for achieving surface roughness, 2) investigating theoretical clamping stress values larger than those previously tested to determine if a limit based on the concrete strength is required and 3) investigate the use of high-strength (greater than specified 60 ksi) reinforcement, which is currently prohibited by ACI. The research was divided into three primary tasks:

- Task 1: Perform an initial study on surface retarders to learn how to properly apply the retarders and to identify which type of retarder to use.
- Task 2: Conduct a series of laboratory experiments on cold-joint specimens with each test series focusing on the effects of the interface roughness, high strength steel reinforcement, and reinforcement ratio. The specimens and the test setup are analogous to the specimens and the test setup utilized by researchers in the past.
- Task 3: Analyze the experimental results and design a shear friction model using the experimental results supplemented with results from similar studies.

1.3 Overview of Report

The report is organized as follows:

- Chapter 2 summarizes code equations and previous experimental research including the shear friction theory. Current shear friction provisions in American codes and summaries of past studies relevant to the experimental program are discussed in detail.
- Chapter 3 describes the experimental program including the test matrix, specimen design, test setup, and instrumentation.
- Chapter 4 discusses the test results for each test series, including the measured force response, interface slip, interface opening, and damage progression.
- Chapter 5 provides an analysis of the data. The data were evaluated to determine the contribution of cohesion and the reinforcement crossing the interface.
- Chapter 6 compares the test results to current American codified interface shear strength equations and limits. The test data were combined with prior test to evaluate the results and develop a shear friction equation that accounts for cohesion and reinforcement strength with new stress limits.
- Chapter 7 summarizes the work and provides conclusions for the research. Recommendations for future work are also provided.

Chapter 2: Current Shear Friction Provisions and Literature Review

Interface shear transfer in reinforced concrete is a topic that has been of great interest to the engineering community for several decades. The current volume of literature precludes a comprehensive review of this body of work. Thus, for the sake of brevity, this chapter focuses on aspects of past research projects that are most relevant to the experimental program conducted in this work and described in Chapters 3 and 4. This chapter is organized into two sub-sections that provide a brief overview of aspects pertaining to 1) shear friction theory and code provisions and 2) results of relevant past experimental programs.

2.1 Shear Friction Theory and Code Provisions

The behavior of concrete-to-concrete interfaces subjected to shear stresses is normally predicted using the shear friction theory. This theory, briefly discussed below, was initially postulated by Birkeland and Birkeland [8] and revisited by several authors (e.g. Hofbeck et al. [13], Kahn and Mitchell [14]) over the years.

The shear friction theory was adopted and implemented in most design codes to deal with problems related to the design of structural elements that transfer shear across an interface. Section 2.1.2 and Section 2.1.3 provide a detailed overview of the shear friction provision contained in two prominent American code provisions: the American Concrete Institute (ACI) code and American Association of State Highway Transportation Officials (AASHTO) design specifications.

2.1.1 Shear Friction Theory

The shear friction theory was first introduced by Birkeland and Birkeland [8] to model the transferring of shear loads across a concrete-to-concrete interface crossed by perpendicular steel reinforcement. According to this theory, the strength of an interface subjected to direct shear comes from the contribution of several resisting mechanisms, namely the cohesion between particles, the friction between concrete parts and the shear reinforcement crossing the interface. As the applied shear reaches a certain magnitude, the aggregate breaks away from the cement matrix, causing a crack to form along the interface plane. As the shear load is further increased, relative horizontal movement between two surfaces (i.e. crack slip) is induced. Because of the interface asperities,

the crack slip is accompanied by some extent of interface opening (i.e. crack width). The crack opening is resisted by the steel reinforcing bars crossing the interface that induce a compressive force, referred to as clamping force, acting normal to the interface. This clamping force in combination with the interaction of the surface features (i.e. coefficient of friction) provides the force that resists the applied loads and provides restraint against slip movement. Free-body diagrams that schematically outline this phenomenon, are shown in Figure 2.1:

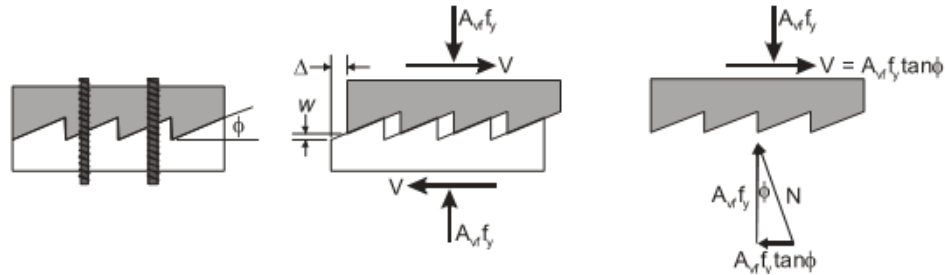


Figure 2.1: Simplified shear friction mechanism originally drawn by Birkeland and Birkeland [8] (taken from Harries et al. [12])

The shear friction theory has been well received and broadly adopted by the engineering community. Countless numerical and experimental studies have been carried out in the past 60 years (e.g. Kahn and Mitchell [14] and Shaw and Sneed [22]). Consequently, numerous variants to the original shear friction equations have been proposed over the years. However, current ACI and AASHTO provisions (discussed in the next sub-section) mainly stem from the recommendations of Hofbeck et al. [13].

Hofbeck et al. were the first to separate and identify some of the key parameters that directly affect the shear-transfer capacity: 1) pre-existing cracks (monolithically casted only); 2) yield strength, size, and arrangements of reinforcement; 3) concrete strength; 4) dowel action. The list of conclusions drawn from their experimental programs is given below:

- The shear-transfer capacity is mostly dependent on aggregate interlock and theoretical clamping force, $A_s f_y$. A_s is the area of reinforcement crossing the interface and f_y is the yield stress of the reinforcement. The reinforcement was assumed to yield at the ultimate shear load.

- The concrete strength acts as an upper limit to the expected clamping stress, ρf_y . The variable ρ is the reinforcement ratio, that is the area of reinforcement crossing the interface divided by the area of the concrete interface.
- The yield strength of the steel reinforcement crossing the interface has an effect in the shear-transfer capacity. It appears that higher strength reinforcement reaches strain-hardening earlier because higher strength reinforcement has shorter yield plateaus.
- Dowel action has no effect on the uncracked specimens but had significant effect on the pre-cracked specimen. This suggests that initial pre-cracking causes reinforcements to engage more in shear.
- Bar size and spacing do not affect the interface shear strength.

The authors proposed the shear friction equation shown below based on their conclusions:

$$V_n = A_s f_y \tan \theta \quad \text{Eq. 2.1}$$

Where,

V_n = Nominal shear strength

A_s = Area of the reinforcement crossing the interface

f_y = Yield stress of the reinforcement

θ = Angle that represents the relationship between the crack slip and crack width. The angle is shown in Figure 2.1.

The reinforcement crossing the interface was assumed to provide a normal force to the interface equal to the yield force. Based on their experimental results, as well as on the results of similar tests conducted by other researchers, it was concluded that setting $\tan \theta = 1.4$ was conservative for values of ρf_y less than $0.15f'_c$ or 600 psi. For pre-cracked specimens or specimens with higher values of ρf_y , setting $\tan \theta = 1.0$ provided good strength estimates.

The shear friction equation proposed by Hofbeck et. al was able to capture the shear friction theory in a simplified way. A lot of work was done to validate the shear friction equation and to better define the stress limits and calibrate the coefficient of friction for different joint types. Details of the upper limits and values of the coefficient of friction term are discussed in the following subsections.

2.1.2 ACI Shear Friction Provision

ACI first codified the shear friction theory in 1970, adopting the design equations proposed by Hofbeck et al. [13], but replacing the $\tan\theta$ term with a coefficient of friction, μ .

The equation below is the current ACI shear friction equation (ACI 318-19 [3] eq. 22.9.4.2) :

$$V_n = \mu A_{vf} F_y \quad \text{Eq. 2.2}$$

Where,

V_n = Nominal shear load

μ = Coefficient of friction

A_{vf} = Area of steel reinforcement crossing the interface

F_y = Yield strength of the steel reinforcement

The coefficient of friction depends on the joint types defined as monolithically-cast joint, roughened cold joint, or smooth cold joint. Roughened interface is defined as “intentionally roughened to full amplitude of approximately one quarter inch.” Table 2-1 defines values of the coefficient of friction. It should be noted that cold joints with untreated interfaces were not allowed until Mattock in 1977 [19] proposed using 0.6 for the value of μ for cold joints with smooth interfaces.

Table 2-1: Table 22.9.4.2 from ACI 318-19 [3] recreated. The value of λ is dependent on the concrete type. $\lambda = 1.0$ for normal-weight concrete, and $\lambda = 0.75$ for lightweight concrete.

Contact Surface Condition	Coefficient of Friction
Concrete placed monolithically	1.4λ
Concrete placed against hardened concrete that is clean, free of laitance, and intentionally roughened to a full amplitude of approximately 1/4 in.	1.0λ
Concrete placed against hardened concrete that is clean, free of laitance, and not intentionally roughened	0.6λ

Other experimental programs tested similar push-off specimens and validated the use this shear friction equation (Eq. 2.2). Other researchers tested different key parameters to help to create various limit states used in current shear friction provisions. Mattock and Hawkins [17] raised the ρf_y limit from the lesser of $0.15f'_c$ and 600 psi to the lesser of $0.2f'_c$ and 800 psi. Kahn and Mitchell [14] raised the upper limit of monolithically-cast joint or cold joints with roughened interfaces to from 800 psi to 1,600 psi. Other critical papers that influenced the current shear friction provisions and the papers related to this experimental program are discussed more in detail in a later section.

The code also contains a series of upper stress limits, typically determined as a function of the concrete strength and interface area. The factors are largely empirical and based on the works from Hofbeck et al [13], Mattock and Hawkin [17], and Kahn and Mitchell [14]. It should be noted that the specified reinforcement yield stress is limited to 60 ksi. Tabulated form of the limit states from ACI is shown below in Table 2-2:

Table 2-2: Table 22.9.4.4 from ACI 318-19 recreated

Condition	Maximum V_n		
Normal weight concrete placed monolithically or placed against hardened concrete intentionally roughened to a full amplitude of approximately 1/4 in.	Least of (a), (b), and (c)	$0.20f'_cA_c$	(a)
		$(480 + 0.08f'_c)A_c$	(b)
		$1600A_c$	(c)
Other cases	Lesser of (d) and (e)	$0.20f'_cA_c$	(d)
		$800A_c$	(e)

In 1983, ACI provided an alternative shear friction equation that included a separate cohesion term and a coefficient of friction factor of 0.8 applicable to all interface types (ACI 318-11 [2] R11.6.3):

$$V_n = 0.8A_vf_y + A_cK_I \quad \text{Eq. 2.3}$$

Where,

A_c = The area of concrete interface

K_I = The cohesion factor, which was fixed at 400 psi for normal weight concretes

Other variables are defined previously in Eq. 2.2

This alternative form of equation is no longer included in the ACI shear friction provisions (dropped in ACI 318-14). Other building codes (e.g. AASHTO) still include the cohesion term but contain different requirements and strength limits.

2.1.3 AASHTO Shear Friction Provisions

The AASHTO [1] shear friction equation (shown in Eq. 2.4) has a separate cohesion/aggregate interlock term. AASHTO also accounts for an applied load. The strength upper limits also exist that are slightly different with respect to those included in the ACI code. Table 2-3 shows the prescribed values of friction coefficient, cohesion, and upper stress limits that AASHTO provides for each interface type.

$$V_{ni} = cA_{cv} + \mu(A_{vf}f_y + P_c)$$

$$V_{ni} \leq K_1f'_cA_{cv}$$

$$V_{ni} \leq K_2A_{cv}$$
Eq. 2.4

Where,

c = Cohesion factor

A_{cv} = Area of concrete interface

P_c = Applied force

K_1 = Fraction of concrete strength available to resist interface shear

K_2 = Limiting interface shear resistance

Other variables are defined previously in Eq. 2.2

Table 2-3: AASHTO Prescribed values for cohesion factor, coefficient of friction and limit states

Interface Type	c (ksi)	μ	K_1	K_2 (ksi)
Monolithic	0.4	1.4	0.25	1.5
Cold joint (Rough)	0.24	1.0	0.25	1.5
Cold joint (Smooth)	0.075	0.6	0.2	0.8

Additionally, AASHTO includes a reinforcement ratio limit that is intended to prevent brittle failures:

$$A_{vf} \geq 0.05A_{cv}f_y$$
Eq. 2.5

2.2 Overview of Relevant Experimental Programs

As discussed earlier, interface shear transfer problems have been of interest to the engineering community for several decades, with the first research papers on the topic dating back to the 1960s (Hanson [11]). A thorough review of the available literature was recently conducted by Davaadorj [9], who assembled a comprehensive database collecting the results of 509 push-off tests, with concrete-to-concrete interfaces subject to monotonic pure shear loads, and steel reinforcement normal to the interface.

The review of the literature revealed that there are eight main variables that have been investigated in past experimental studies: interface type, concrete strength and weight, shear interface area, aggregate size, reinforcement ratio, reinforcement yield strength and clamping stress. The extent to which these variables have been studied experimentally is summarized in Figure 2.2, which provides the distributions and cumulative curves of the number of tests as a function of all key variables.

The multi-parametric distribution depicted in Figure 2.2 outlines that a substantial number of tests have been conducted in all of the four major surface types. Monolithically-cast specimens make up most tests available (approximately 60% of the total), with the most conducted on pre-cracked (MO-P) specimens. Cold-joint specimens represent approximately 40% of the total collected, and of them the majority were intentionally roughened cold joints (CJ-R). Of these, less than half were normal weight (NW) concrete CJ-R (87 specimens in total) and only 21 were untreated (or smooth) cold-joint specimens (CJ-S). Further to this, only eight CJ-S had steel reinforcement crossing the interface.

The tested reinforcement ratios ranged from 0% to 3%, with most of the tests falling in the 0-2% range. This, combined with the reinforcement strengths considered, resulted in clamping stresses rarely exceeding 1,600 psi. The few tests that exceed this threshold exist pertain to MO-P interfaces. With specific reference to CJs, there were only four specimens characterized by clamping stress (ρf_y) values exceeding 1,000 psi. In approximately 90% of the tests, the reinforcement yield stress was lower than 80 ksi. More specifically, only 26 specimens presented reinforcement yield stress over 80 ksi, and the results were somewhat inconsistent.

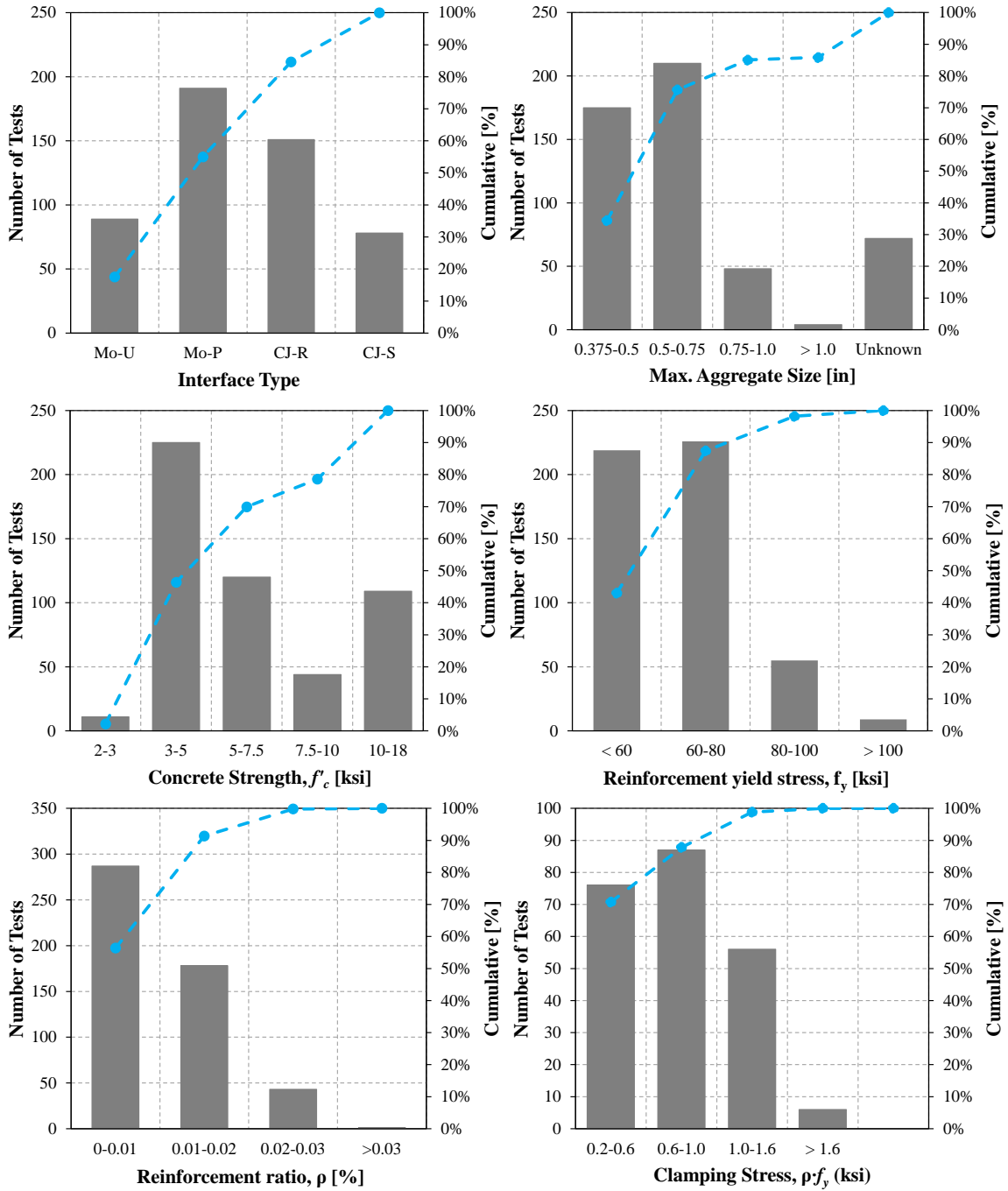


Figure 2.2: Figure 2 from Davaadorj et al. [10]. Frequency distribution of tests as a function of main parameters.

It is evident that, despite their importance in practical applications, cold joints have received somewhat limited experimental attention, and that major knowledge gaps exist, particularly pertaining to variables such as interface roughening and steel reinforcement strength. The following of this section is dedicated to a more thorough review of past research that focused on these variables.

2.2.1 Bass, Carrasquillo, and Jirsa (1989)

Bass et al. [7] focused on cold-joint specimens. The authors constructed specimens based on a retrofitting method where holes are drilled into an interface of interest and reinforcing bars are embedded before casting the second concrete block. The experimental program involved 33 specimens and the variables of interest were the reinforcement ratio, the embedment lengths of reinforcing bars, concrete strength, and surface condition.

The different surfaces were achieved using various techniques: 1) untreated surface, 2) sandblasted surface, 3) surface chipped with a pickaxe, 4) 1-inch depth shear keys, and 5) surface with epoxy bonding agents. The interface reinforcement was embedded after casting the base-block. The holes were drilled then steel dowels were placed inside the hole with epoxy. The specimens and the test set up is shown in Figure 2.3 and in Figure 2.4. The test matrix and the results are provided in Table 2-4.

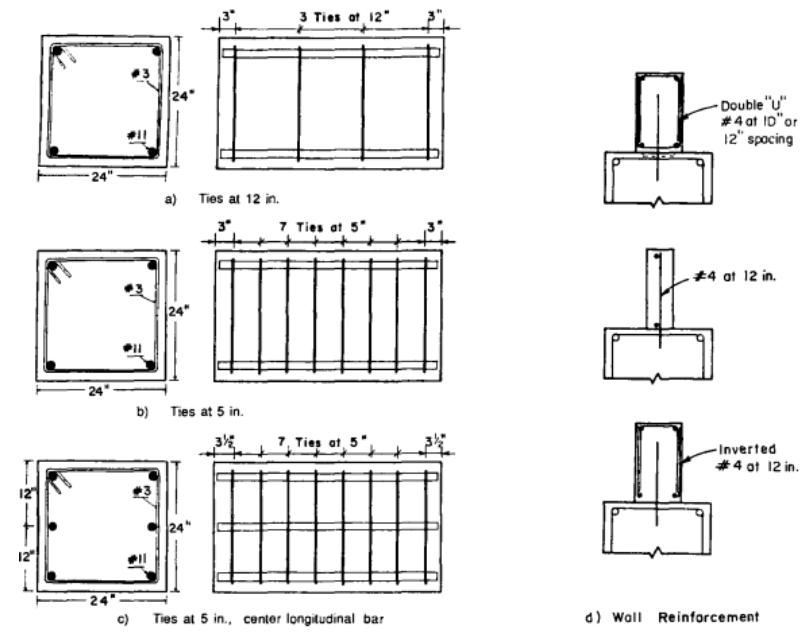


Figure 2.3: Fig. 2 from Bass et al. [7]. Details of the specimen. Base-block and wall reinforcement.

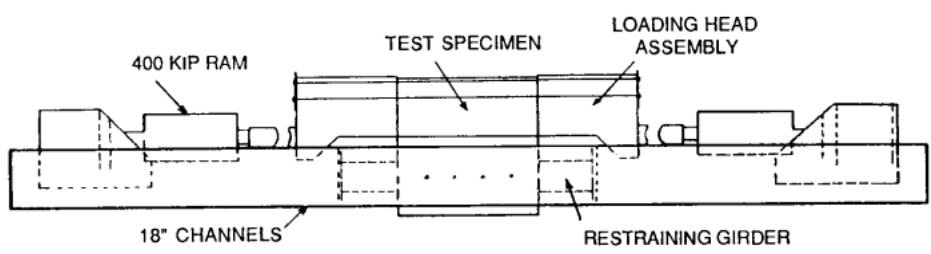


Figure 2.4: Fig. 7 from Bass et al. [7]. Test frame.

Table 2-4: Test Matrix from Bass, Carrasquillo, and Jirsa [7], including the ultimate shear load.

Specimen	f'_c (ksi)	f_y (ksi)	ρf_y (psi)	Surface Preparation	Embedment length (in)	V_u (kip)
1A	3.1	60	589	Sandblasted	6	145
2A	3.1	60	589	Sandblasted	6	153
3A	3.1	60	589	Sandblasted	6	152
4A	3.1	60	589	Sandblasted	6	165
5A	3.1	60	589	Sandblasted	6	150
6A	3.1	60	589	Sandblasted	6	165
7A	3.1	60	393	Sandblasted	6	132
8A	3.1	60	1178	Sandblasted	6	210
9A	3.1	60	589	Sandblasted	12	190
10A	3.1	60	589	Sandblasted	3	130
11A	2.7	60	589	Sandblasted	6	104
12A	2.75	60	589	Chipped	6	118
13A	2.75	60	589	Shear Keyed	6	128
14A	2.75	60	589	Untreated	6	90
15A	2.75	60	589	Sandblasted	6	88
16A	2.75	60	589	Epoxy	6	105
17A	2.7	60	589	Sandblasted	6	125
18A	2.75	60	589	Chipped	6	118
19A	2.75	60	589	Shear Keyed	6	127
20A	2.87	60	589	Sandblasted	6	134
21A	4.15	60	589	Chipped	6	115
22A	4.3	60	589	Shear Keyed	6	148
23A	4.3	60	589	Sandblasted	3	135
24A	4.3	60	589	Sandblasted	6	160
1B	3.21	60	982	Sandblasted	6	102
2B	3.21	60	589	Sandblasted	6	150
3B	3.21	60	589	Sandblasted	6	162
4B	3.21	60	393	Sandblasted	12	137
5B	3.21	60	589	Sandblasted	6	166
6B	3.21	60	589	Sandblasted	12	172
17B	2.87	60	589	Sandblasted	12	151
20B	2.7	60	589	Chipped	6	75
21B	4.3	60	589	Sandblasted	12	132

The results of the experimental programs showed that the shear-transfer capacity increased with increasing depth of embedment, especially at large slip, meaning that bond directly influenced the capacity. The confinement of concrete around the interface was had an impact on the shear-transfer capacity as well. This suggested that dowel action and bond were important parameters in cold joints.

Sandblasted surfaces showed good results compared to conventional surface treatment methods, while it was found that treating the interface with an epoxy bonding agent was not effective. Different methods of treating the surface had little to no effect after 0.2 inch of slip displacement, meaning that the steel reinforcement was providing majority of the shear-transfer capacity after peak load.

The authors concluded that reinforcement ratio had direct impact on the shear-transfer capacity. It was also verified that the shear friction provision of ACI provided conservative strength estimates, with an average measure-to-design shear strength ratio of 1.77 with *CV* of 18.6%. The ACI development length requirement was conservative for shear friction applications as well.

2.2.2 Kono, Tanaka, and Watanabe (2000)

Kono et al. [15] investigated the contributions of dowel action and cohesion in the context of interface shear applications. They tested 23 specimens with varying concrete strength, reinforcement yield strength, bar diameter, and different interface roughening methods that involved trowels, wire brushes, nails, and steel triangular molds. The first series of specimens (15 specimens with a label “H”) was designed to investigate reinforcement yield stress and concrete strength. The yield stress of the reinforcement ranged from 47 ksi to 145 ksi, and concrete compressive strength ranged from 4.4 ksi to 11.6 ksi. In 6 of the 15 specimens, a steel plate was placed between the two concrete members to remove the concrete contribution to isolate dowel action. The test matrix with the experimental result is summarized in Table 2-5:

Table 2-5: Test matrix from Kono et al. [15] including the ultimate shear load of each specimens.

Specimen	f'_c (ksi)	f_y (ksi)	Surface Preparation	V_u (kip)
L10-30C	4.4	47.0	Troweled	53.6
L10-30D	4.4	47.0	Plate	N/A
L10-50C	7.3	47.0	Troweled	60.2
L10-50C	7.3	47.0	Plate	N/A
L10_80C	11.6	47.0	Troweled	46.0
L10_80C	11.6	47.0	Plate	N/A
H10-30C	4.4	144.9	Troweled	61.7
H10-30C	4.4	144.9	Plate	N/A
H10-50C	7.3	144.9	Troweled	53.1
H10-50C	7.3	144.9	Plate	N/A
H10-80C	11.6	144.9	Troweled	92.8
H10-80C	11.6	144.9	Plate	N/A
H16-30C	4.4	125.7	Troweled	80.8
H16-50C	7.3	125.7	Troweled	104.9
H16-80C	11.6	125.7	Troweled	117.4
H50PC	7.3	144.9	Troweled	27.0
H50SC	7.3	144.9	Scratched	51.4
H50RC	7.3	144.9	Rough	131.5
H50TC	7.3	144.9	Triangle	125.4
H100PC	14.5	144.9	Troweled	76.8
H100SC	14.5	144.9	Scratched	127.9
H100RC	14.5	144.9	Rough	150.4
H100TC	14.5	144.9	Triangle	126.3

The experimental results showed that specimens with higher ρf_y values had higher shear-transfer capacity, and that dowel action made a more significant contribution at larger slip displacement. The study showed that up to 2 mm (0.079 inch) of slip displacement, the specimens performed as well as any monolithically-cast specimens. The researchers also concluded that the interface could endure large slip without significant degradation in strength because of dowel action.

The surface roughness was quantified using the variables: root mean square height, H_{rms} , average height, H_{avg} and core roughness depth, R_k . Different surface treatment methods resulted in different roughness measurements. Core roughness depth ranged from 0.16 mm (0.0063 inch) to 6.5 mm (0.26 inch), but somewhat surprisingly, the results showed that core roughness depth and shear-transfer capacity did not correlate. It was thus concluded that the surface treatment does not impact the shear-transfer capacity.

Another notable finding was that the reinforcing bars did not yield at the peak load. Based on this outcome, Kono et al. proposed the use of ρf_s instead of ρf_y to predict the shear-transfer capacity. Regression analysis was used to find a suitable approximation of stress of the reinforcing bars at peak load, f_s .

$$f_s = 2/3 f_y \quad \text{Eq. 2.6}$$

A modified shear friction equation that includes a modification factor, k , to account for the concrete strength and an upper limit on the clamping stress, ρf_y , of 7.6 MPa:

$$\tau_u = k (0.67 \rho f_y + 2.84) \text{ (MPa);} \quad \text{Eq. 2.7}$$

Where, $k = 0.02 f'_c + 0.2$ for $f'_c < 40$ MPa, and $k = 1.0$ otherwise

2.2.3 Kahn and Mitchell (2002)

Kahn and Mitchell [14] tested 50 specimens with varying concrete strength, reinforcement ratio, and joint type. The recorded peak shear loads, the concrete strength and clamping stress values considered are reported in the test matrix shown in Table 2-6. The surface of the cold-joint specimens was not intentionally roughened, but the researchers reported quarter inch amplitude.

Table 2-6: Test Matrix from Kahn and Mitchell [14], including the ultimate shear load.

Specimen	f'_c (psi)	f_y (ksi)	ρf_y(psi)	Joint Type	V_u (kip)
SF-4-1-U	6805	60	255	Uncracked Monolithic	35
SF-4-1-C	6805	60	255	Pre-cracked Monolithic	58
SF-4-2-U	6805	60	510	Uncracked Monolithic	56
SF-4-2-C	6805	60	510	Pre-cracked Monolithic	80
SF-4-3-U	6805	60	765	Uncracked Monolithic	71
SF-4-3-C	6805	60	765	Pre-cracked Monolithic	86
SF-7-1-U	11734	60	304	Uncracked Monolithic	42
SF-7-1-C	11734	60	304	Pre-cracked Monolithic	54
SF-7-1-CJ	11734	60	304	Cold joint	88
SF-7-2-U	12410	60	609	Uncracked Monolithic	52
SF-7-2-C	12410	60	609	Pre-cracked Monolithic	82
SF-7-2-CJ	11734	60	609	Cold joint	118
SF-7-3-U	13103	60	913	Uncracked Monolithic	72

SF-7-3-C	13103	60	913	Pre-cracked Monolithic	110
SF-7-3-CJ	12471	60	913	Cold joint	138
SF-7-4-U	12471	60	1217	Uncracked Monolithic	63
SF-7-4-C	12471	60	1217	Pre-cracked Monolithic	133
SF-7-4-CJ	12471	60	1217	Cold joint	149
SF-10-1-U-a	12053	60	304	Uncracked Monolithic	26
SF-10-1-U-b	14326	60	304	Uncracked Monolithic	30
SF-10-1-C-a	12053	60	304	Pre-cracked Monolithic	32
SF-10-1-C-b	14326	60	304	Pre-cracked Monolithic	100
SF-10-1-CJ	14326	60	304	Cold joint	92
SF-10-2-U-a	14676	60	609	Uncracked Monolithic	51
SF-10-2-U-b	14804	60	609	Uncracked Monolithic	48
SF-10-2-C-a	14676	60	609	Pre-cracked Monolithic	49
SF-10-2-C-b	14804	60	609	Pre-cracked Monolithic	131
SF-10-2-CJ	12053	60	609	Cold joint	124
SF-10-3-U-a	16170	60	913	Uncracked Monolithic	65
SF-10-3-U-b	13934	60	913	Uncracked Monolithic	63
SF-10-3-C-a	16170	60	913	Pre-cracked Monolithic	114
SF-10-3-C-b	13934	60	913	Pre-cracked Monolithic	145
SF-10-3-CJ	12953	60	913	Cold joint	148
SF-10-4-U-a	15468	60	1217	Uncracked Monolithic	74
SF-10-4-U-b	16476	60	1217	Uncracked Monolithic	76
SF-10-4-C-a	15468	60	1217	Pre-cracked Monolithic	126
SF-10-4-C-b	16476	60	1217	Pre-cracked Monolithic	156
SF-10-4-CJ	12953	60	1217	Cold joint	160
SF-14-1-U	17957	60	304	Uncracked Monolithic	25
SF-14-1-C	16015	60	304	Pre-cracked Monolithic	91
SF-14-1-CJ	14756	60	304	Cold joint	95
SF-14-2-U	17362	60	609	Uncracked Monolithic	40
SF-14-2-C	15496	60	609	Pre-cracked Monolithic	99
SF-14-2-CJ	14756	60	609	Cold joint	108
SF-14-3-U	16255	60	913	Uncracked Monolithic	56
SF-14-3-C	15392	60	913	Pre-cracked Monolithic	135
SF-14-3-CJ	15218	60	913	Cold joint	146
SF-14-4-U	16059	60	1217	Uncracked Monolithic	73
SF-14-4-C	15982	60	1217	Pre-cracked Monolithic	153
SF-14-4-CJ	15218	60	1217	Cold joint	156

The ultimate load reported in Table 2-6 was defined as the maximum load recorded for slip displacement values ranging between 0 and 0.2 inch, and the residual shear capacity (not reported here) was defined as the load recorded at 0.2 inch of slip displacement. The study revealed that, of the different approaches considered, the shear friction equation proposed by Birkeland and Birkeland [8] best predicted the response of cold-joint specimens. The Birkeland and Birkeland equation is provided in Eq. 2.8 below:

$$V_u = 0.05f'_c + 1.4\rho f_y \leq 0.2f'_c \quad \text{Eq. 2.8}$$

It was also found that the shear friction provision of ACI was conservative for all joint types tested, particularly for cold-joint specimens independently of concrete strength. The residual load was similar between all three different types of specimens. This was attributed to the fact that the residual strength is provided solely by the steel reinforcement crossing the interface through dowel action.

2.2.4 Shaw and Sneed (2014)

Shaw and Sneed [22] tested 36 cold-joint specimens to study how the interface strength is affected by the compressive strength of concrete and the interface surface roughness. The interface was roughened by “scoring the surface of the shear interface in the direction perpendicular to the direction of loading.” The recorded peak shear loads, the concrete strength and clamping stress values considered are reported in the test matrix shown in Table 2-7:

Table 2-7 Test matrix from Shaw and Sneed [22], including the ultimate shear load.

Specimen	Concrete Type	f'_c (psi)	f_y (ksi)	ρf_y (psi)	Surface Condition	V_u (kip)
N5R4	Normal weight	4860	66.2	880	Rough	59
N5R5	Normal weight	4860	66.2	880	Rough	53
N5R6	Normal weight	4860	66.2	880	Rough	53
N5S4	Normal weight	4860	66.2	880	Smooth	33
N5S5	Normal weight	4860	66.2	880	Smooth	35
N5S6	Normal weight	4860	66.2	880	Smooth	39
S5R1	Sand light weight	4550	66.2	880	Rough	51
S5R2	Sand light weight	4550	66.2	880	Rough	50
S5R3	Sand light weight	4550	66.2	880	Rough	54
S5S1	Sand light weight	4550	66.2	880	Smooth	39
S5S2	Sand light weight	4550	66.2	880	Smooth	34
S5S3	Sand light weight	4550	66.2	880	Smooth	40
A5R1	Light weight	6080	66.2	880	Rough	48
A5R2	Light weight	6080	66.2	880	Rough	53
A5R3	Light weight	6080	66.2	880	Rough	51
A5S1	Light weight	6080	66.2	880	Smooth	41
A5S2	Light weight	6080	66.2	880	Smooth	40
A5S3	Light weight	6080	66.2	880	Smooth	39
N8R1	Normal weight	7550	66.2	880	Rough	74
N8R2	Normal weight	7550	66.2	880	Rough	56
N8R3	Normal weight	7550	66.2	880	Rough	64
N8S1	Normal weight	7550	66.2	880	Smooth	66
N8S2	Normal weight	7550	66.2	880	Smooth	53
N8S3	Normal weight	7550	66.2	880	Smooth	55
S8R1	Sand light weight	7210	66.2	880	Rough	72
S8R2	Sand light weight	7210	66.2	880	Rough	67
S8R3	Sand light weight	7210	66.2	880	Rough	67
S8S1	Sand light weight	7210	66.2	880	Smooth	67
S8S2	Sand light weight	7210	66.2	880	Smooth	58
S8S3	Sand light weight	7210	66.2	880	Smooth	59
A8R1	Light weight	7845	66.2	880	Rough	62
A8R2	Light weight	7845	66.2	880	Rough	64
A8R3	Light weight	7845	66.2	880	Rough	64
A8S1	Light weight	7845	66.2	880	Smooth	46
A8S2	Light weight	7845	66.2	880	Smooth	48
A8S3	Light weight	7845	66.2	880	Smooth	52

Smooth and roughened specimens had similar initial stiffness, but the smooth specimens experienced greater slip than their roughened counterparts as the applied load increased. The roughened specimens reached higher peak loads, but they manifested a more brittle behavior. Notably, it was found that the concrete strength affected the peak shear load for both smooth and roughened specimens. It was also reported that the steel reinforcement crossing the interface yielded at peak load. Consistently with the outcome of previous studies, the residual strengths were all similar, regardless of concrete strength and interface condition.

The researchers concluded that the ACI code provisions provided conservative estimates of the experimental strength in all cases. In particular, it was noted that the 800 psi limit for smooth cold joints, currently present in the ACI code appeared excessively strict. To this end, it was suggested that the strength upper limit should be a function of the concrete strength rather than be assigned an arbitrary value.

2.2.5 Harries, Zeno, and Shahrooz (2012)

Harries et al. [12] investigated high strength reinforcement and bar size with cold-joint specimens. Their test matrix, shown in Table 2-8, included eight specimens with two reinforcement parameters: bar diameter and steel yield stress. All interfaces were roughened to a minimum amplitude of one quarter inch.

Table 2-8 Test Matrix from Harries et al. [12], including the ultimate shear load.

Specimen	f'_c (psi)	f_y (ksi)	ρf_y (psi)	V_u (kip)
615-3A	5800	67.3	277	66.2
615-3B	5800	67.3	272	66.8
614-4A	5800	61.5	447	50
614-4B	5800	61.5	454	58.2
1035-3A	5800	130	545	57.2
1035-3B	5800	126	517	72.5
1035-4A	5800	140	1034	58.4
1035-4B	5800	131.3	980	60

The slip displacement recorded at the peak load was different for specimens with different bar sizes. Stress in the reinforcing steel was negligible until slip displacement of approximately 0.01 inch. The reinforcing bars did not yield at peak and had little clamping stress, implying that the

crack width was not enough to fully engage the bars. The 60 ksi specimens had a post-peak sharp degradation, while the 100 ksi specimens exhibited non-trivial post-peak load-carrying capacity. Notable conclusions were that the theoretical clamping stress mattered for prediction of the peak shear load, but the yield strength of the bars did not. Additionally, the overall stiffness was not affected by bar size or yield strength.

The authors proposed a shear friction equation (Eq. 2.9 reported below) that involved both a cohesion term and a clamping force-proportional term. The term that is proportional to the clamping force was directly related to the steel modulus, E_s , instead of the yield stress of the steel reinforcement.

$$V_{ni} = \alpha A_{cv} f'_c + 0.002 A_{cv} E_s \leq 0.2 A_{cv} f'_c \quad \text{Eq. 2.9}$$

It is interesting to note that previous research programs (e.g. Khan and Mitchell [14] and Hofbeck et al. [13]) had reported yielding of the reinforcing bars crossing the interface at peak load. Harries and Zeno attributed the conflicting results of the stress of the steel reinforcement at peak load to the natural scattering of the tests. Even though the steel reinforcement did not reach yield at peak, Harries et al. proposed that the 60 ksi limit in ACI should be raised to a higher value.

2.2.6 Barbosa, Trejo, and Nielsen (2017)

The experimental program conducted by Barbosa et al. [6] investigated the impact of high strength steel, reinforcement ratio and bar diameter, on the shear strength of cold-joint specimens. The test program consisted of 20 push-off specimens: 10 specimens had 60 ksi reinforcing bars and 10 specimens had 80 ksi reinforcing bars. Each of the group of specimens contained five specimens with No. 4 bars and five with No. 5 bars. To match the reinforcement ratio for different sized bars, the interface of the No. 5 bar specimen was partially de-bonded to reduce the net concrete section that resists the shear transfer. The interface had an amplitude of approximately one eighth inch. The test matrix with the peak shear loads are provided in Table 2-9, and the specimen dimensions are shown in Figure 2.5.

Table 2-9 Test Matrix from Barbosa [6], including the ultimate shear load.

Specimen	f'_c (psi)	f_y (ksi)	ρf_y (psi)	V_u (kip)
4G60-1	4481	72.6	302.5	279.0
4G60-2	4481	72.6	302.5	256.5
4G60-3	4198	72.6	302.5	244.5
4G60-4	4198	72.6	302.5	264.2
4G60-5	4198	72.6	302.5	269.8
4G80-1	4372	93.0	387.5	232.8
4G80-2	4198	93.0	387.5	243.5
4G80-3	4198	93.0	387.5	252.5
4G80-4	4198	93.0	387.5	262.2
4G80-5	4198	93.0	387.5	290.6
5G60-1	4578	67.6	436.6	273.3
5G60-2	4578	67.6	436.6	275.8
5G60-3	4149	67.6	436.6	277.4
5G60-4	4149	67.6	436.6	272.1
5G60-5	4149	67.6	436.6	275.2
5G80-1	4578	86.8	560.6	301.7
5G80-2	4149	86.8	560.6	305.7
5G80-3	4149	86.8	560.6	312.4
5G80-4	4149	86.8	560.6	282.7
5G80-5	4149	86.8	560.6	297.2

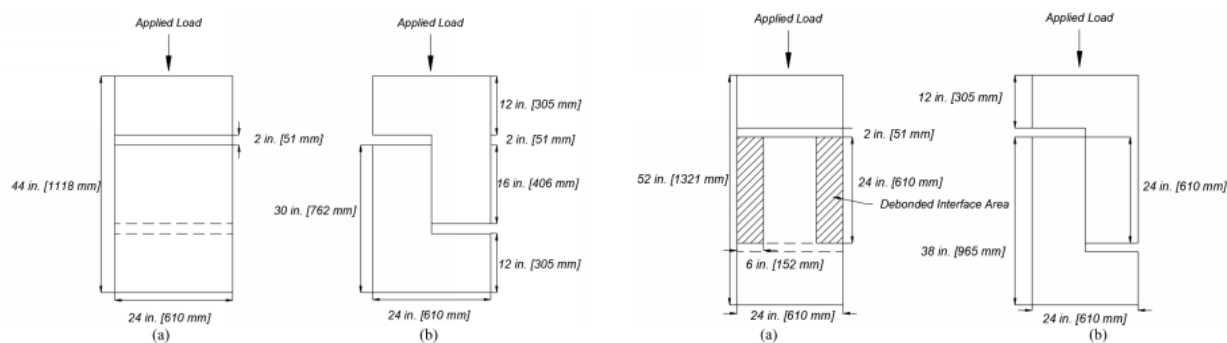


Figure 2.5: Fig 3.3 and 3.4 from Barbosa [6]. Test elevation for specimens No.4 (left) and No.5 (right) reinforcing bars.

Sustained shear load was higher for specimens with 80 ksi reinforcement. This result was consistent for both No. 4 and No. 5 bar specimens. The 80 ksi specimens had greater peak capacity but only for No. 5 bar specimens. The lack of consistency suggested that the reinforcement ratio by itself did affect the shear-transfer capacity. The peak shear load was similar for all specimens, suggesting that cohesion and aggregate interlock played a major role with respect to the peak strength of specimens. The No. 5 bar specimens also consistently had higher shear-transfer

capacity than No. 4 bar specimens. However, this was mainly attributed to some issues associated to the de-bonded areas.

The reinforcing bars yielded at peak load for the 60 ksi specimens, but pre-peak yielding was recorded for the 80 ksi specimens. These somewhat surprising and inconsistent results provide the motivation for additional experimental research to be performed in this area. However, since the 80 ksi specimens had higher sustained shear loads, the researchers suggested that 80 ksi bars should still be allowed for use in practical applications.

2.3 Findings and Summary

The theoretical clamping stress and concrete strength (within a certain range) had a significant effect on the shear-transfer capacity of cold joints. However, the isolated effects of the reinforcement ratio and yield strength were lesser known. For example, some the results of some experimental programs showed that the reinforcement yielded at ultimate shear load, while some showed no yielding of the reinforcing bars. There were only a limited number of tests that dealt with cold joints and even fewer that tested high strength reinforcement.

Chapter 3: Experimental Design

The literature review indicated that the following parameters are not well understood and/or studied: cold joints, surface roughness, roughening methods, strength limits, and steel reinforcement yield strength. The experimental program was created with a focus on these parameters:

- Cold joints: the cold-joint specimens tested in past studies were limited in number with respect to other interface types, so cold-joint specimens became the focus of this experimental program.
- Surface roughness: surface roughness and treatment are important because it is believed that the interface roughness is directly proportional to its shear strength. However, it is currently labor intensive to achieve a rough interface that complies with ACI standards. In this study, surface retarders were used to investigate their effectiveness in achieving similar behavior of physically roughened specimens.
- Strength upper limits: the current strength upper limits in shear friction provisions were questioned in some of the past studies reviewed in Chapter 2 [13],[14]. A series of tests were developed to investigate theoretical clamping stress values that would result higher strength than currently prescribed code limits.
- Steel strength: there is an interest in increasing the yield strength limit of the reinforcement crossing the shear interface, and the evidence collected in Chapter 2 suggests that the use of steel reinforcement with yield stress exceeding 60 ksi may represent a viable option. As such, both 60 and 80 ksi reinforcement were investigated.

The chapter presents the test matrix, specimen design, test set up, and instrumentation.

3.1 Test Matrix

Twenty-four cold-joint specimens with varying roughness, reinforcement ratios, and steel reinforcement yield strengths were designed and tested. Table 3-1 presents the test matrix. The test matrix includes test series, specimen label, measured concrete compressive strength, measured yield strength of the reinforcing bars, area of reinforcement, reinforcement ratio, and the theoretical clamping stress. In the table, each specimen has a designation. The first number in the specimen label refers to the specified yield strength of the reinforcement crossing an interface. The letter “R” or “S” indicates roughened or smooth interface. The number following the hyphen refers to the number of bars crossing the interface (e.g. “2” indicates that there are two No. 5 bars crossing the interface). For example, UW60R-8 has eight 60 ksi bars crossing a roughened interface.

The specimens were separated into five test series:

1. Test series 0 included two specimens with different surface conditions (smooth and roughened) with no reinforcement crossing an interface
2. Test series 60S included six specimens with varying numbers of 60 ksi bars crossing a smooth interface.
3. Test series 80S included six specimens with varying numbers of 80 ksi bars crossing a smooth interface.
4. Test series 60R included five specimens with varying numbers of 60 ksi bars crossing a roughened interface.
5. Test series 80R included five specimens with varying numbers of 80 ksi bars crossing a roughened interface.

Test series 60S, 80s, 60R and 80R isolated the effects of the reinforcement ratio. Between test series 60S and 60R, and 80S and 80R, specimens with identical reinforcement parameters were compared to highlight the effects of interface roughness. Test series 0 was similarly designed to test the effects of roughness. The roughened interfaces had a minimum average amplitude of one quarter inch to meet the ACI requirement using surface retarders, and the amplitude of the roughness was measured using a ruler.

Table 3-1: Test matrix

Test Series	Specimen	f'_c (psi)	f_y (ksi)	A_{vf} (in ²)	ρ (%)	ρf_y (psi)
0	UW0S	5,850	N/A	0	0	0
	UW0R					
60S	UW60S-2	5,651	74.4	0.62	0.39	290
	UW60S-4			1.24	0.78	580
	UW60S-6			1.86	1.16	863
	UW60S-8			2.48	1.55	1153
	UW60S-10			3.1	1.94	1443
	UW60S-12			3.72	2.33	1734
80S	UW80S-2	5,651	98.1	0.62	0.39	383
	UW80S-4			1.24	0.78	765
	UW80S-6			1.86	1.16	1138
	UW80S-8			2.48	1.55	1521
	UW80S-10			3.1	1.94	1903
	UW80S-12			3.72	2.33	2286
60R	UW60R-4	5,850	74.4	1.24	0.78	580
	UW60R-6			1.86	1.16	863
	UW60R-8			2.48	1.55	1153
	UW60R-10			3.1	1.94	1443
	UW60R-12			3.72	2.33	1734
80R	UW80R-4	5,850	98.1	1.24	0.78	765
	UW80R-6			1.86	1.16	1138
	UW80R-8			2.48	1.55	1521
	UW80R-10			3.1	1.94	1903
	UW80R-12			3.72	2.33	2286

3.2 Specimen Design

As indicated in Chapter 2, there are different test setups that have been used to test shear friction. The specimen and the reinforcement details used in this experimental program are modeled off push-off specimens subjected to monotonic pure shear loads for simplicity and consistency with prior tests (e.g. Figure 2.5). Although other methods may provide a more accurate method to investigate shear friction of surfaces with multidirectional loading, using a more advanced setup was beyond the scope of this project. Figure 3.1 provides the typical geometry and reinforcement layout of each specimen, while details pertaining to the steel reinforcement crossing the interface are provided in Table 3-1. The specimen geometry and bar size of the reinforcement were constant. The specimen height was 24 inches, the width was 10 inches, and the length was 48 inches. The length of the interface was 16 inches, and the area of the interface was 160 in². Horizontal 2-inch gaps between two halves of the specimens were designed to allow for relative slip displacement. This gap is highlighted in Figure 3.1. A 1.5-inch cover was used throughout the specimen. The specimen was reinforced with No. 5 reinforcing bars as shown in Figure 3.1. Hoop reinforcement was used as interface reinforcement to ensure full development. The interface reinforcing bars were spaced out evenly along the length of the interface area.

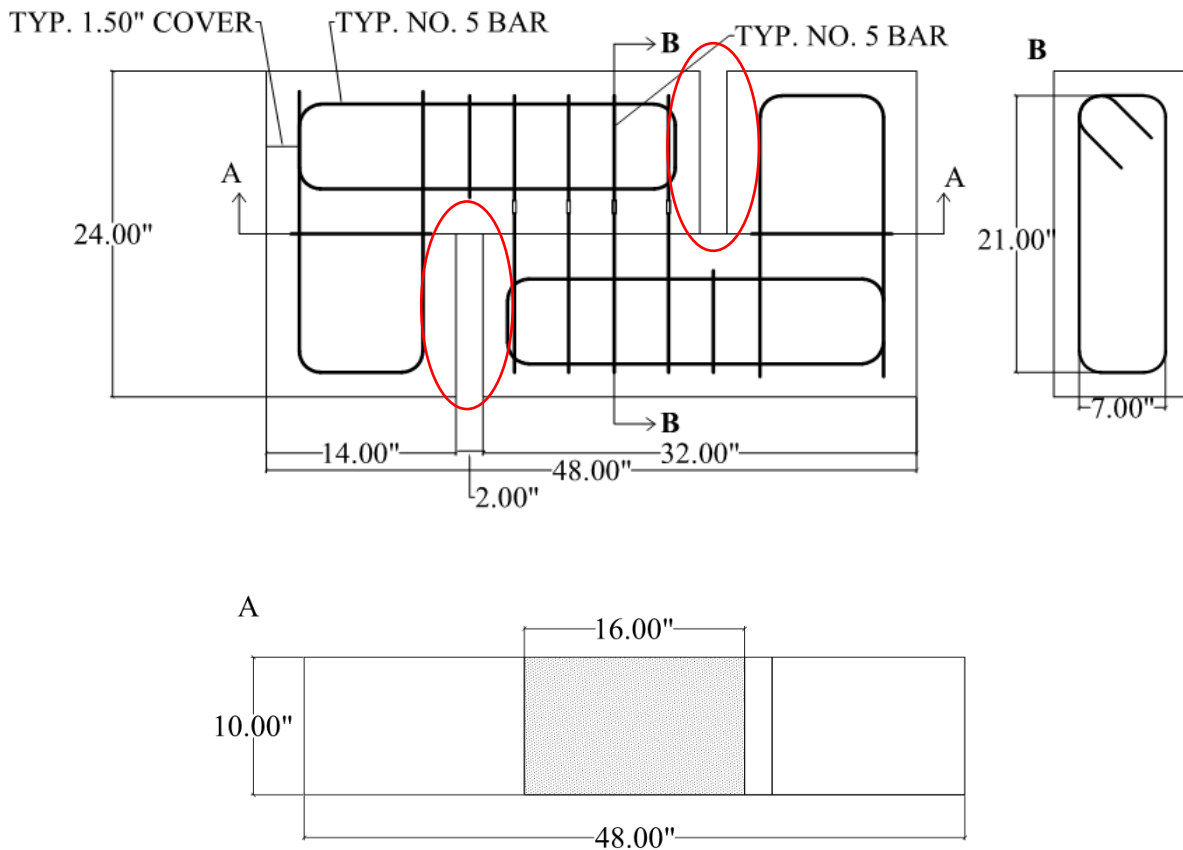


Figure 3.1: Drawing of a specimen with typical reinforcement details. Grey region in Section cut A-A is the interface region. Section cut B-B shows dimension of the interface reinforcement.

To investigate the use of retarders to achieve interface roughness, companion 6 inches by 6 inches by 3.5 inches concrete specimens were cast and treated. Two different retarders were tested: Dayton Superior's Top-Cast Top-Surface Retarders Grade 15 (yellow) and Grade 150 (light blue). The Grade 15 retarder did not result in minimum average amplitude of one quarter inch whereas the Grade 150 retarder did (Figure 3.2 and Figure 3.3). The amplitude was measured manually using a ruler. Grade 150 retarder was used for the shear-friction specimens.

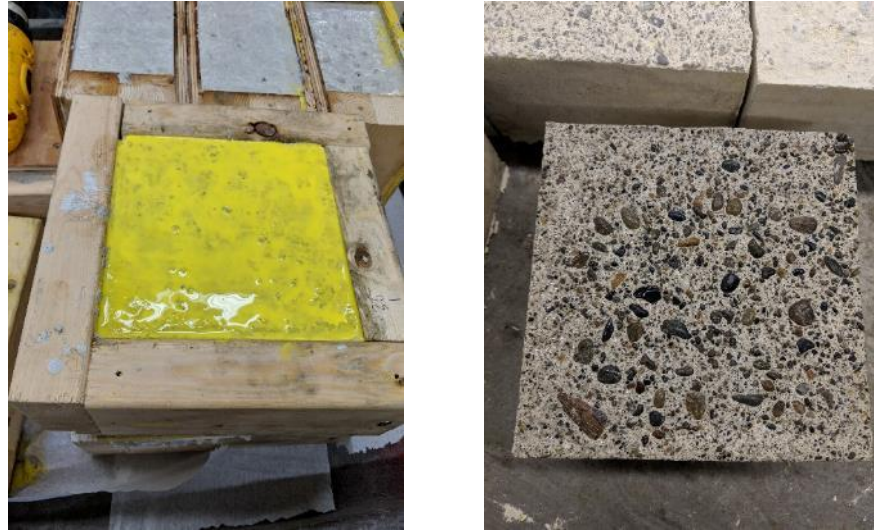


Figure 3.2: Specimen treated with Grade 15 retarder

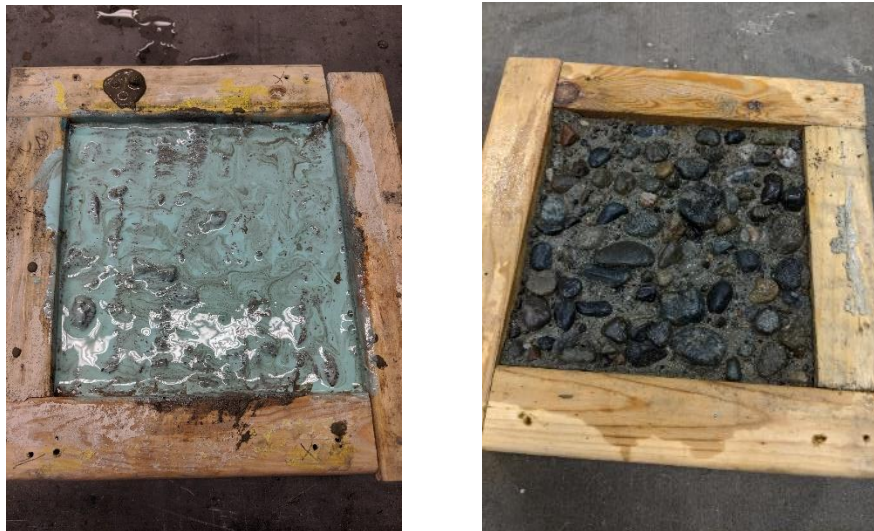


Figure 3.3: Specimen treated with Grade 150 retarder

The specimen construction was as follows:

1. The reinforcement cage was constructed.
2. The bottom half of the specimen was cast first (Figure 3.4).
3. The interface was smoothed out or treated with retarders (Figure 3.5 and Figure 3.6).
4. Within 48 hours of the first cast, the second half of the specimen was cast (Figure 3.7)



Figure 3.4: Photograph showing the first half of the specimen being casted and the interface being treated with surface retarders.



Figure 3.5: Photograph of an untreated surface.



Figure 3.6: Photograph of a surface treated with surface retarder.



Figure 3.7: Photograph of UW60R-8

3.2.1 Concrete Material Properties

Companion cylinders made of concrete from each cast were tested to obtain compression strength. The material properties of two halves did not show much difference, so the average compressive strength of the two halves was recorded. The concrete cylinders and the specimens were cast, cured, and tested following the ASTM C39/C39M-16 [5] guidelines. The average compressive strength, f'_c , of the first series of specimens (60S and 80S) was 5,651 psi and the strength of the second series of specimens (0, 60R and 80R) was 5,850 psi.

Table 3-2: Concrete compression strengths over time.

Time (days)	f'_c (psi)	
	Test Series 60S and 80S	Test Series 0, 60R, and 80R
7	3,937	3,036
14	4,519	3,939
21	4,831	4,661
28	4,940	5,850
Day of test	5,651	5,850

3.2.2 Reinforcement Material Properties

Grade 60 ASTM A706 and grade 80 ASTM 706A No. 5 steel reinforcing bars were used in the experiments. Material properties of these bars were assessed through testing using the reduced section method outlined in ASTM 317-17 [4]. The material properties are provided in Table 3-3 and stress-strain plots of the steel reinforcing bars are shown in Figure 3.8:

Table 3-3: Steel reinforcement material properties

Steel Type	f_y (ksi)	ϵ_y	f_u (ksi)	ϵ_u
Gr. 60 A706	74.4	0.0058	104.6	N/A
Gr. 80 A706	98.1	0.0040	133.2	N/A

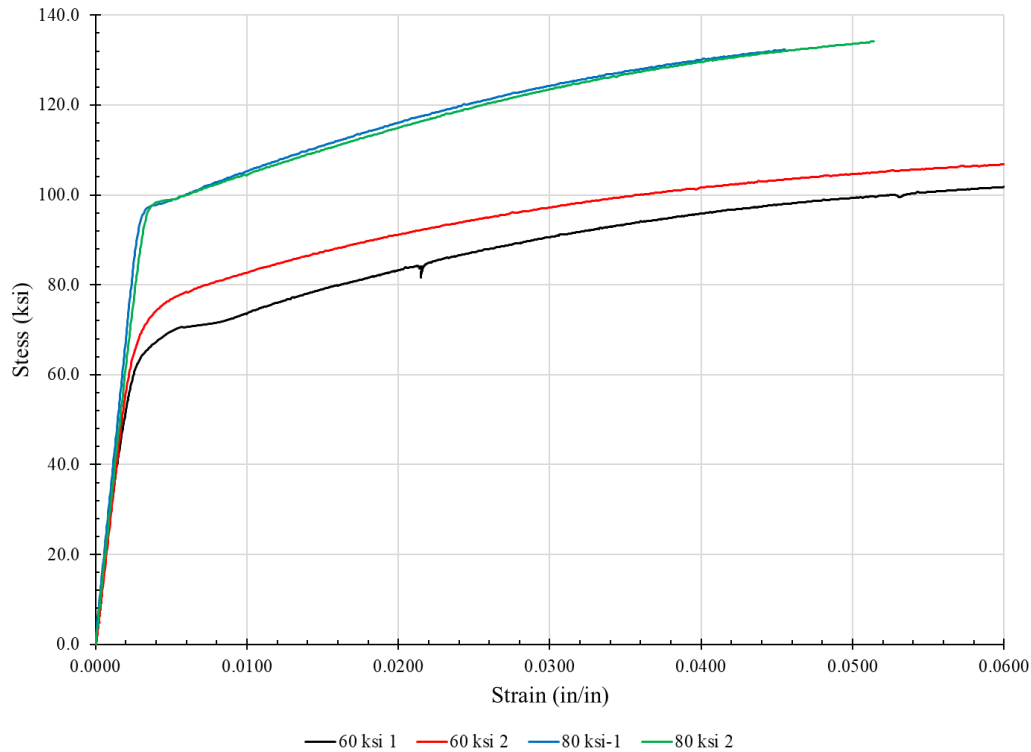


Figure 3.8: Stress-strain plot of the steel reinforcement

3.3 Test Setup

The experimental setup is outlined in Figure 3.9 and Figure 3.10. The specimens were tested horizontally and were loaded using a hydraulic actuator with a load capacity of 450-kips. A reaction block, pre-stressed to the floor of the lab, was used to react the applied loads. The loading protocol consisted in quasi-static, monotonically increasing loading and the test was run in displacement control. The swivel was attached at the end of the actuator to reduce out-of-plane loading, and it was supported by a wide-flange beam. To reduce friction between the swivel and the support beam, the swivel sat on a PTFE plate set on top of the silicone greased stainless steel surface (Figure 3.12). Series of plates and a one quarter inch rubber pad were placed between the specimen and the swivel to distribute the load across a designated 10 inches by 10 inches square. Because of the placement of the actuator, the specimen needed to be elevated from the ground. A wide-flange steel beam was used as support, and a stainless steel sheet was welded on top of the steel beam with silicone grease applied between the specimen and the stainless steel sheet to minimize friction. A GRM cotton duck pad was placed between the reaction block and the specimen to help distribute the load evenly across the designated 10 inches by 10 inches square and to account for any potential alignment issues (circled in Figure 3.11).

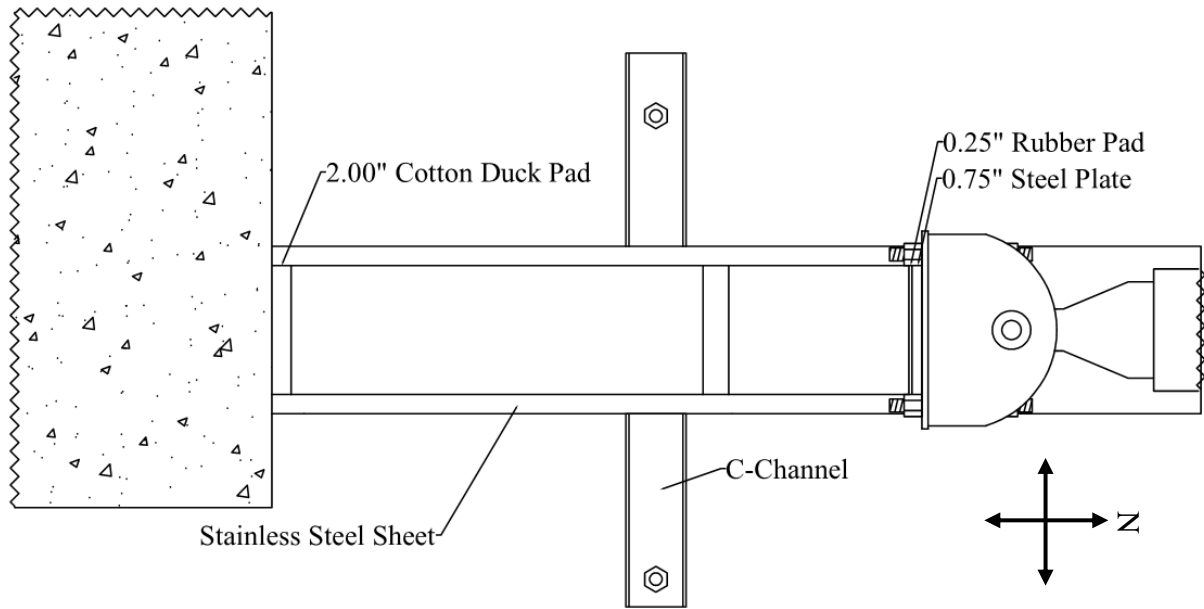


Figure 3.9: Test Setup (Plan View)

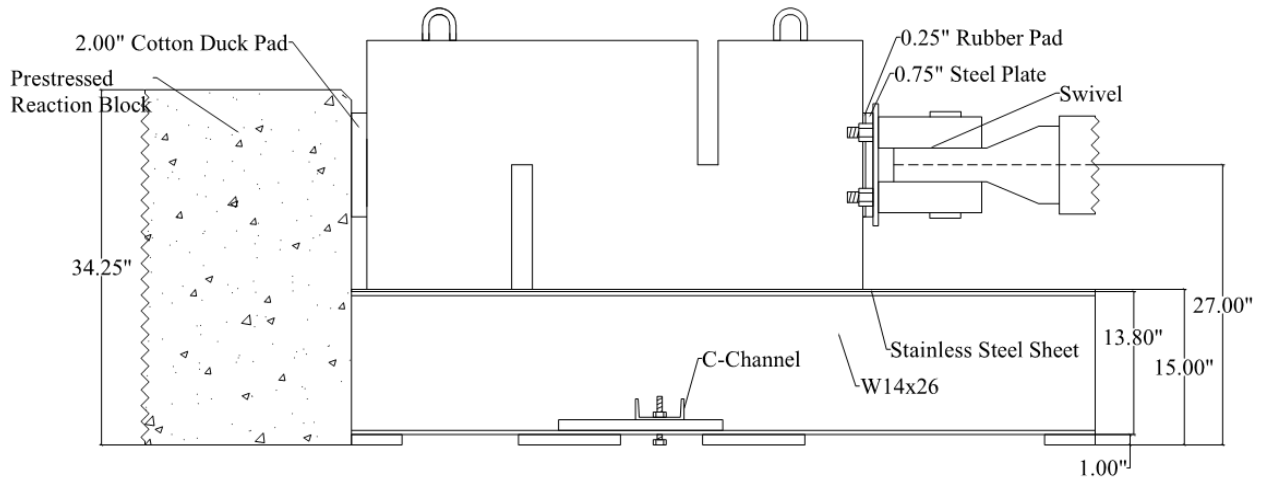


Figure 3.10: Test Setup (Elevation View, East side)



Figure 3.11: Picture of the test setup. The wide flange beam was anchored down with two C-channels.

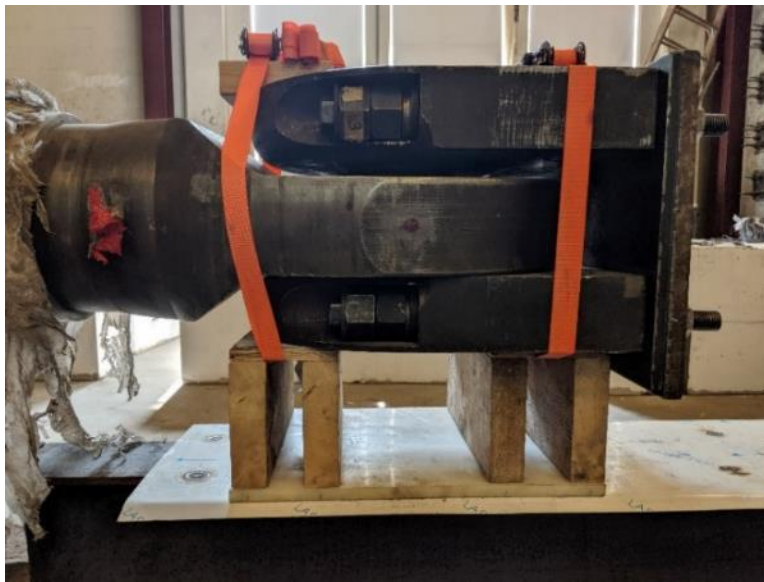


Figure 3.12: Photograph of the actuator head.

3.4 Instrumentation

Four key parameters were monitored throughout each test: the applied load, the strain of the interface reinforcement, the relative slip displacement between the two halves of a specimen, and the vertical separation (i.e. crack width) between the two halves of the specimen. The test set that includes a view of the instrumentation used is shown in Figure 3.13 and in Figure 3.17. The

actuator had a built-in load cell that was used to measure the applied load throughout the tests. Strain gauges were used to capture the strain of the interface reinforcement. String potentiometers and spring return linear sensors (Duncan potentiometers) were used to capture relative slip displacement. An Optotrak system was used to monitor the position in space of a grid of LED markers glued to one side of the specimen. The relative displacement between targets was used to compute the interface relative slip displacement and width.

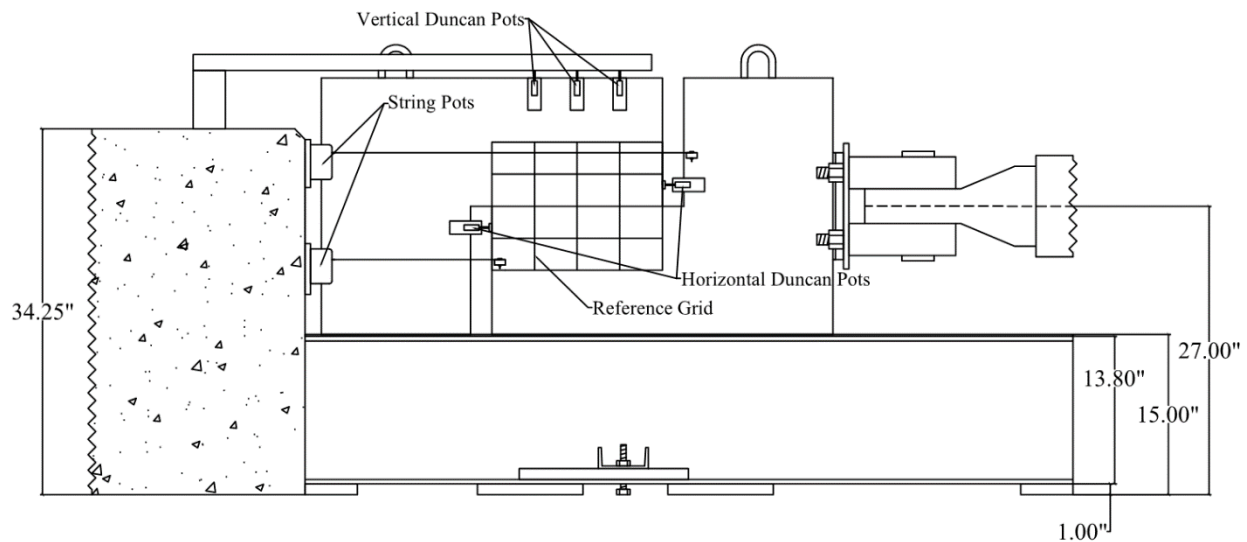


Figure 3.13: Drawing of the test setup with instrumentations (Elevation view, East side).

3.4.1 Strain Gauge

The strain gauges were primarily used to capture strain in the axial direction. Monitoring the strain level in the steel reinforcement crossing the interface was important to adequately interpret the experimental results and understand the mechanics of the specimens' response. High elongation strain gauges were used, and they were attached 2 inches away from the interface to not affect the bond at the interface. Because the strain gauges were further away from the interface, any local yielding behavior at the interface was not captured.

3.4.2 String Potentiometers and Duncan Potentiometers

The string potentiometers were placed on the reaction block to track the overall horizontal movement of the specimen (Figure 3.14). The Duncan potentiometers were placed between the two horizontal gaps of the specimen to measure the relative slip displacement. The other three Duncan potentiometers placed at the top of the specimen measured uplift and rotation (Figure 3.15).



Figure 3.14: String potentiometer attached to the reaction block



Figure 3.15: Duncan potentiometers used during the test.

3.4.3 Optotrak

The Optotrak camera captured the movement of the flashing LED markers at a given frequency of 4 Hz and generated positional data of the LED markers. The location of the LED markers and their designated numbers are shown in Figure 3.17. These positional data were compared with physical instrumentations to verify each instrumentations' accuracy. Figure 3.16 compares the displacement data from the string potentiometer and the displacement data calculated from the Optotrak positional data.

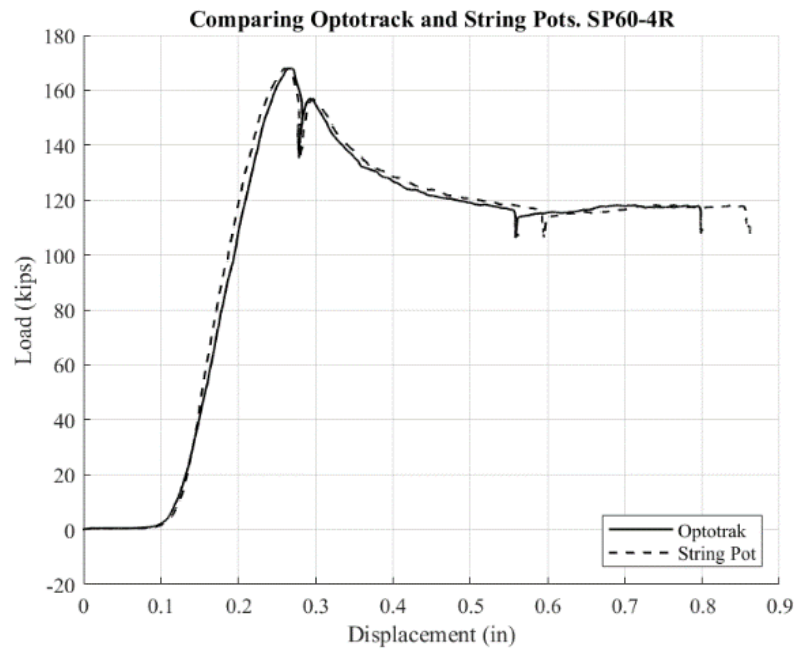


Figure 3.16: Plot comparing the displacement readings from the Optotrak markers and string potentiometer.

Referencing the LED marker numbers shown in Figure 3.17, horizontal displacement between pairs of LED markers #7 and #13, #8 and #14, #9 and #15, #10 and #16, #11 and #17, and #12 and #18 were used to represent the relative slip displacement between two halves of the specimen. The vertical displacement between the same pairs of LED markers were used to represent the crack width. Figure 3.18 show the photograph of a specimen with LED markers.

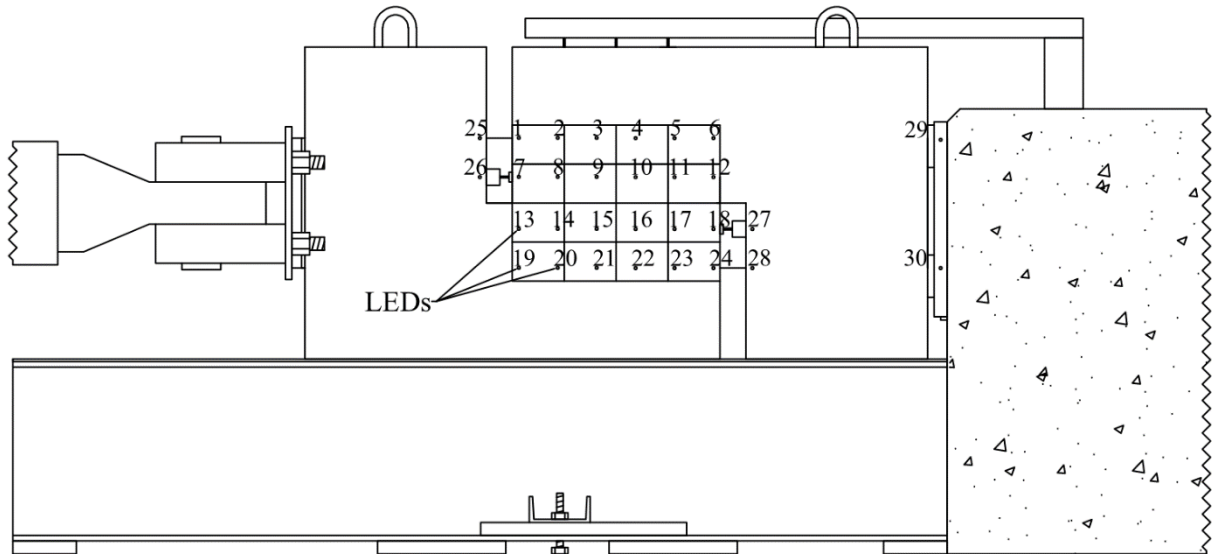


Figure 3.17: Drawing of the test setup with Optotrak LED markers and designated marker numbers (Elevation view, West side).

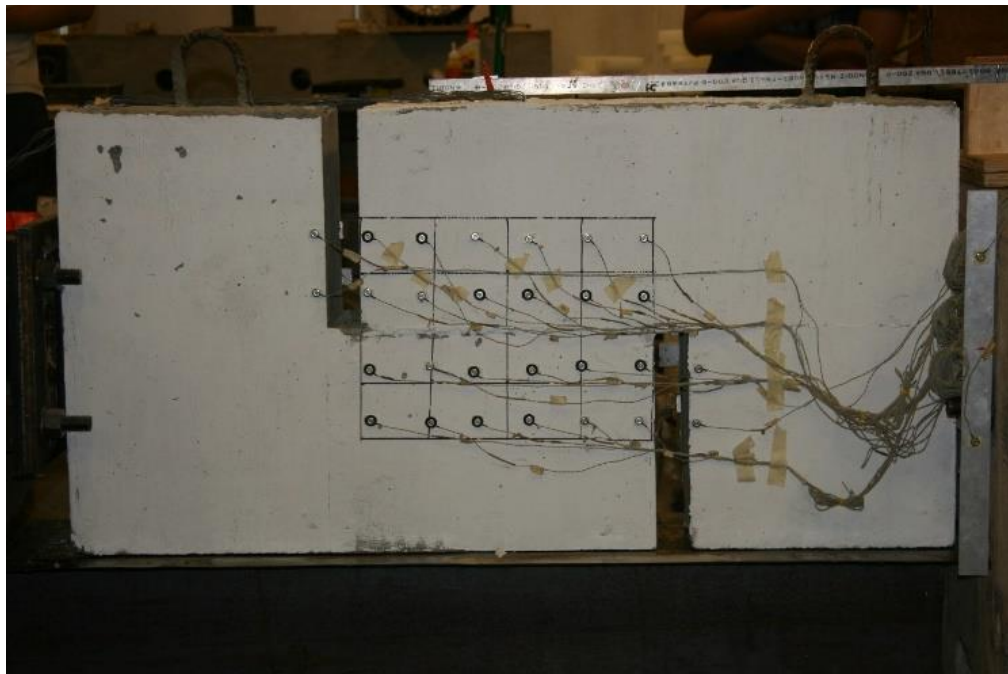


Figure 3.18: Picture of a specimen with LED markers (West side)

Chapter 4: Experimental Results

The test program was conducted to investigate the impact of several key variables including roughening using retarders, strength of the reinforcement, and the number of reinforcing bars crossing the interface. This chapter presents the test results for each specimen including key observations made during and after the tests along with photographs, and relevant plots and tables. Crack patterns and visible damage at different stages of the tests are presented through photographs. The force-displacement graphs and force-crack width graphs show the qualitative behavior of the specimens.

Salient experimental data is provided in Table 4-1. The measured applied load, interface slip displacement and interface crack widths are reported. The residual shear load was reported as the load corresponding to additional interface slip of 0.15 inch from the peak slip displacement value. UW60S-2 and UW80S-2 do not have reported values of slip displacement and crack width because the instrumentations were faulty. Only value reported for those two specimens are the peak shear load and the residual load. The information is presented in five test series previously presented in Chapter 3 for better organization: test series 0, 60S, 80S, 60R, and 80R.

The variables in Table 4-1 are defined as follows:

- ρf_y is the theoretical clamping stress.
- V_{peak} is the peak shear load.
- Δ_{peak} is the interface slip displacement at V_{peak} .
- w_{peak} is the interface crack width at V_{peak} .
- $V_{residual}$ is the residual shear load.

Table 4-1: Summary Table

Specimen Properties					Measured Results			
Specimen	f'_c (psi)	f_y (ksi)	ρf_y (psi)	V_{peak} (kip)	Δ_{peak} (in)	w_{peak} (in)	$V_{residual}$ (kip)	
0	UW0S	5850	N/A	0	41.3	0.008	0.0003	N/A
	UW0R	5850			67.4	0.002	0.0003	
60S	UW60S-2	5650	74.4	290	99.1	N/A	N/A	48.2
	UW60S-4	5650		580	119.2	0.014	0.0064	99.0
	UW60S-6	5650		863	111.3	0.037	0.0116	96.8
	UW60S-8	5650		1153	157.6	0.025	0.0059	140.8
	UW60S-10	5650		1443	136.7	0.029	0.0117	125.5
	UW60S-12	5650		1734	156.8	0.035	0.0107	121.3
80S	UW80S-2	5650	98.1	383	88.1	N/A	N/A	49.2
	UW80S-4	5650		765	101.3	0.049	0.0176	86.3
	UW80S-6	5650		1138	109.7	0.040	0.0163	93.4
	UW80S-8	5650		1521	135.6	0.042	0.0130	116.2
	UW80S-10	5650		1903	158.8	0.027	0.0129	143.6
	UW80S-12	5650		2286	195.0	0.040	0.0081	134.5
60R	UW60R-4	5850	74.4	580	132.3	0.026	0.0145	88.1
	UW60R-6	5850		863	126.4	0.011	0.0040	101.9
	UW60R-8	5850		1153	167.8	0.021	0.0093	121.4
	UW60R-10	5850		1443	169.6	0.022	0.0055	137.5
	UW60R-12	5850		1734	173.9	0.022	0.0062	131.5
80R	UW80R-4	5850	98.1	765	131.0	0.015	0.0123	104.0
	UW80R-6	5850		1138	119.0	0.005	0.0017	98.1
	UW80R-8	5850		1521	174.7	0.039	0.0222	140.7
	UW80R-10	5850		1903	178.9	0.023	0.0097	133.4
	UW80R-12	5850		2286	153.9	0.014	0.0037	109.8

4.1 Testing Procedure

All specimens were tested using the same testing procedure. The specimens were subjected to displacement-controlled monotonically increasing horizontal load. When the applied load started to decline, or at peak shear load, the tests were paused to mark both primary and secondary cracks, measure crack width, and record the displacement changes in the horizontal gaps between the two halves of the specimen. Post-peak response was investigated by imposing a series of actuator displacement of 0.3 inch, pausing every time to inspect the specimens and take crack width and slip displacement measurements. The 0.3-inch increment was chosen arbitrarily. The tests were stopped completely when the instrumentations were at risk of being damaged or when significant spalling occurred.

4.2 Typical Specimen Behavior

The tests are broken down into three stages: pre-peak, peak, and post-peak. Most of the specimens, excluding UW0S and UW0R (discussed separately), had similar responses. The following descriptions of the specimen behavior are considered typical specimen behavior:

- No noticeable cracks along the interface formed before the peak shear load.
- Sets of two vertical cracks at the top and the bottom of the specimen and long horizontal cracks near the actuator and the cotton duck pad formed before peak.
 - These were secondary cracks that occurred outside of the critical region and did not affect the experimental results.
- At peak, one long continuous crack formed along the interface plane (i.e. primary crack) and the applied load started to decline.
- After peak, some specimens maintained that residual load until the end of test while other specimens had increasing or decreasing load towards the end of the test.
- Spalling occurred during the post-peak stage as the steel reinforcements mobilized and experienced substantial rotation, causing large concrete bodies to spall outward. Most of the spalling occurred around the gap area and at the vicinity of the interface.

Crack patterns and spalling described above can be seen in photographs of the specimens in the following section. Details for each specimen, including any unexpected aspects of the responses are presented in following sections.

4.3 Individual Specimen Behavior

4.3.1 Test Series 0: Specimens without Reinforcement

UW0S had no reinforcement crossing a smooth interface. Despite having no reinforcement, it reached a nontrivial peak shear load of 41.3 kips, occurring at a slip displacement of 0.008 inch and an interface crack width of 0.0003 inch. The peak response was very brittle with the load immediately dropping to zero after peak. The test was stopped at peak as shown in Figure 4.1. The top half of the specimen was removed to observe the interface after the test, and this is photographed in Figure 4.3. The interface was clean and smooth with no exposed aggregate.

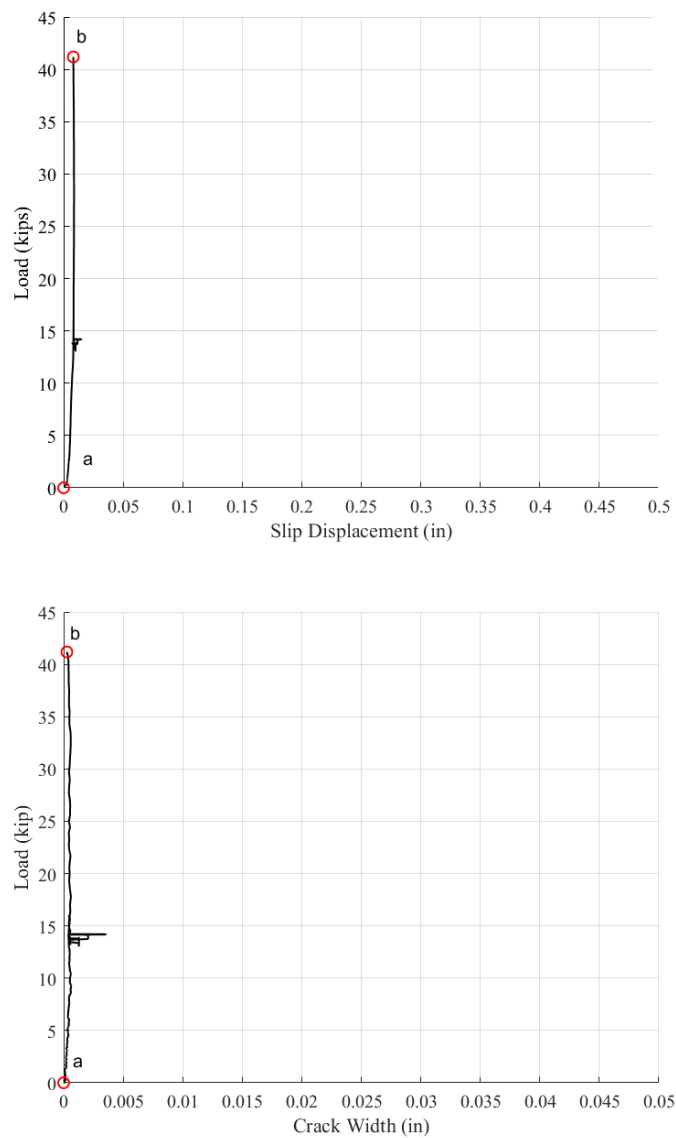


Figure 4.1: UW0S load-slip displacement graph (top) and load-crack width graph (bottom). The letters in the graphs reference different stages and photographs in Figure 4.2

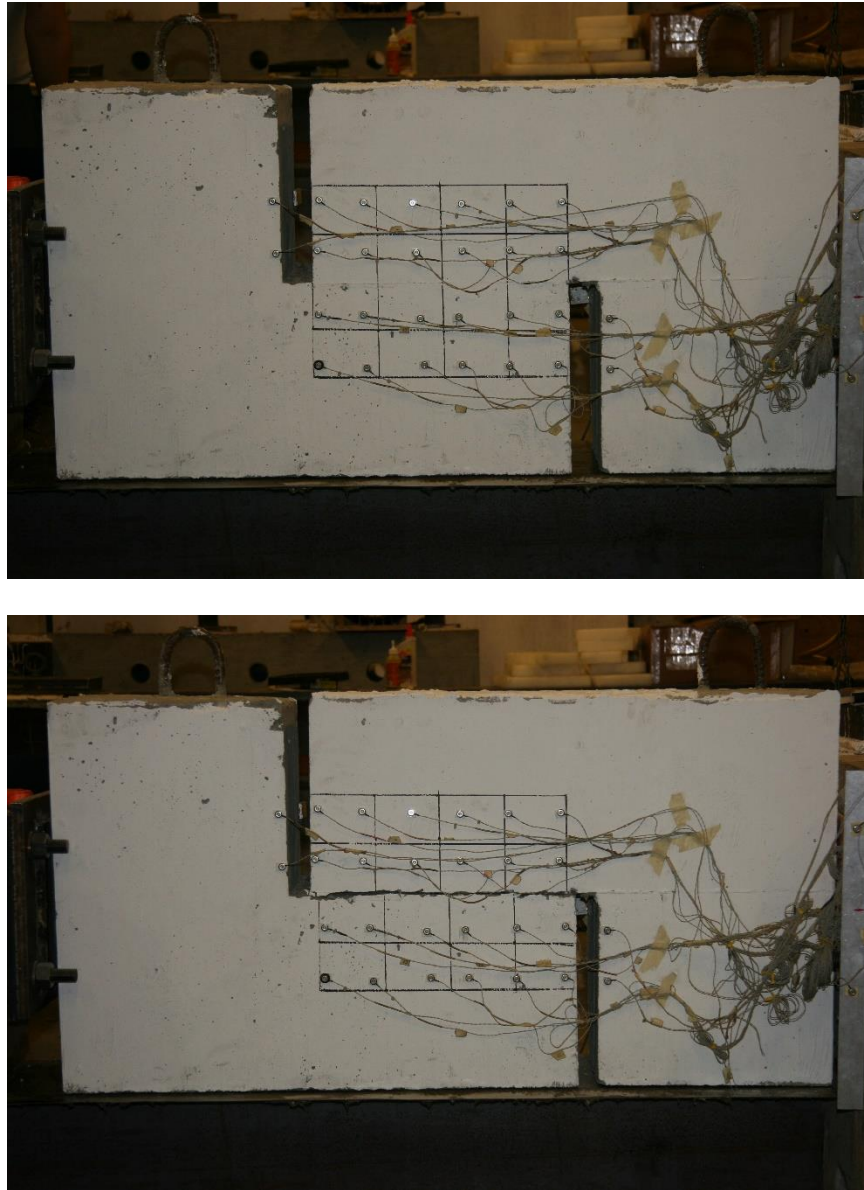


Figure 4.2: Photographs of UWOS during the test: a) start of test (top), and b) end of test (bottom).



Figure 4.3: Photograph of the interface after test (UW0S)

Similar to UW0S, UW0R had no reinforcement crossing an interface. The only difference between the two specimens was that the interface was roughened for UW0R as discussed in Chapter 3. The peak shear load was 67.4 kips, occurring at a slip displacement of 0.002 inch and an interface crack width of 0.0002 inch. After the primary crack along the interface formed, the applied load dropped to zero and the test was stopped. Upon post-test inspection, the interface appeared rough with craters and partially exposed aggregate distributed evenly throughout the interface as shown in Figure 4.6. None of the aggregate appeared sheared-off, which suggest that the weakness of the cold joint was the bond between the aggregate and the cement matrix.

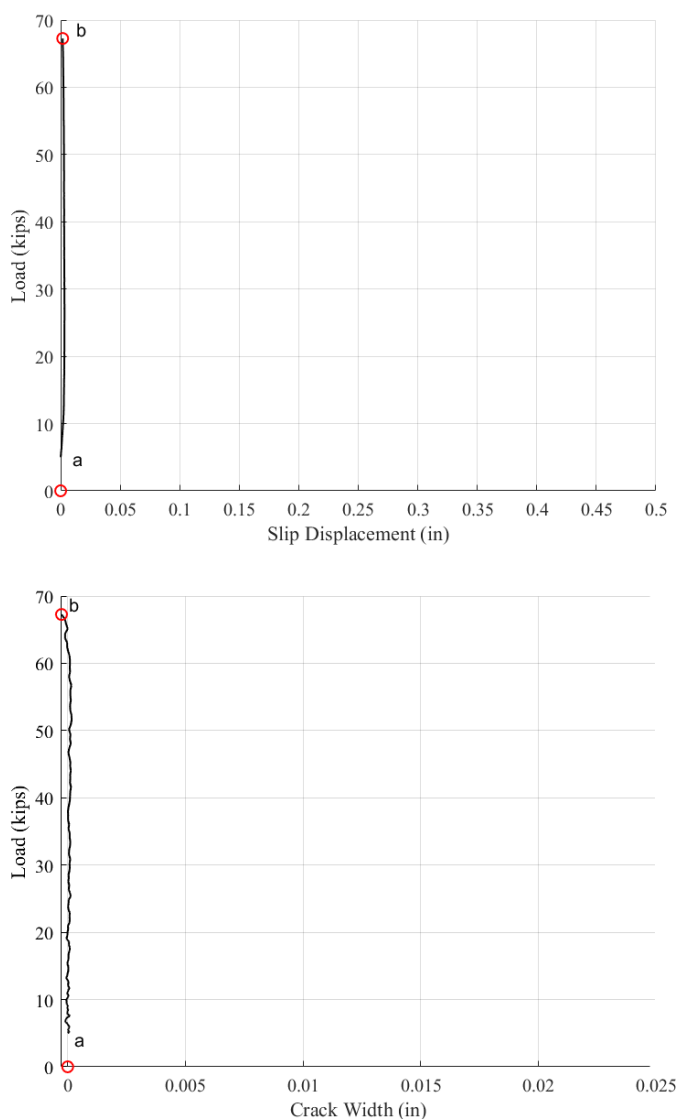


Figure 4.4: UW0R load-slip displacement graph (top) and load-crack width graph (bottom). The letters in the graphs reference different stages and photographs in Figure 4.5



Figure 4.5: Photographs of UW0R during the test: a) start of test (top), and b) end of test (bottom).



Figure 4.6: Photograph of the interface after test (UW0R)

4.3.2 Test Series 60S: Specimens with 60 ksi Reinforcement Crossing a Smooth Interface

This series consisted of six specimens with 2 to 12 74.4 ksi (60 ksi specified) steel reinforcing bars crossing the smooth interface. The theoretical clamping stress ranged from 290 psi to 1,734 psi.

UW60S-2 had two No. 5 60 ksi reinforcing bars crossing a smooth interface. It reached a peak shear load of 99.1 kips. Because the instrumentations provided faulty data, only the load-count graph is reported (Figure 4.7). After activation of the primary crack along the interface, the applied load dropped to 48.2 kips; this load was maintained until the end of test as shown in the Figure 4.7. Spalling occurred around gap; this is circled in red in Figure 4.8-c. At this stage, there was noticeable out-of-plane twisting. This was most likely caused by the fact that this specimen had two reinforcement bars crossing the interface that were not sufficient to provide enough out-of-plane stability when the reinforcing bars were deforming and rotating. At the end of the test, significant spalling occurred around the interface plane, and removing some concrete around the interface revealed that the reinforcement had rotated. The photographs below (Figure 4.8, Figure 4.9, and Figure 4.10) provide a qualitative sense of the specimen slip displacement, spalling, and reinforcement rotation.

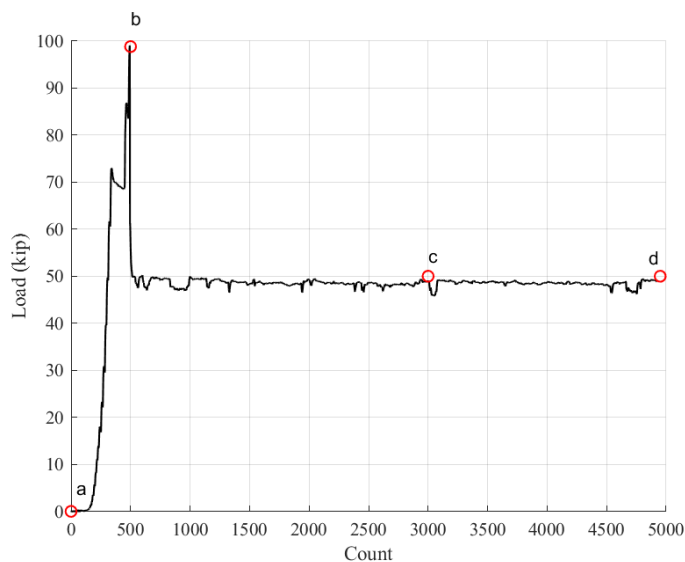


Figure 4.7: UW60S-2 load-count graph. The letters on the graph reference different stages and photographs in Figure 4.8.

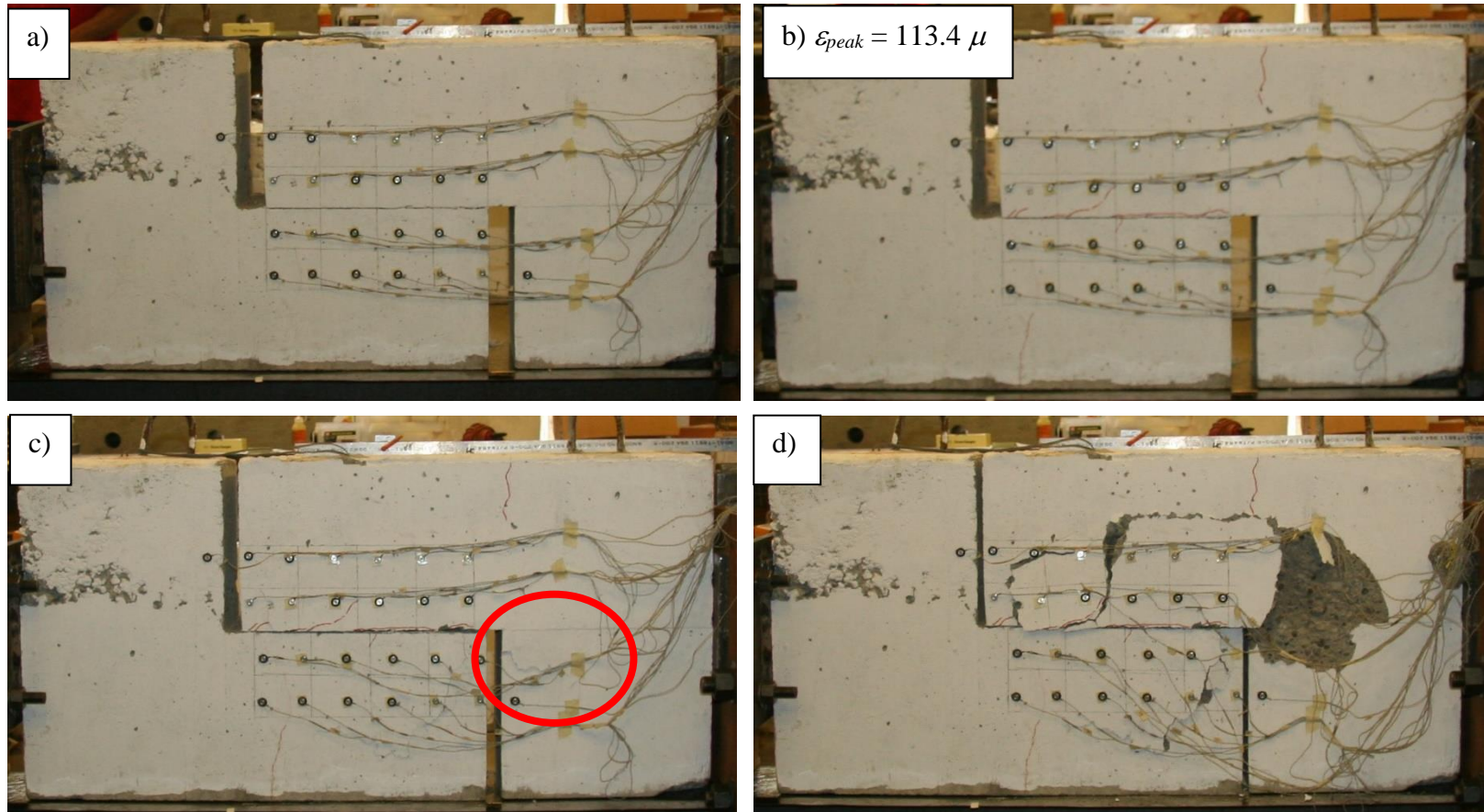


Figure 4.8: Photographs of UW60S-2 at different stages of the tests: a) start of test b) peak c) residual d) end of test. The average strain-gauge value at peak load is included in the photographs.



Figure 4.9: Close up of the revealed reinforcement after test (UW60S-2 West side).



Figure 4.10: Close up of the revealed reinforcement after test (UW60S-2 East side).

UW60S-4 had four No. 5 60 ksi reinforcing bars crossing a smooth interface. The peak load was 119.3 kips, occurring at a slip displacement of 0.014 inch, and an interface crack width of 0.006 inch. After peak load, as the load began to degrade, large diagonal crack propagated from near the gaps through the interface as shown in Figure 4.12-c. This secondary crack was independent of the primary crack occurred along the interface plane at peak. The cracks and spalling that occurred after peak load resulted from the movement of the reinforcing bars and did not affect the experimental results. Post-peak, the specimen reached a stable residual load of 98.9 kips. Unlike UW60S-2, any out-of-plane movement was insignificant. The reinforcement had less rigid body rotation and more shear deformation. The photographs below (Figure 4.12, Figure 4.13, and Figure 4.14) provide a qualitative sense of the specimen slip displacement, spalling, and reinforcement rotation.

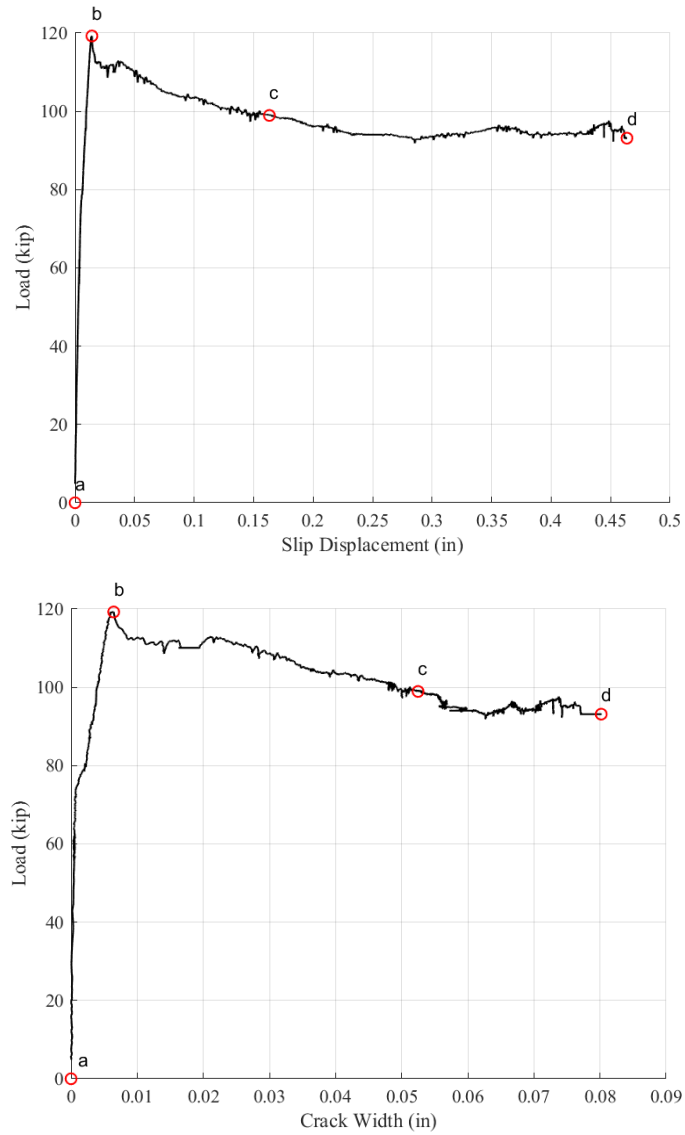


Figure 4.11: UW60S-4 load-slip displacement (top) and load-crack width graph (bottom). The letters in the graphs reference different stages and photographs in Figure 4.12.

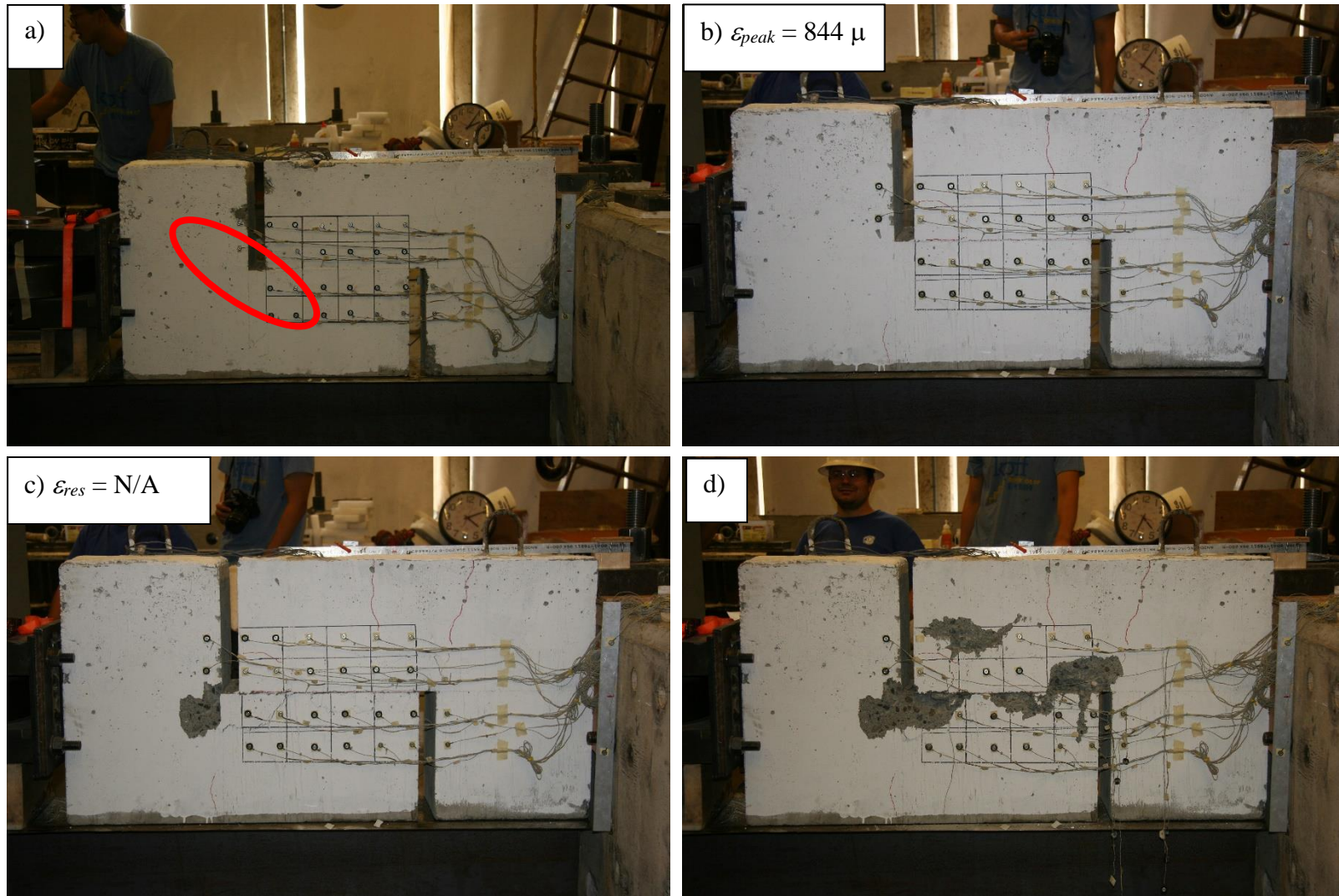


Figure 4.12: Photographs of UW60S-4 at different stages of the tests: a) start of test b) peak c) residual d) end of test. The average strain-gauge value at peak and at residual are included in the photographs.



Figure 4.13: Close up of the revealed reinforcement after test (UW60S-4 East side).



Figure 4.14: Close up of the revealed reinforcement after test (UW60S-4 West side).

UW60S-6 had six No. 5 60 ksi reinforcing bars crossing a smooth interface. The peak load was 111.3 kips at a slip displacement of 0.037 inch and interface crack width of 0.116 inch. The specimen's residual load was 96.8 kips. The load continued to drop until the end of test. The interface crack width decreased after the residual load (region between c and d in Figure 4.15). This behavior occurred in 3 out of 24 specimens (other specimens are discussed later). It was unclear on why this behavior occurred and why it did not affect slip displacement. It might have been caused by concrete around the interface being damaged a certain way. A large block of concrete broke off at the gap due to the rotating reinforcement pushing the concrete out towards the gap. This is highlighted in Figure 4.17.

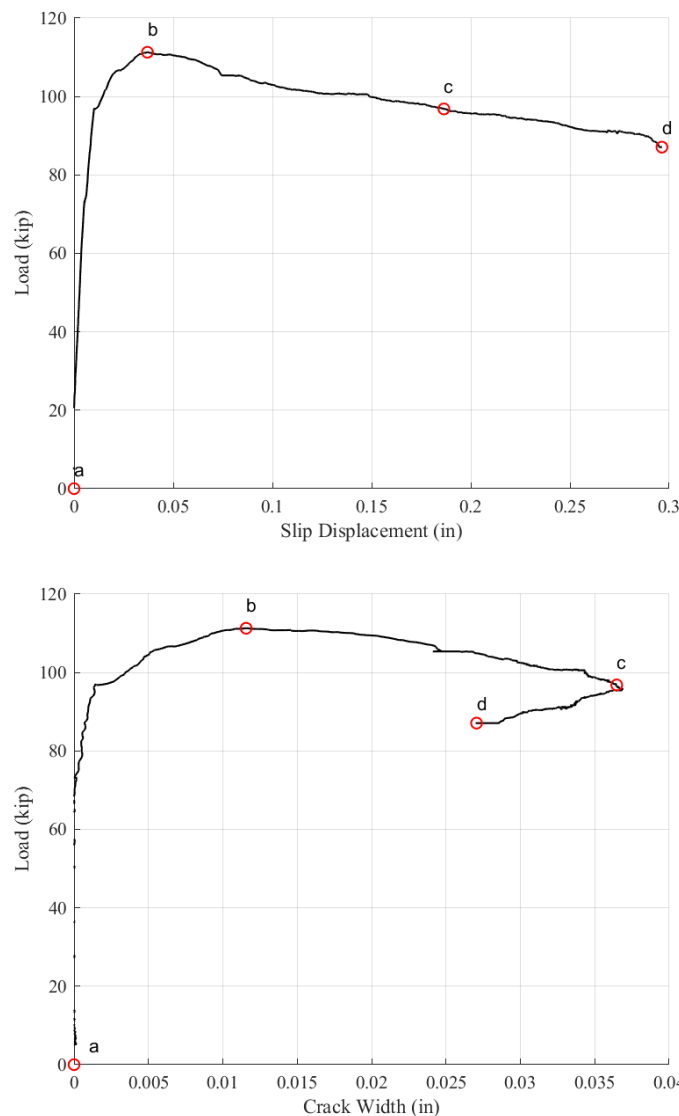


Figure 4.15: UW60S-6 load-slip displacement (top) and load-crack width graph (bottom). The letters in the graphs reference different stages and photographs in Figure 4.16.

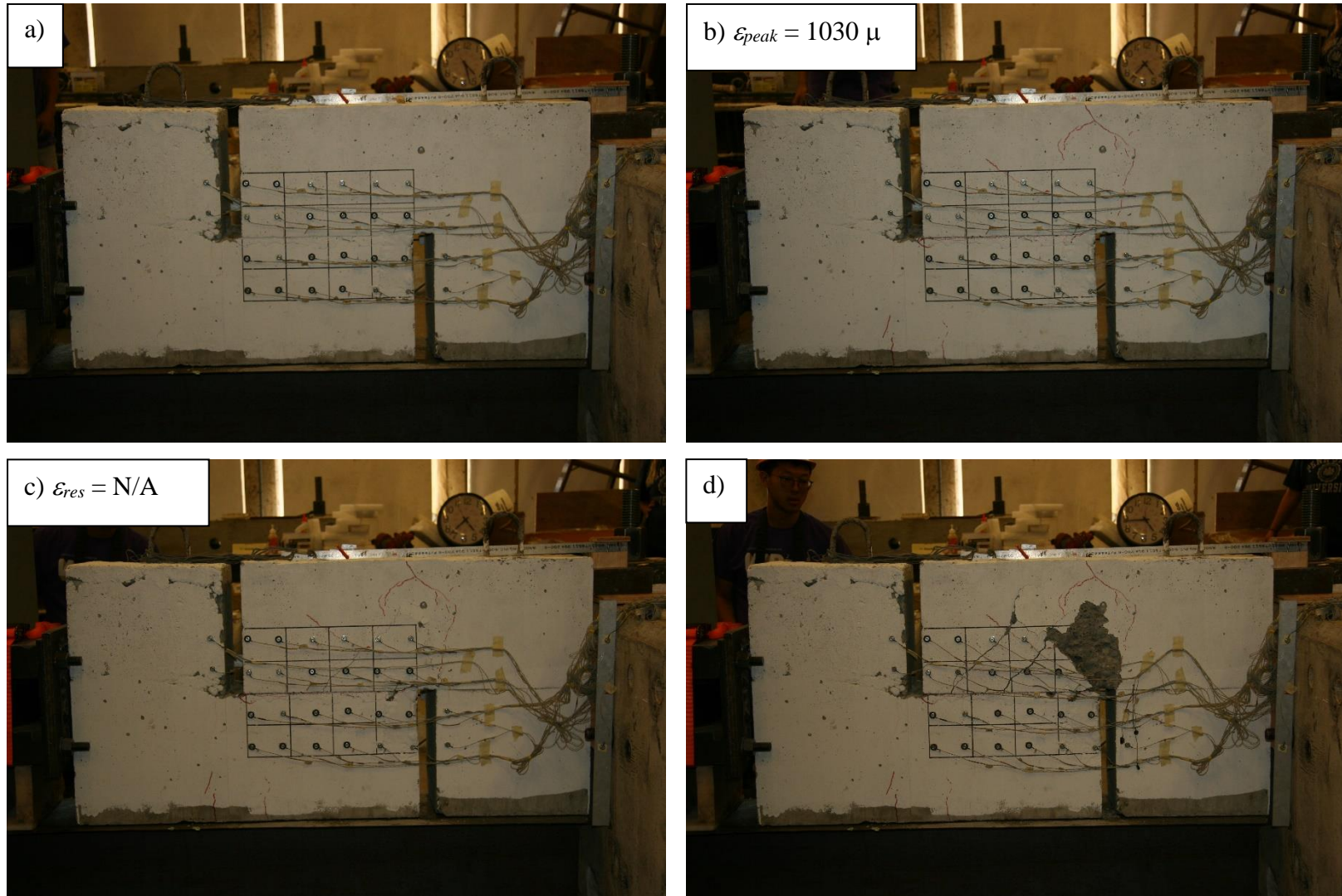


Figure 4.16: Photographs of UW60S-6 at different stages of the tests: a) start of test b) peak load c) residual d) end of test. The average strain-gauge value at peak load and at residual are included in the photographs.

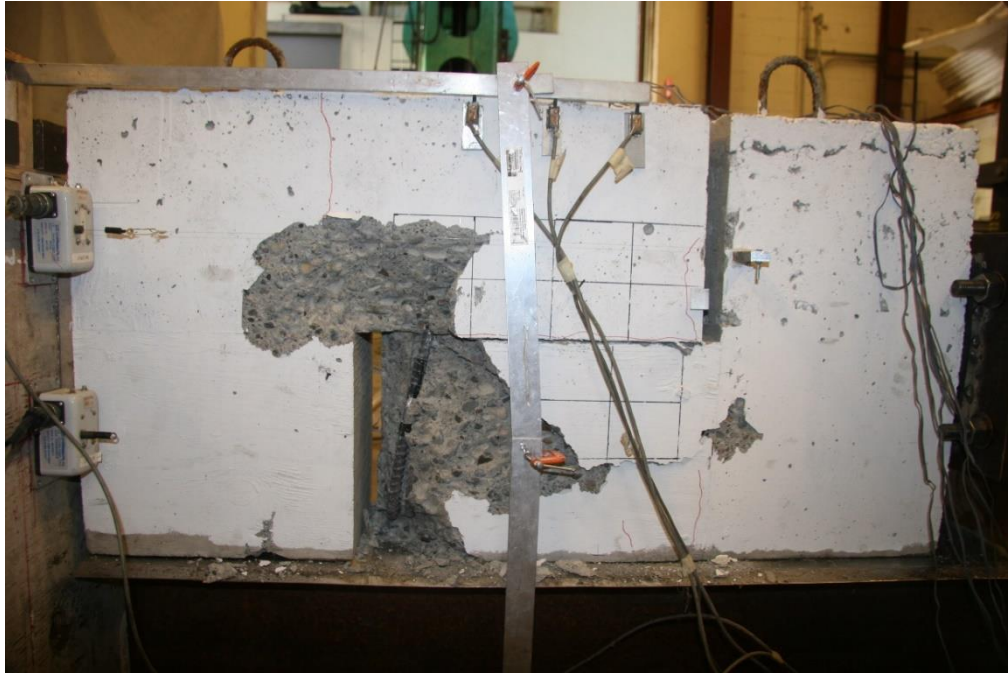


Figure 4.17: Photograph of the revealed reinforcement after test (UW60S-6 East side).

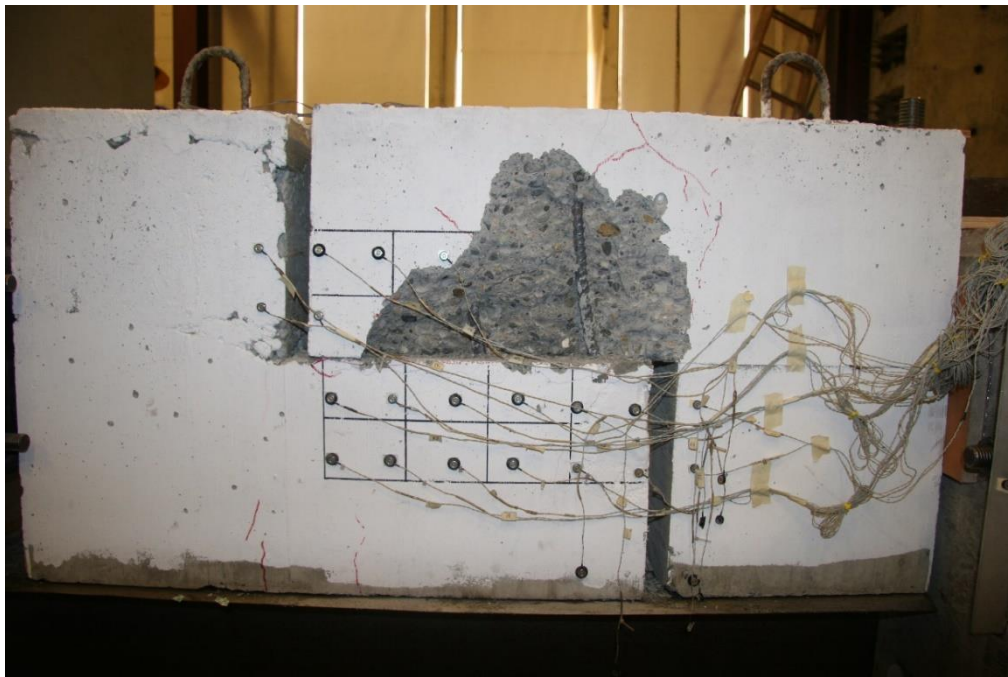


Figure 4.18: Revealed reinforcement after test (UW60S-6 West side).

UW60S-8 had eight No. 5 60 ksi reinforcing bars crossing a smooth interface. Nothing noticeable happened with respect to the specimens discussed earlier. The peak load was 157.5 kips, occurring at a slip displacement of 0.025 inch and an interface crack width of 0.006 inch. The residual load of 140.8 kips was maintained without notable fluctuation until the end of the test. The load-crack width plot (Figure 4.19) showed that there was a significant increase in crack width at the peak. The deformation of the reinforcing bars and the visible damage (e.g. spalling) were also consistent with those observed for other specimens. The photographs taken after the test are shown in Figure 4.21 and in Figure 4.22.

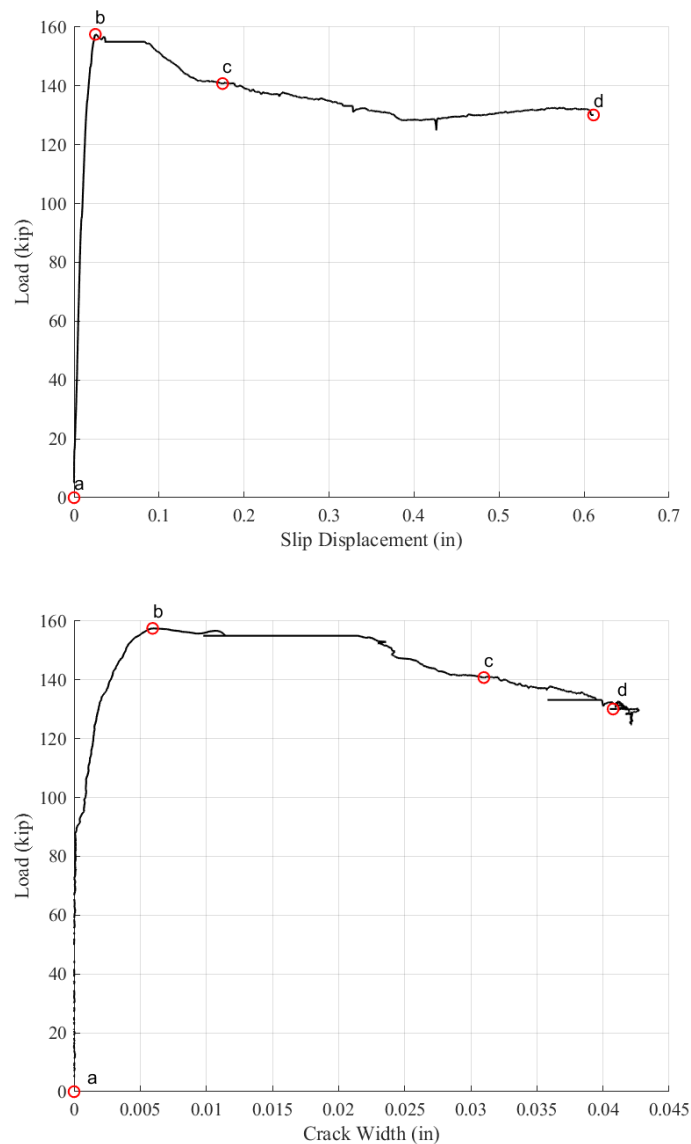


Figure 4.19: UW60S-6 load-slip displacement (top) and load-crack width graph (bottom). The letters in the graphs reference different stages and photographs in Figure 4.20.

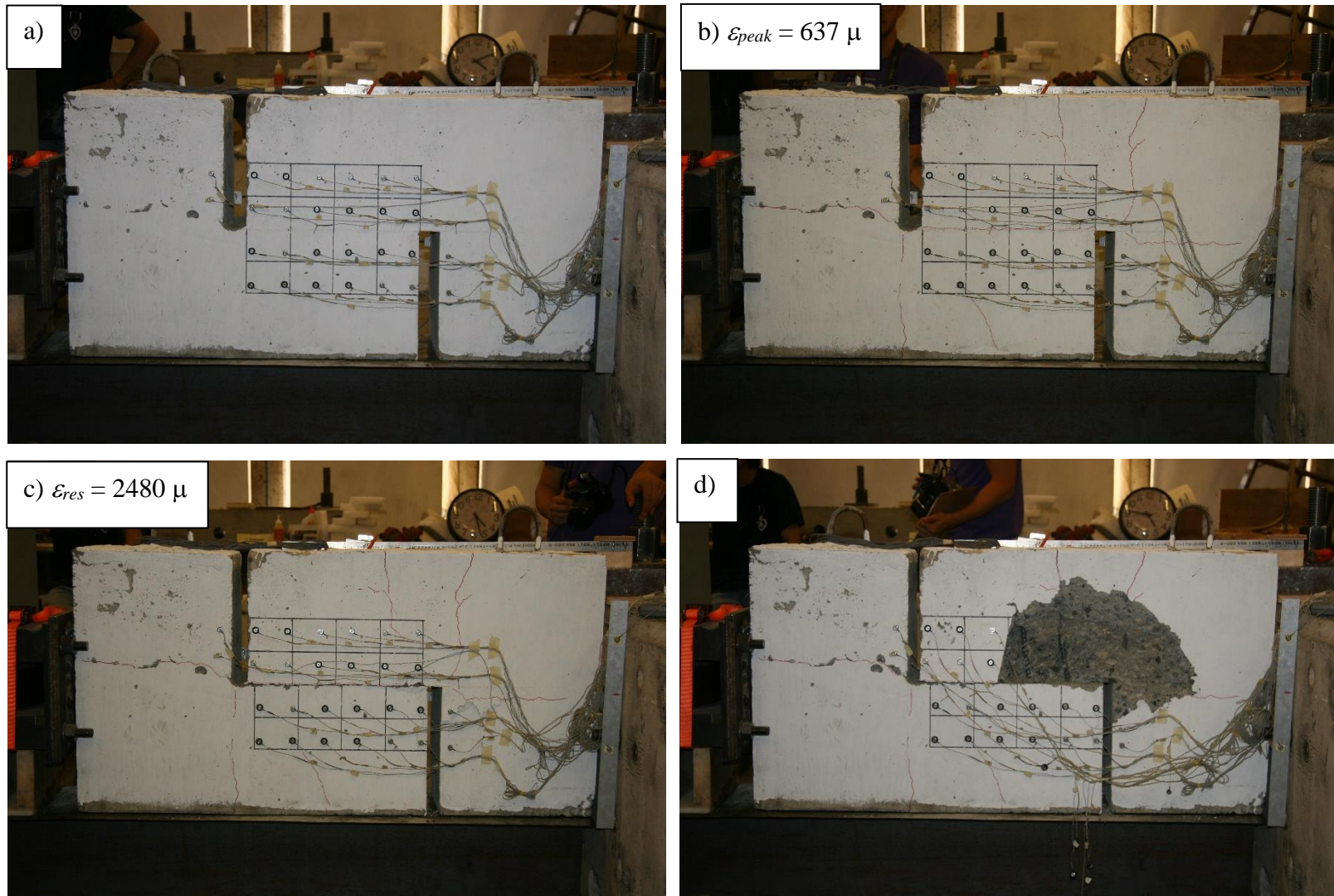


Figure 4.20: Photographs of UW60S-8 at different stages of the tests: a) start of test b) peak load c) residual d) end of test. The average strain-gauge value at peak load and at residual are included in the photographs.



Figure 4.21: Close up of the revealed reinforcement after test (UW60S-8 East side).



Figure 4.22: Close up of the revealed reinforcement after test (UW60S-8 West side).

UW60S-10 had 10 No. 5 60 ksi reinforcing bars crossing a smooth interface. The peak load was 136.6 kips, occurring at a slip displacement of 0.029 inch and an interface crack width of 0.012 inch. The residual load was 125.5 kips. Unlike other specimens, UW60S-10 had an increasing shear-transfer capacity after an initial post-peak drop, exhibiting a strain-hardening behavior shown in Figure 4.23. It is unknown why this behavior occurred. The crack width decreased and increased as the applied load was continuing the increase. It is of note that the damage pattern for this specimen was different and the bars were restrained by the intact concrete. The photographs below (Figure 4.24 and Figure 4.25) provide a qualitative sense of the specimen slip displacement, spalling, and reinforcement rotation.

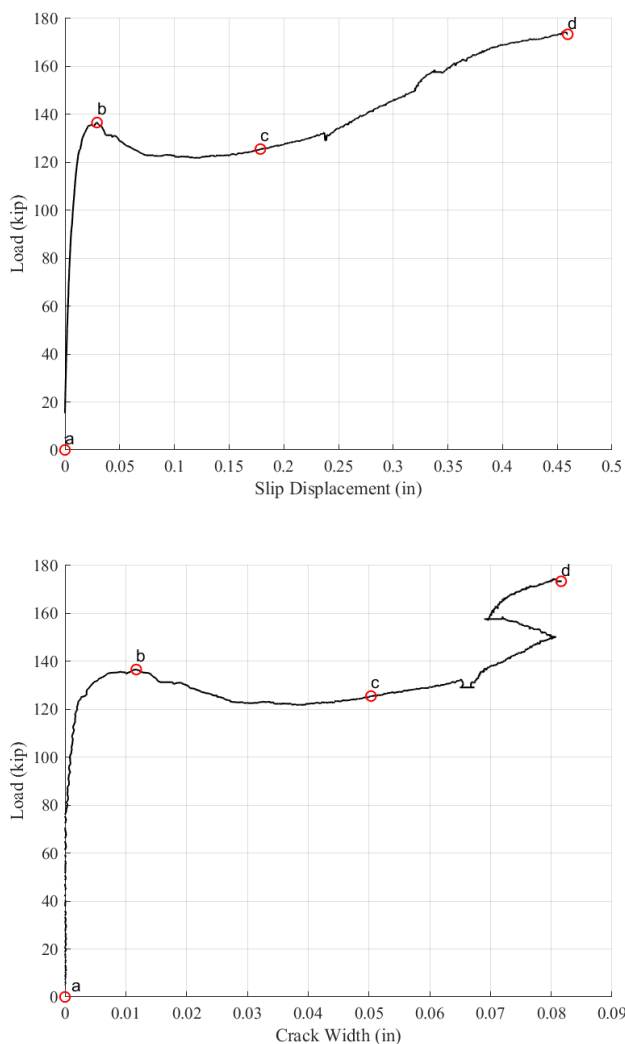


Figure 4.23 UW60S-10 load-slip displacement (top) and load-crack width graph (bottom). The letters in the graphs reference different stages and photographs in Figure 4.24.

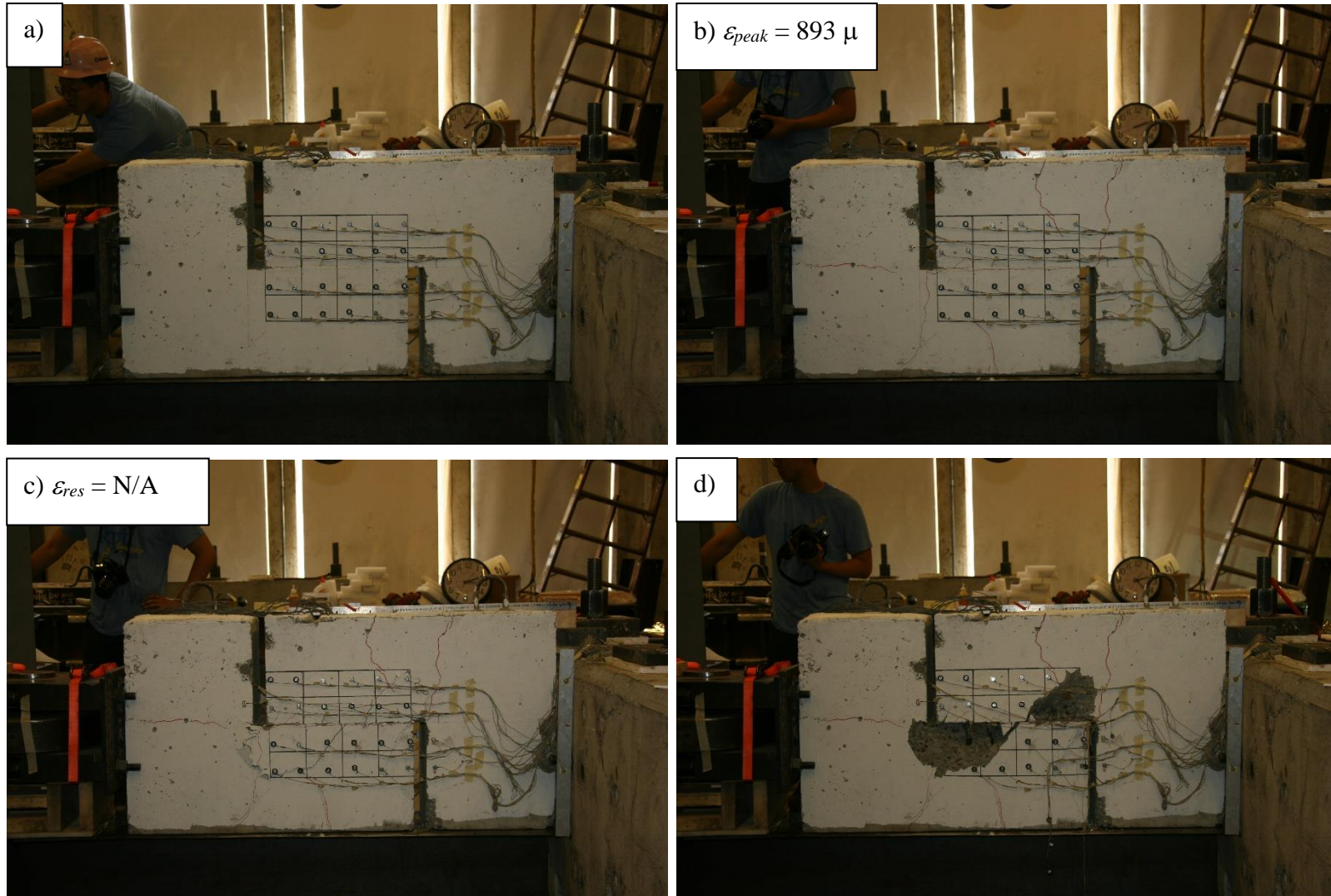


Figure 4.24: Photographs of UW60S-10 at different stages of the tests: a) start of test
 b) peak c) residual d) end of test. The average strain-gauge value at peak and at residual are included in the photographs.



Figure 4.25: Photograph of the revealed reinforcement after test (UW60S-10 East side).

UW60S-12 had 12 No. 5 60 ksi reinforcing bars crossing a smooth interface. The peak load was 156.8 kips, occurring at a slip displacement of 0.035 inch and an interface crack width of 0.011 inch. The applied load stabilized at a residual load of 121.3 kips after a gradual drop from the peak load (shown in Figure 4.26). The applied load increased after reaching a large slip displacement and increased until the end of the test. It is unknown why this behavior occurred. The damage at the concrete and the deformation of the reinforcing bars can be seen in Figure 4.27 and Figure 4.28

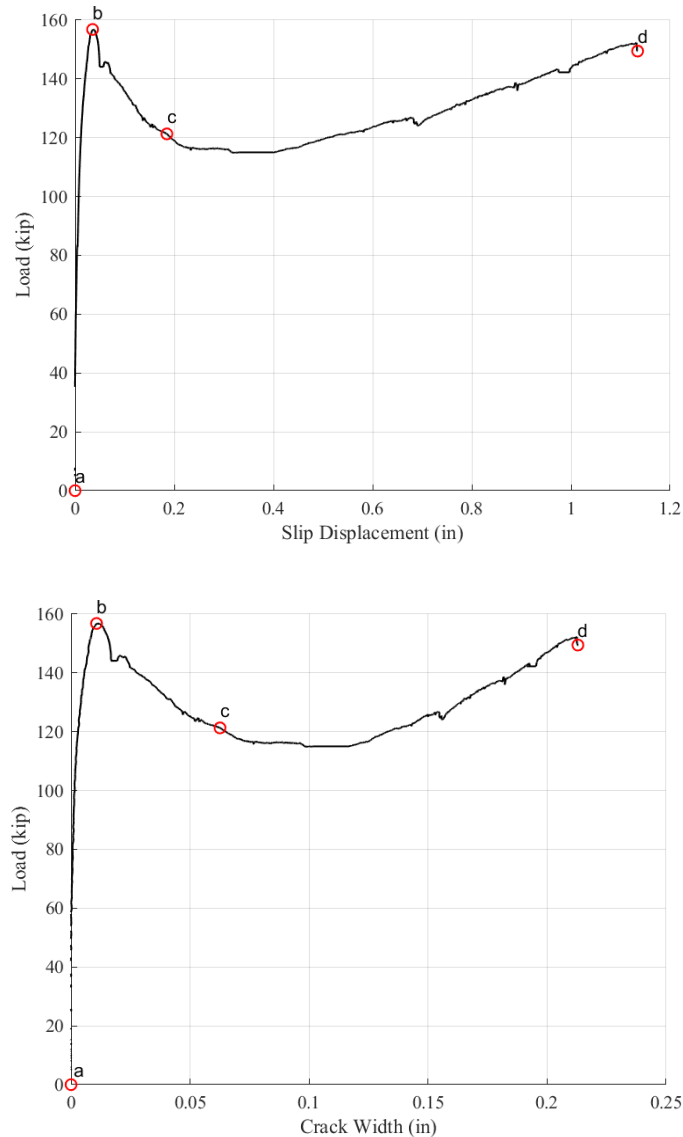


Figure 4.26 UW60S-12 load-slip displacement (top) and load-crack width graph (bottom). The letters in the graphs reference different stages and photographs in Figure 4.27.

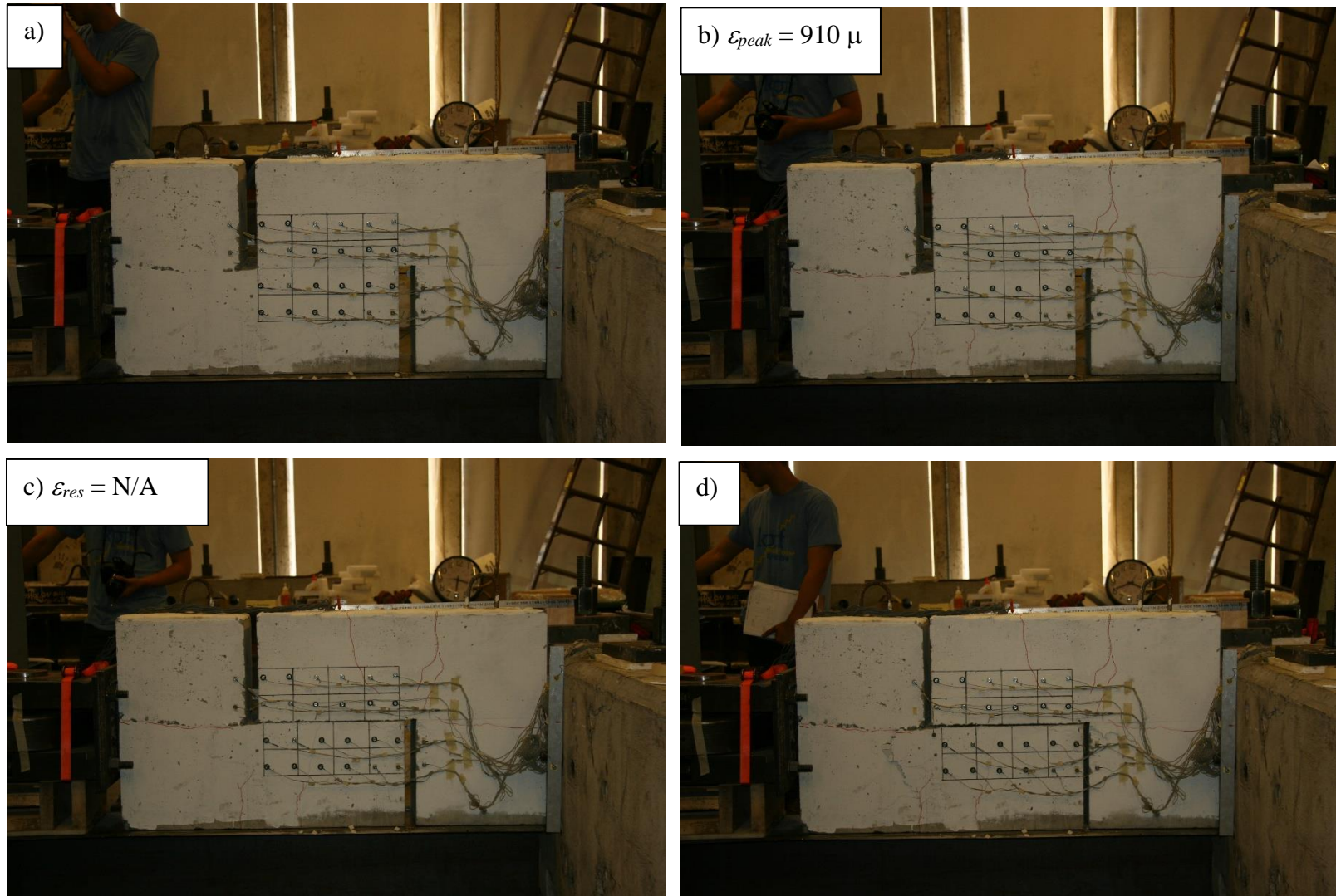


Figure 4.27: Photographs of UW60S-12 at different stages of the tests: a) start of test b) peak c) residual d) end of test. The average strain-gauge value at peak and at residual are included in the photographs.



Figure 4.28: Photograph of the revealed reinforcement after test (UW60S-12 East side).

4.3.3 Test Series 80S: Specimens with 80 ksi Reinforcement Crossing a Smooth Interface

This series consisted of six specimens with 2 to 12 98.1 ksi (specified 80 ksi) steel reinforcing bars crossing a smooth interface. The theoretical clamping stress ranged from 383 psi to 2,286 psi.

UW80S-2 had two No. 5 80 ksi reinforcing bars crossing a smooth interface. Its pre-peak and peak behaviors fit the descriptions of the typical specimen behavior. Because the instrumentations provided insufficient data, only the load-count graph is reported (Figure 4.29). The specimen reached a peak shear load of 88.1 kips. After the peak, applied load stabilized at a residual load of 49.2 kips as shown in Figure 4.29. Similar to UW60S-2, UW80S-2 had notable out-of-plane twisting. The photographs below (Figure 4.30, Figure 4.31, and Figure 4.32) provide a qualitative sense of the specimen slip displacement, spalling, and reinforcement rotation.

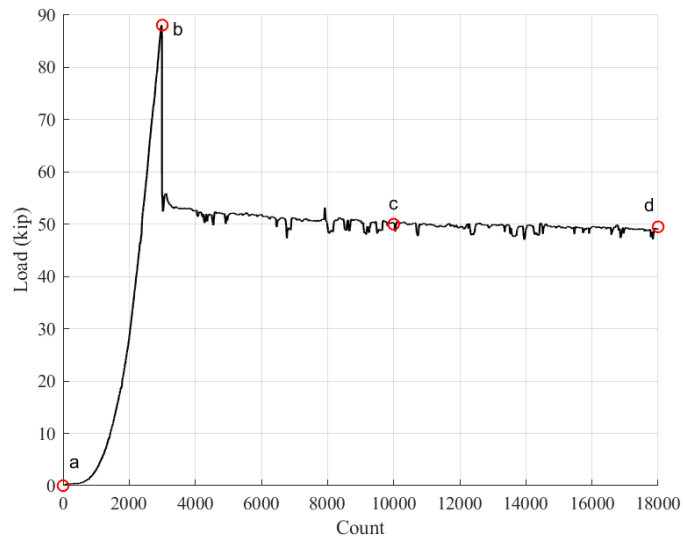


Figure 4.29: UW80S-2 load-count graph. The letters in the graph reference different stages and photographs in Figure 4.30.

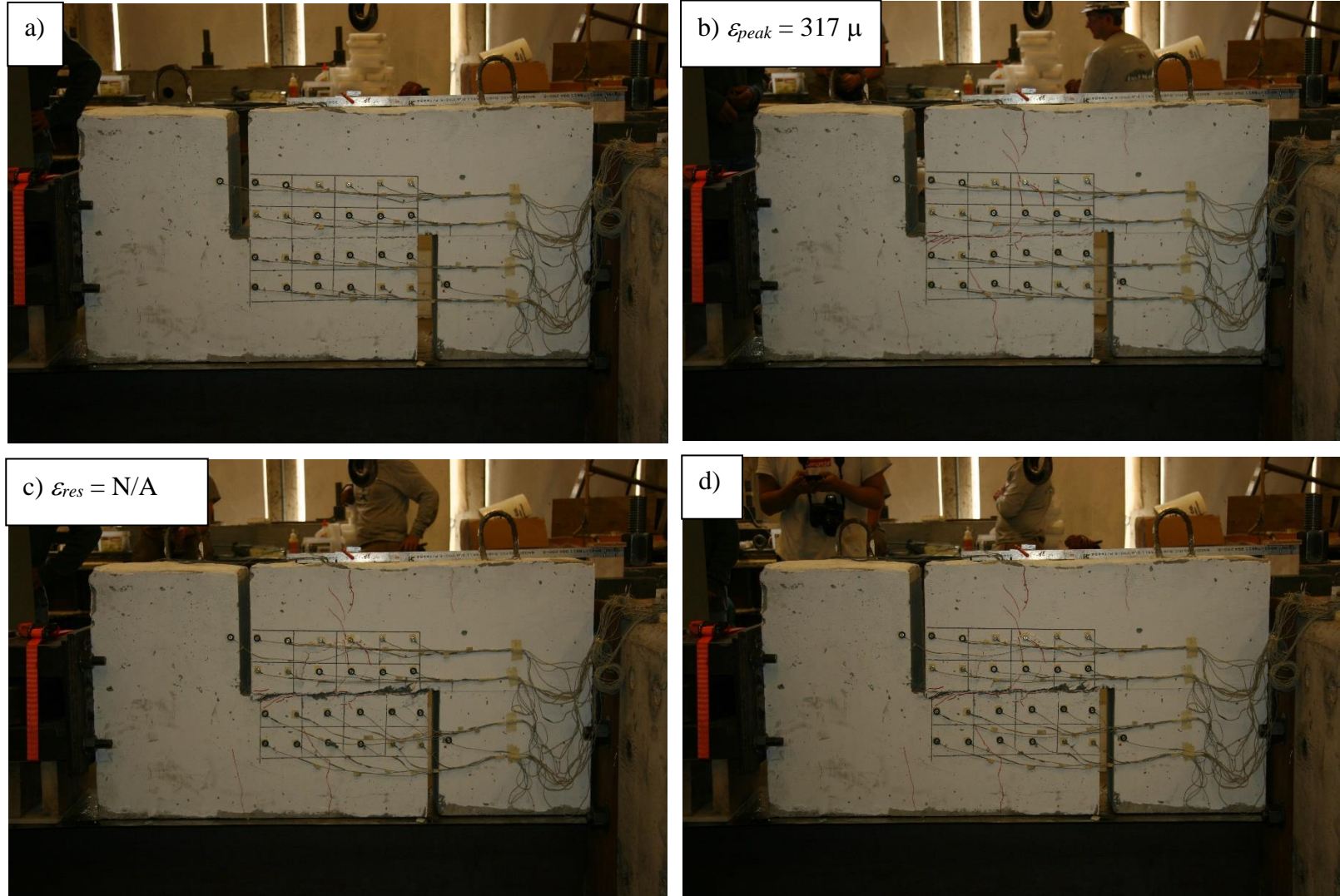


Figure 4.30: Photographs of UW80S-2 at different stages of the tests: a) start of test b) peak c) residual d) end of test. The average strain-gauge value at peak and at residual are included in the photographs.

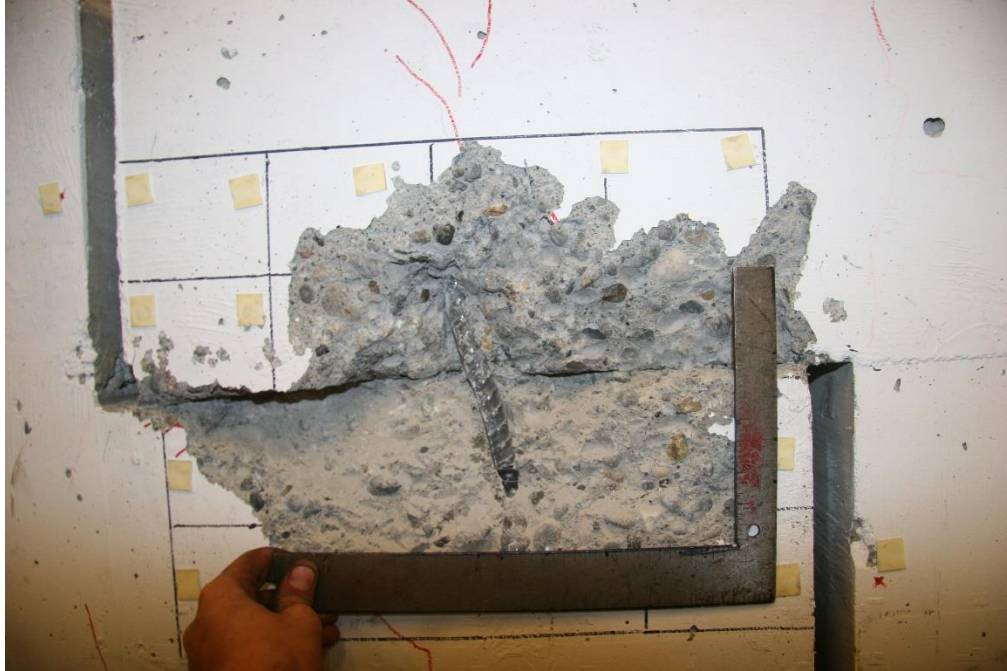


Figure 4.31: Photograph of the revealed reinforcement after test (UW80S-2 East side).



Figure 4.32: Close up of the revealed reinforcement after test (UW80S-2 West side).

UW80S-4 had four No. 5 80 ksi reinforcing bars crossing a smooth interface. This specimen displayed an unusual behavior right before peak; the applied load dropped suddenly, picked up immediately, and dropped gradually; this behavior is circled in red in Figure 4.33. Primary crack at the interface formed when the load dropped for the first time. It was unclear to why this behavior occurred. The peak load was 101.3 kips, occurring at a slip displacement of 0.049 inch, and an interface crack width of 0.018 inch. There was a sudden shift in the interface width measurement before the peak at around 75 kips of applied load (Figure 4.33), suggesting that a primary crack formed along the interface before the peak load. The applied load stabilized at a residual load of 86.3 kips and was maintained until the end of test. The photographs below (Figure 4.35 and Figure 4.36) show the state of the reinforcing bars after the test.

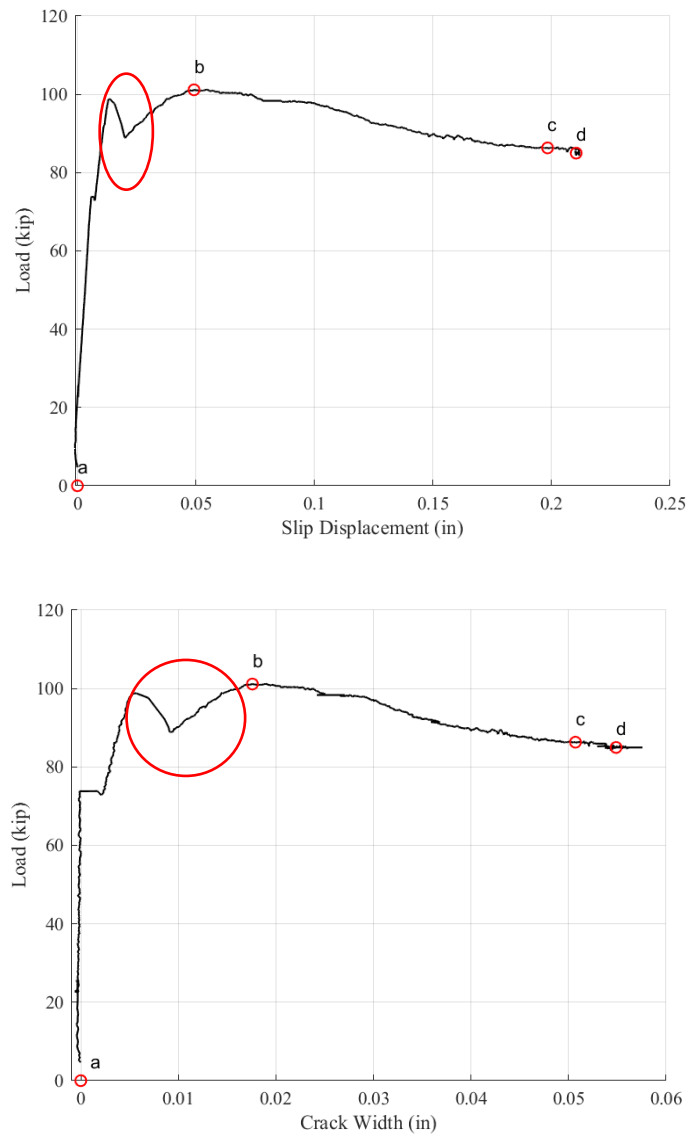


Figure 4.33 UW80S-4 load-slip displacement (top) and load-crack width graph (bottom). The letters in the graphs reference different stages and photographs in Figure 4.34.

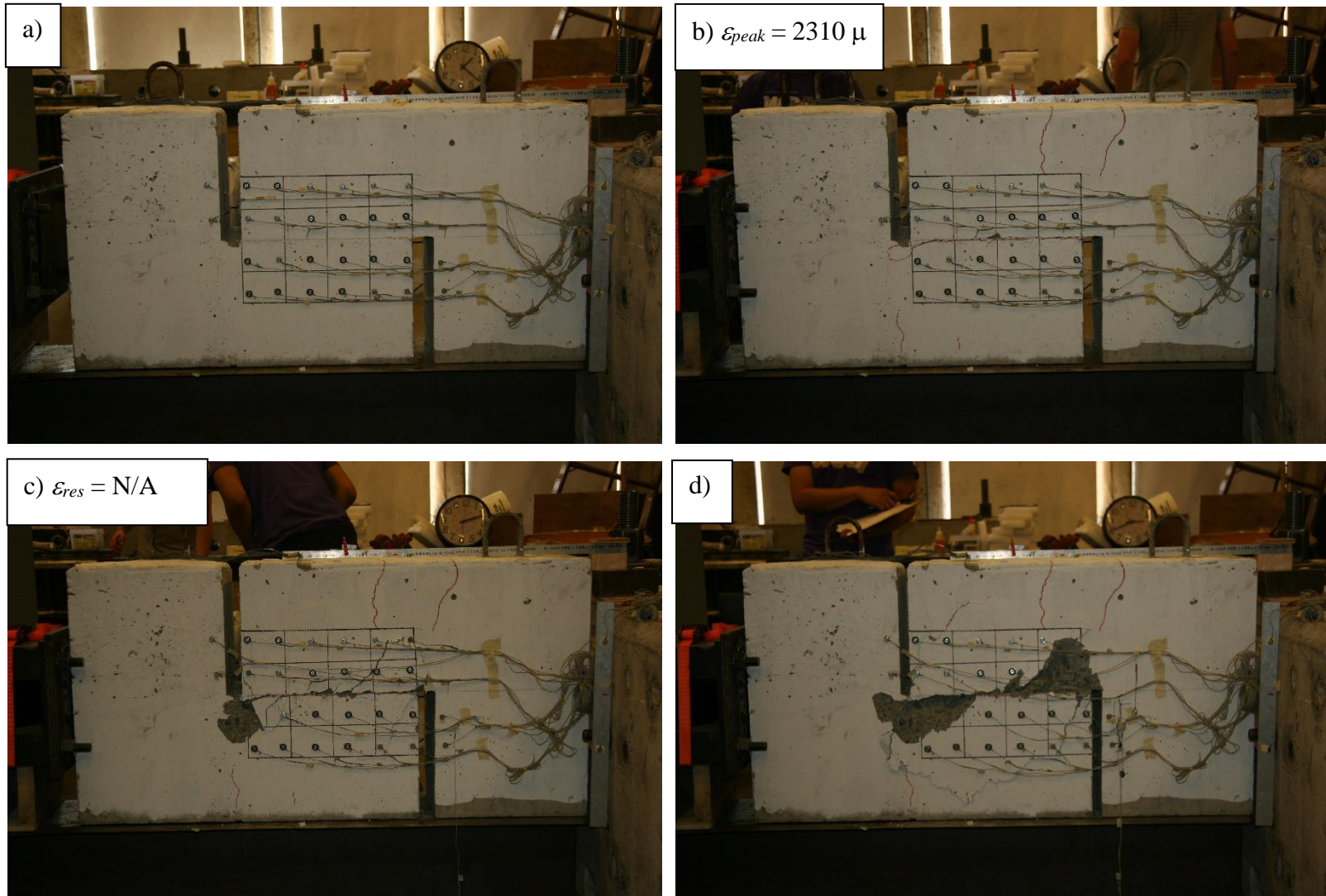


Figure 4.34: Photographs of UW80S-4 at different stages of the tests: a) start of test b) peak c) residual d) end of test. The average strain-gauge value at peak and at residual are included in the photographs.



Figure 4.35: Close up of the revealed reinforcement after test (UW80S-4 East side).



Figure 4.36: Close up of the revealed reinforcement after test (UW80S-4 West side).

UW80S-6 had six No. 5 80 ksi reinforcing bars crossing a smooth interface. The peak load was 109.7 kips, occurring at a slip displacement of 0.040 inch and an interface crack width of 0.016 inch. The applied load stabilized at a residual load of 93.4 kips, and the load was maintained until the end of test. This specimen in particular had minimal visible damage throughout the test. The extent of the damage is shown in Figure 4.38 and in Figure 4.39.

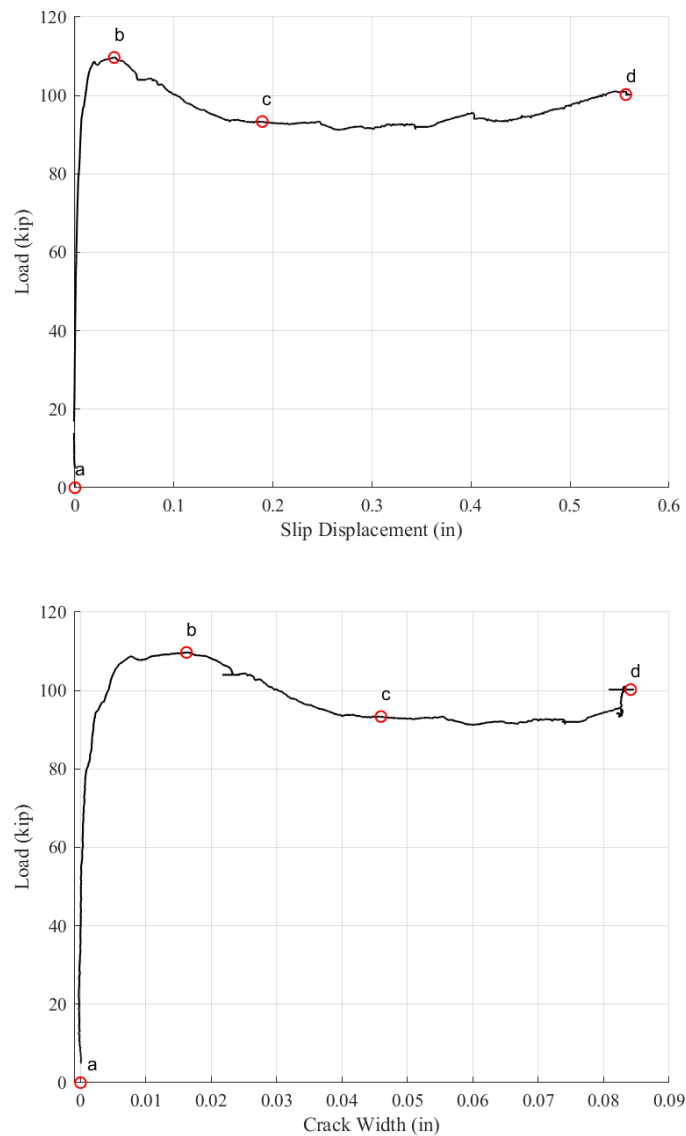


Figure 4.37: UW80S-6 load-slip displacement (top) and load-crack width graph (bottom). The letters in the graphs reference different stages and photographs in Figure 4.38.

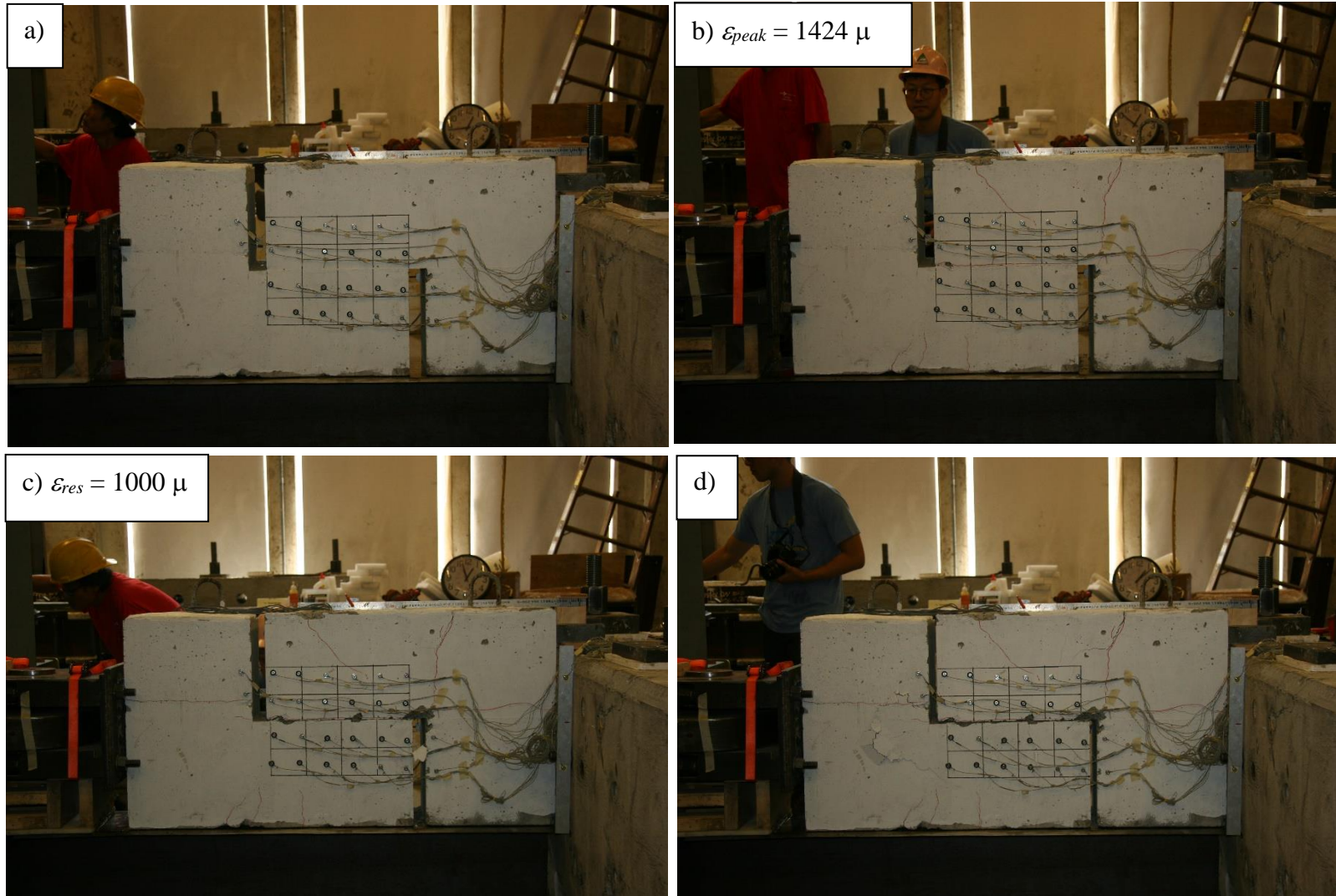


Figure 4.38: Photographs of UW80S-6 at different stages of the tests: a) start of test b) peak c) residual d) end of test. The average strain-gauge value at peak and at residual are included in the photographs.



Figure 4.39: Close up of the revealed reinforcement after test (UW80S-6 West side).

UW80S-8 had eight No. 5 80 ksi reinforcing bars crossing a smooth interface. The peak load was 135.6 kips, occurring at a slip displacement of 0.042 inch and an interface crack width of 0.013 inch. The applied load briefly plateaued at an 116.2 kips, then it gradually increased until the end of test as shown in Figure 4.40. It is unknown why this behavior occurred. A large block of concrete spalled towards the end of test while the applied load was still increasing, which was unusual. The damages are shown in Figure 4.42.

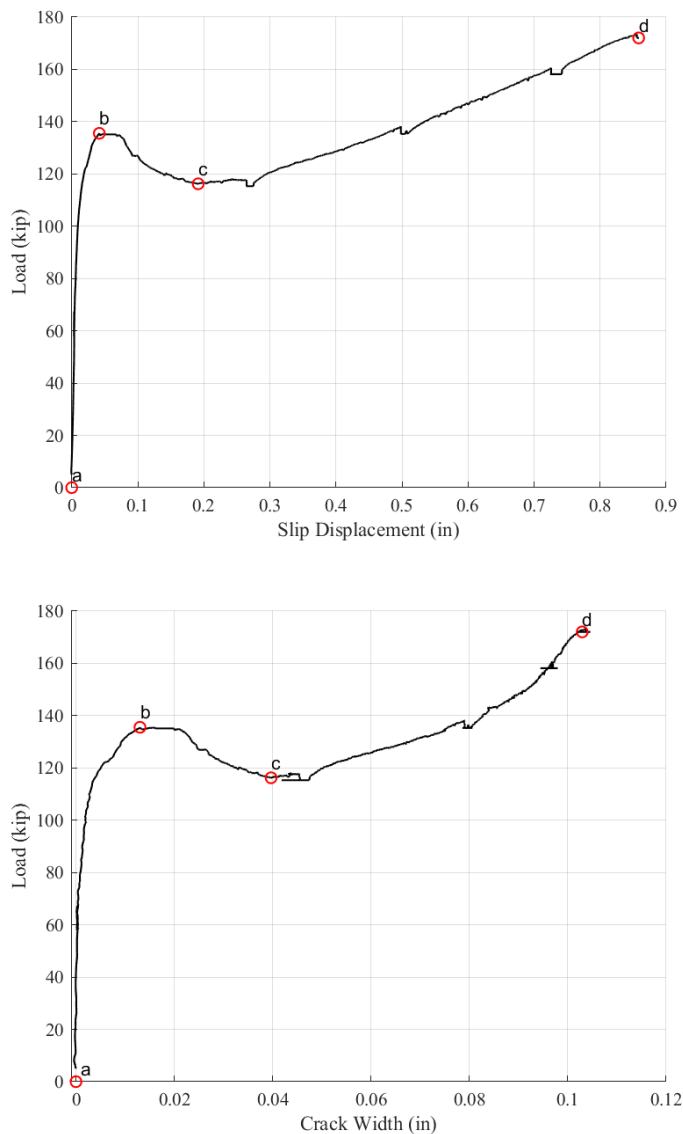


Figure 4.40 UW80S-8 load-slip displacement (top) and load-crack width graph (bottom). The letters in the graphs reference different stages and photographs in Figure 4.41.

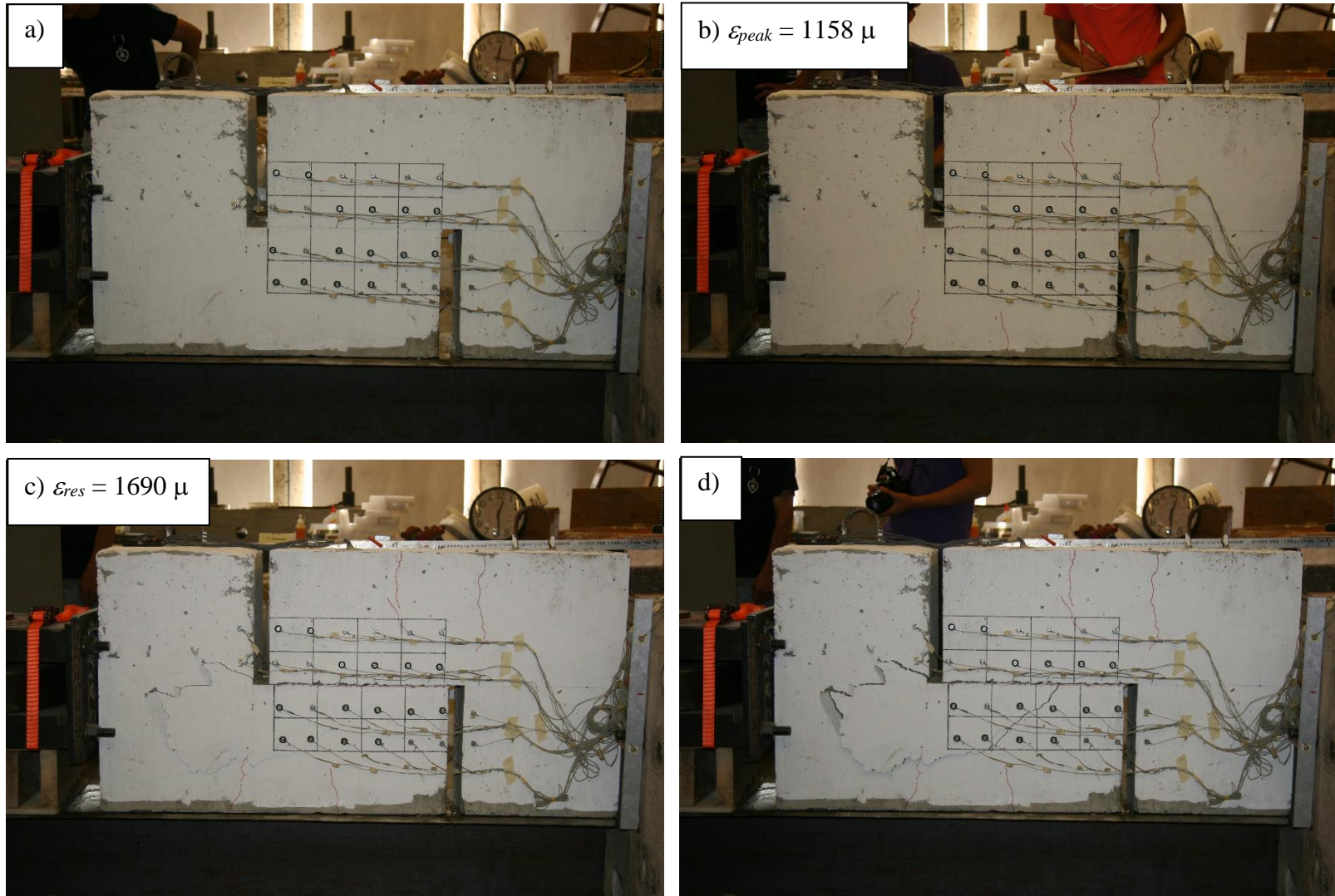


Figure 4.41: Photographs of UW80S-8 at different stages of the tests: a) start of test b) peak c) residual d) end of test. The average strain-gauge value at peak and at residual are included in the photographs.



Figure 4.42: Close up of the revealed reinforcement after test (UW80S-8 East side).



Figure 4.43: Photograph of the revealed reinforcement after test (UW80S-8 West side).

UW80S-10 had 10 No. 5 80 ksi reinforcing bars crossing a smooth interface. The peak load was 158.8 kips, occurring at a slip displacement of 0.027 inch and an interface crack width of 0.013 inch. The drop in applied load after peak was very gradual as shown in Figure 4.44. The applied load stabilized at a residual load of 143.6 kips. This load was maintained initially, but it increased slightly towards the end of the test. The reinforcement did not deform as much as reinforcement in other specimens, exhibiting a more rigid body rotation. The reinforcement after the test is shown in Figure 4.46.

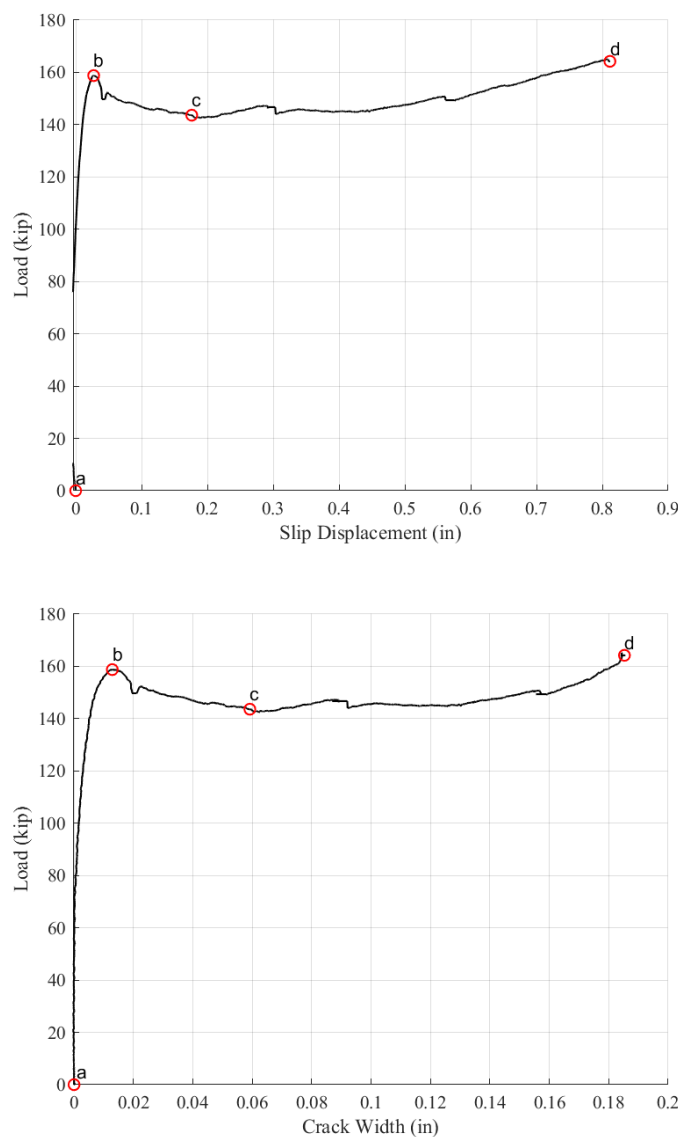


Figure 4.44: UW80S-10 load-slip displacement (top) and load-crack width graph (bottom). The letters in the graphs reference different stages and photographs in Figure 4.45.

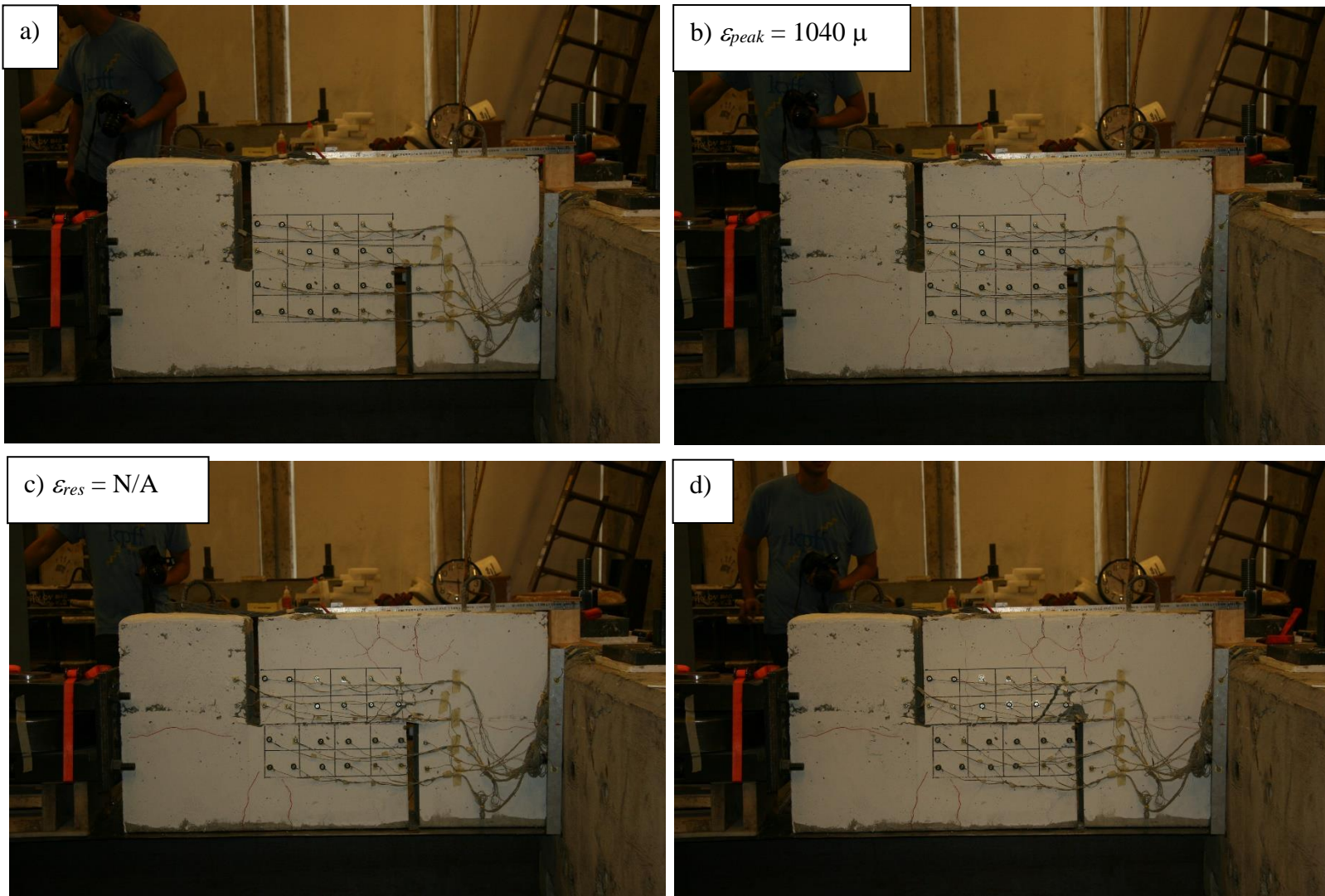


Figure 4.45: Photographs of UW80S-10 at different stages of the tests: a) start of test b) peak c) residual d) end of test. The average strain-gauge value at peak and at residual are included in the photographs.

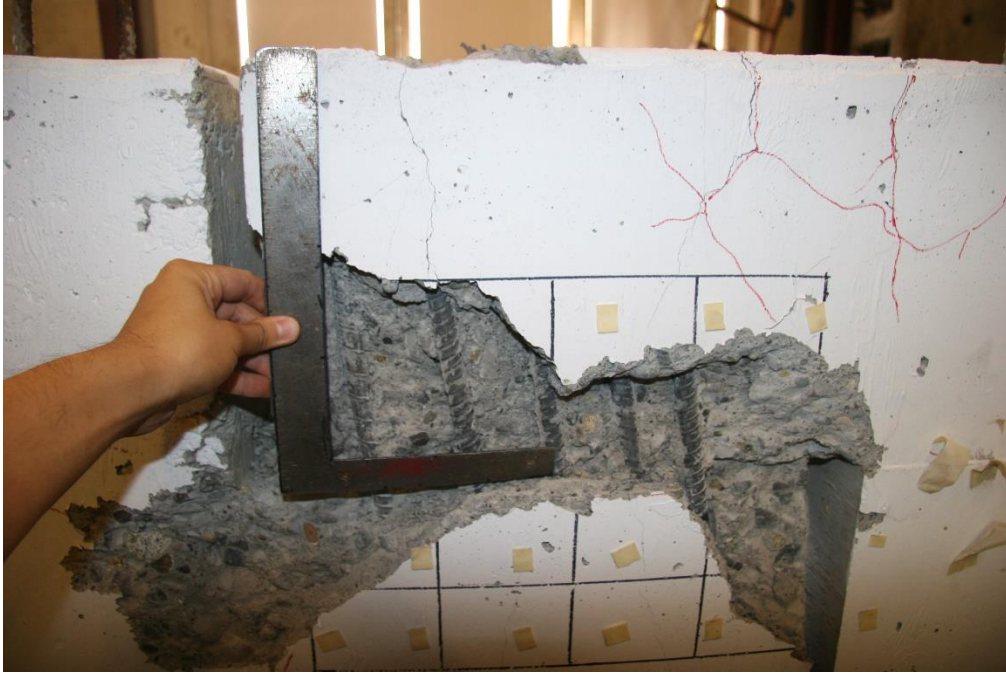


Figure 4.46: Photograph of the revealed reinforcement after test (UW80S-10 East side).

UW80S-12 had 12 No. 5 80 ksi reinforcing bars crossing a smooth interface. The peak load was 195.0 kips, occurring at a slip displacement of 0.040 inch and an interface crack width of 0.008 inch. This specimen displayed the typical specimen behavior prior to the peak, but it displayed a unique post-peak behavior. The applied load continued to decline rather than stabilizing at a specific residual load value (shown in Figure 4.47). The specimen started to lift off the support beam towards the end of the test (stage c marked in the Load-Slip Displacement graph shown in Figure 4.47). The uplift might explain why the crack width decreased at the residual stage. This behavior was not seen in other specimens. It was unclear why this behavior only occurred for UW80S-12, but it was most likely a test setup issue. Photographic evidence is provided and the gap between the support beam and the specimen is circled in red; however, the uplift is difficult to see in the photographs (Figure 4.48).

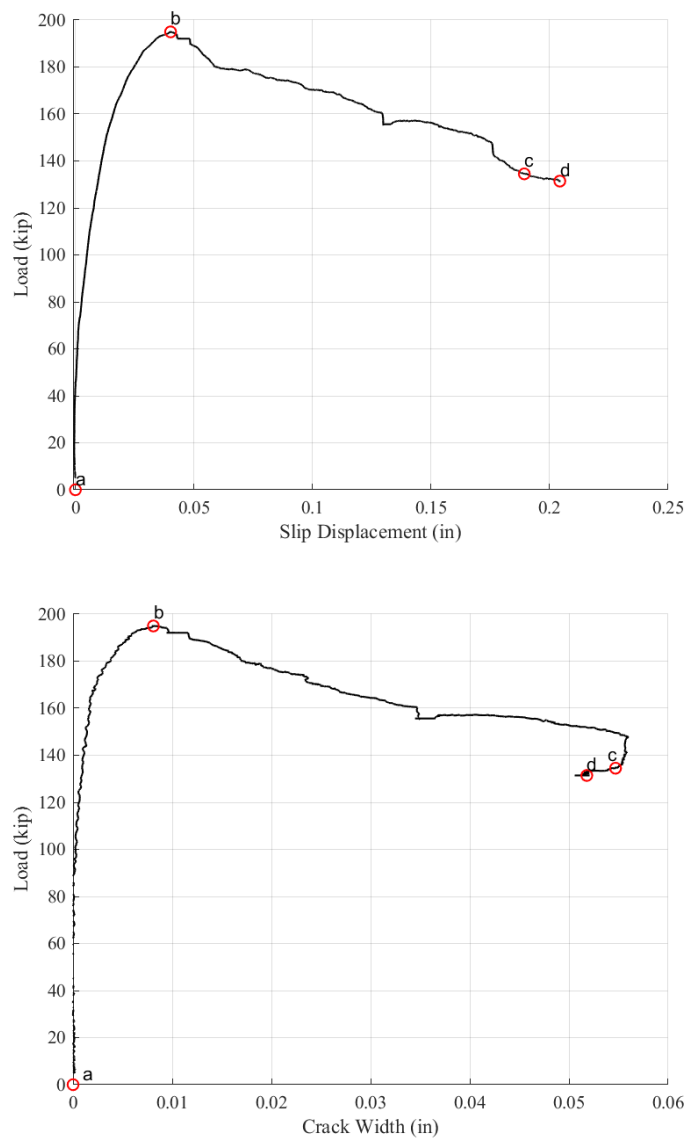


Figure 4.47: UW80S-12 Load-slip displacement (top) and load-crack width graph (bottom). The letters in the graphs reference different stages and photographs in Figure 4.48.

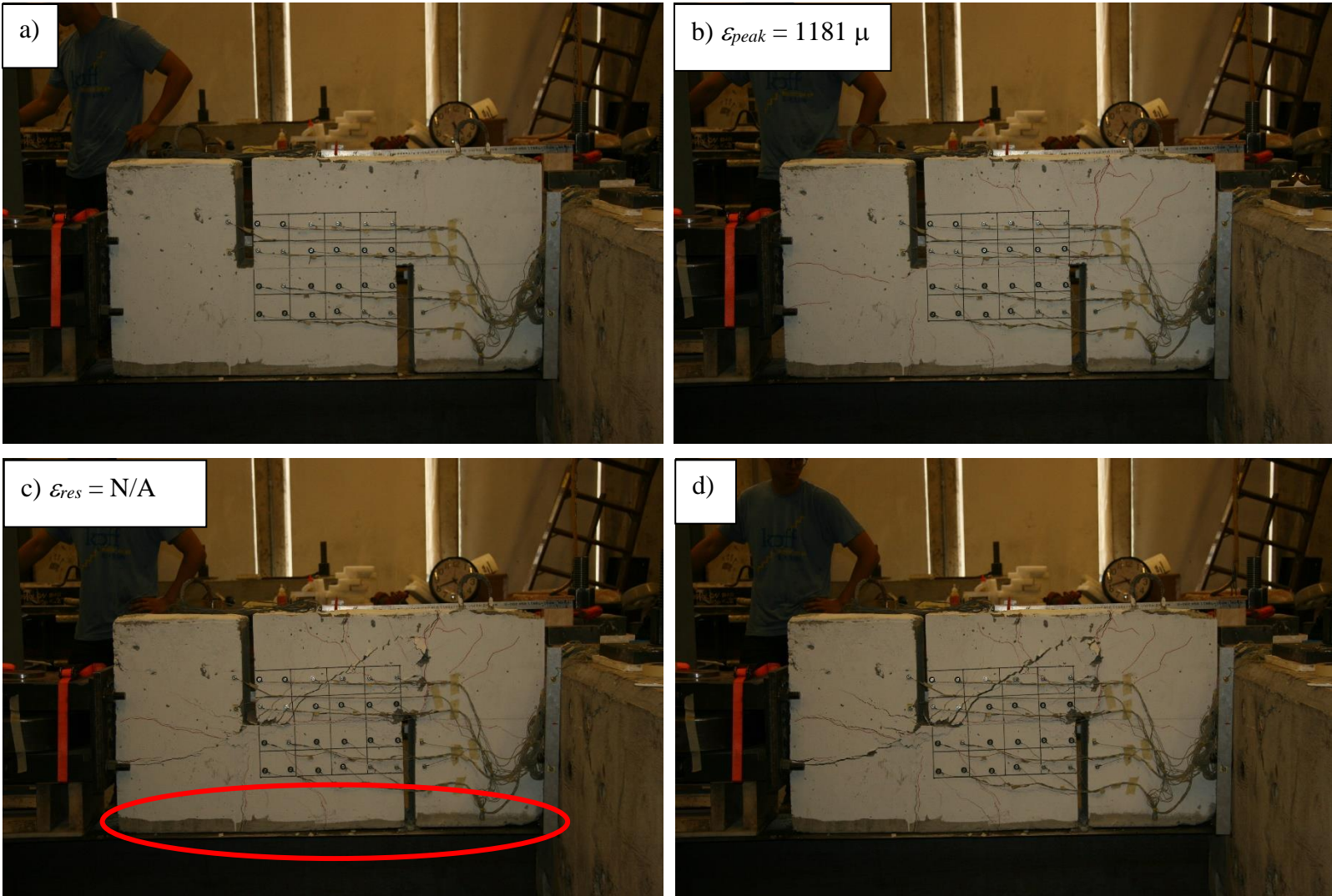


Figure 4.48: Photographs of UW80S-12 at different stages of the tests: a) start of test b) peak c) residual d) end of test. The average strain-gauge value at peak and at residual are included in the photographs.



Figure 4.49: Photograph of the revealed reinforcement after test (UW80S-12 East side).

4.3.4 Test Series 60R: Specimens with 60 ksi Reinforcement Crossing a Roughened Interface

This series consisted of five specimens with 4 to 12 74.4 ksi (specified 60 ksi) steel reinforcing bars crossing a roughened interface. The theoretical clamping stress ranged from 580 psi to 1,734 psi.

UW60R-4 had four No. 5 60 ksi reinforcing bars crossing a roughened interface. The peak load was 132.3 kips, occurring at a slip displacement of 0.0396 inch and an interface crack width of 0.0145 inch. The load gradually dropped to a residual load of 88.1 kips and continued to drop until the end of the test (shown in Figure 4.50). The specimen did not show any unusual visible damage or reinforcement deformation. The photographs below (Figure 4.51, Figure 4.52 and Figure 4.53) shows the qualitative sense of the slip displacement, visible damage and reinforcement deformation.

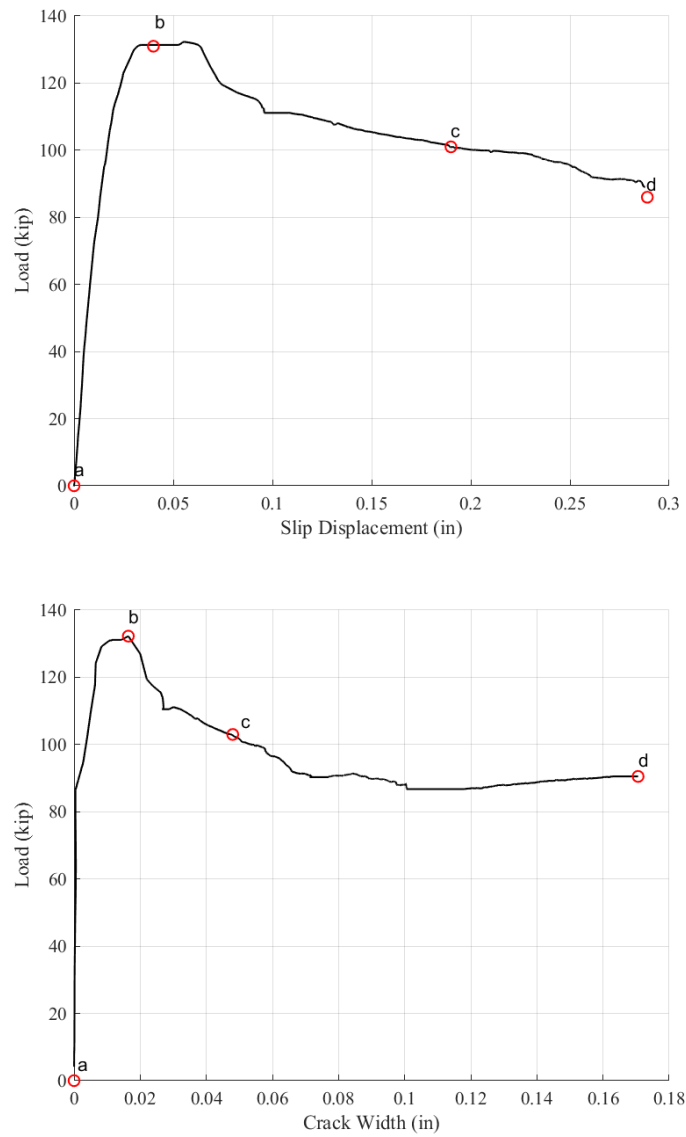


Figure 4.50: UW60R-4 Load-slip displacement (top) and load-crack width graph (bottom). The letters in the graphs reference different stages and photographs in Figure 4.51

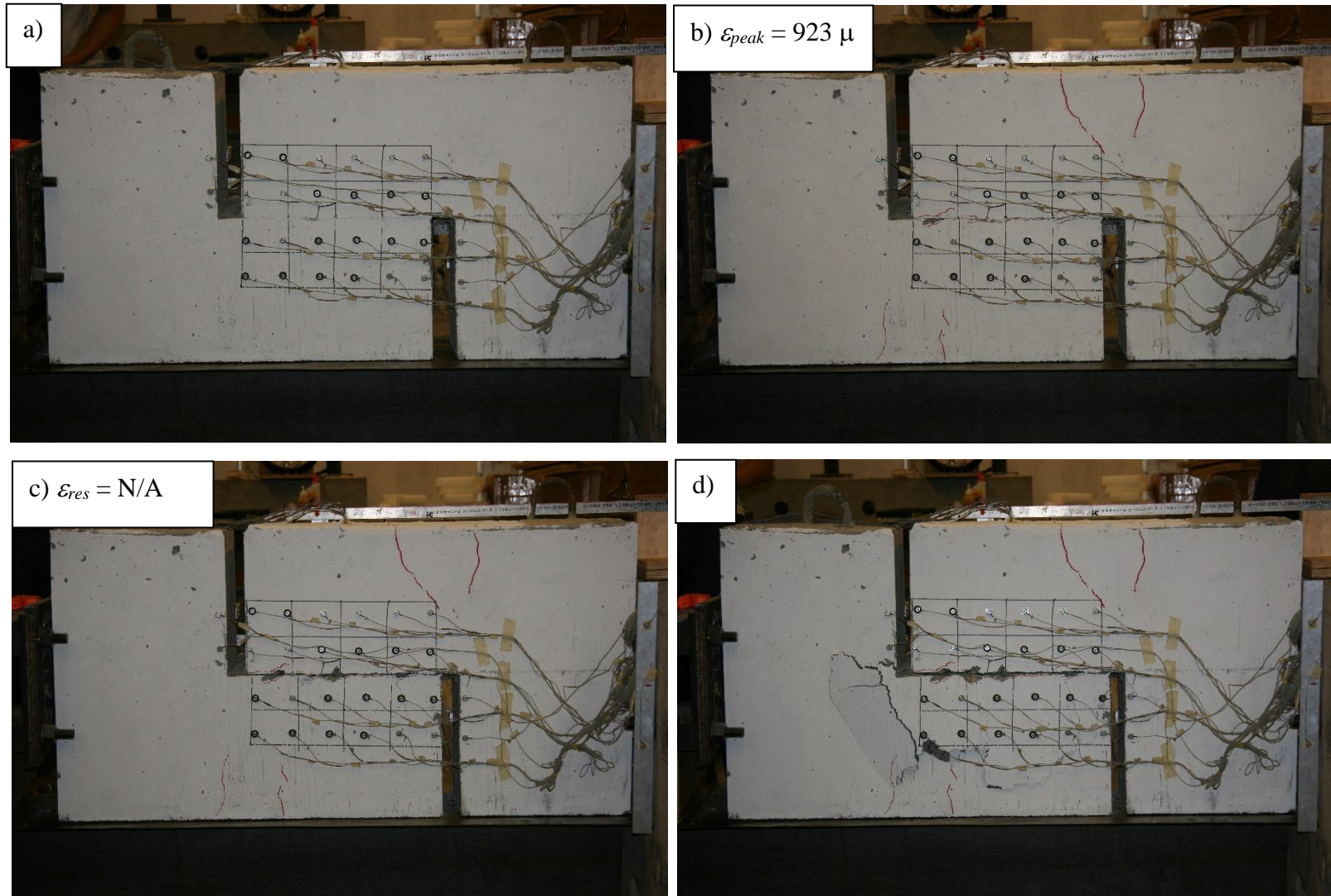


Figure 4.51: Photographs of UW60R-4 at different stages of the tests: a) start of test b) peak c) residual d) end of test. The average strain-gauge value at peak and at residual are included in the photographs.



Figure 4.52: Photograph of the revealed reinforcement after test (UW60R-4 East side).



Figure 4.53: Photograph of the revealed reinforcement after test (UW60R-4 West side).

UW60R-6 had six No. 5 60 ksi reinforcing bars crossing a roughened interface. The peak load was 126.4 kips, occurring at a slip displacement of 0.011 inch and an interface crack width of 0.004 inch. The residual load is reported as 101.9 kips, but the load continued to decline gradually to around 90 kips. The applied load stabilized briefly before the load started to rise near the end of the test (point d in Figure 4.54). The photographs below (Figure 4.55, Figure 4.56 and Figure 4.57) provide a qualitative sense of the specimen slip displacement, spalling, and reinforcement deformation.

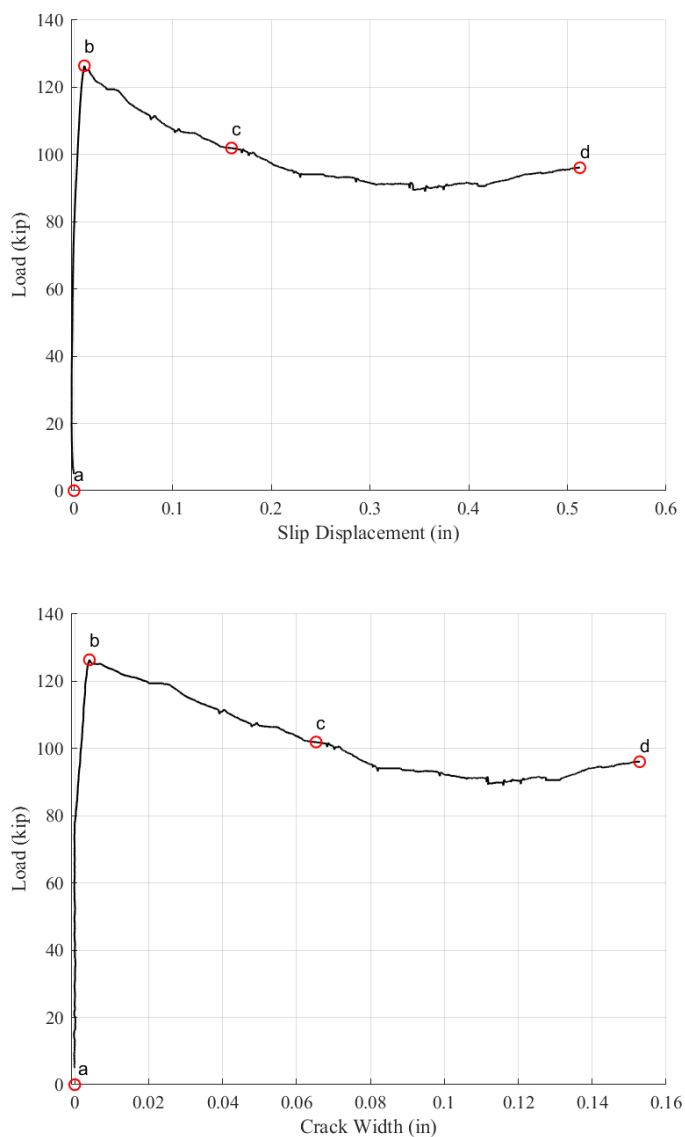


Figure 4.54: UW60R-6 Load-slip displacement (top) and load-crack width graph (bottom). The letters in the graphs reference different stages and photographs in Figure 4.55.

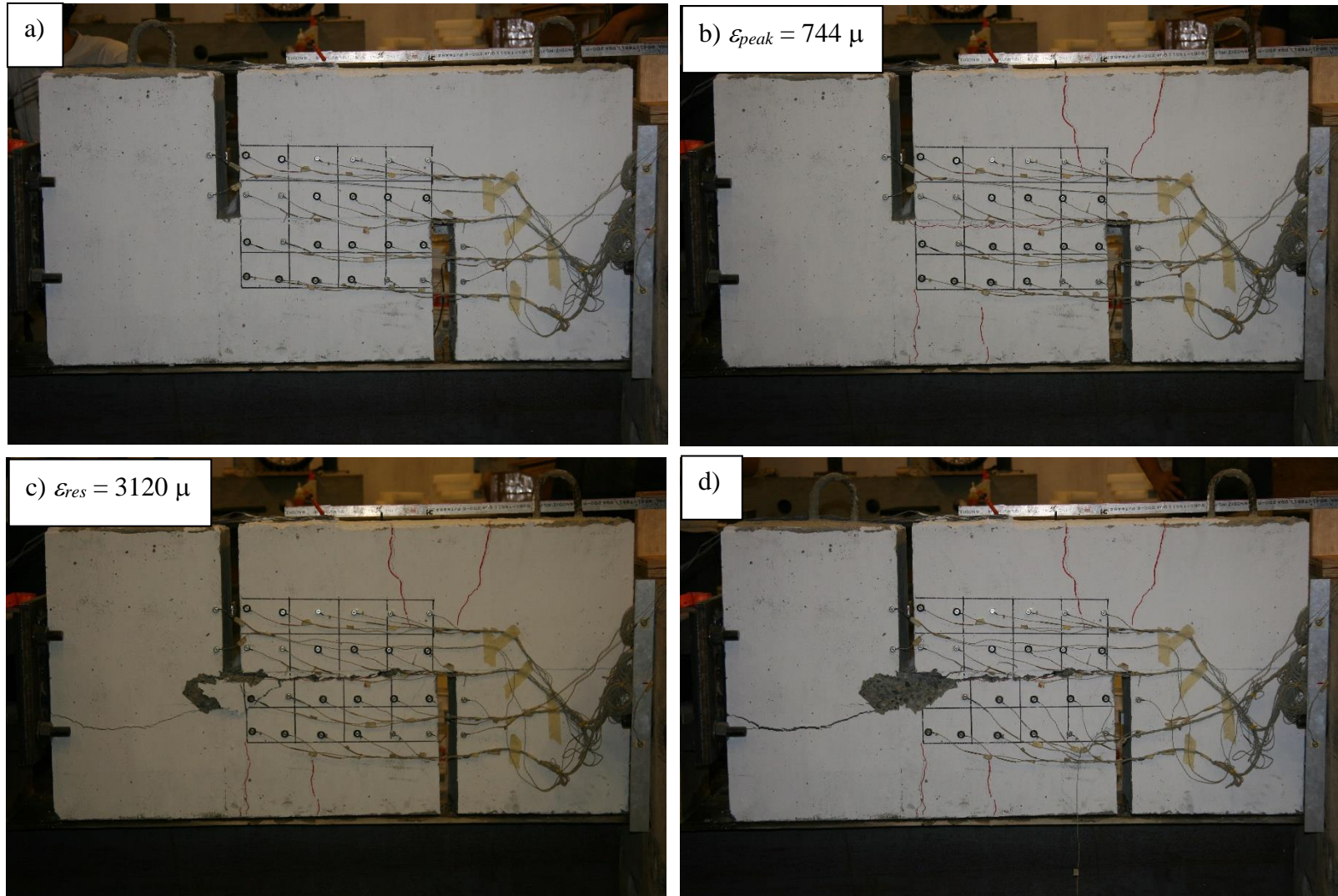


Figure 4.55: Photographs of UW60R-6 at different stages of the tests: a) start of test b) peak c) residual d) end of test. The average strain-gauge value at peak and at residual are included in the photographs.



Figure 4.56: Close up of the revealed reinforcement after test (UW60R-6 West side).

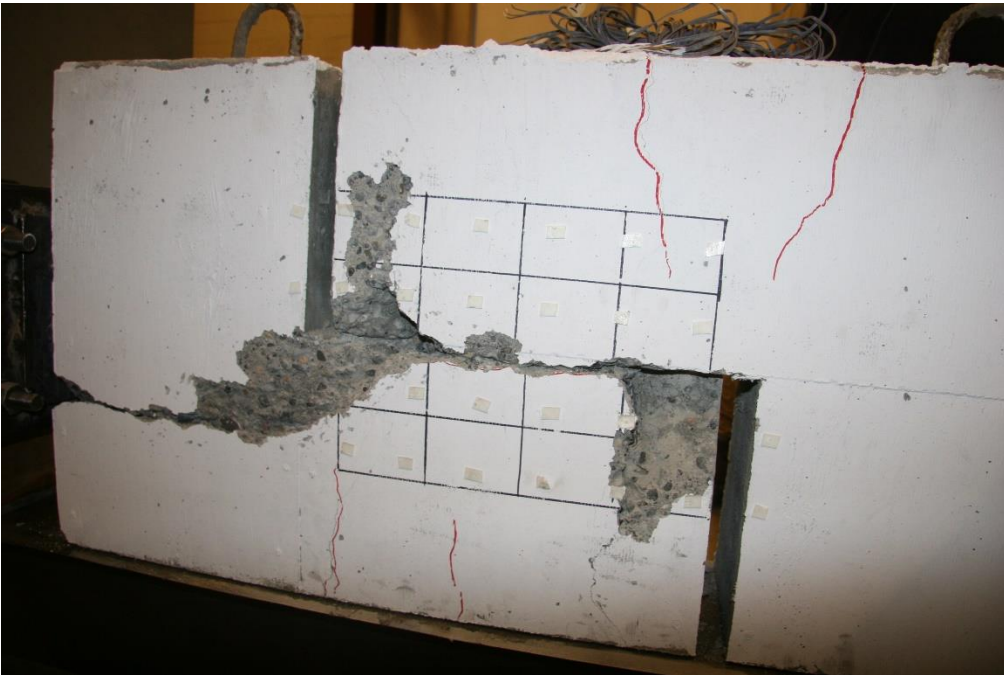


Figure 4.57: Photograph of the visible damage after test (UW60R-6 East side).

UW60R-8 had eight No. 5 60 ksi reinforcing bars crossing a roughened interface. The peak load was 167.8 kips, occurring at a slip displacement of 0.021 inch and an interface crack width of 0.009 inch. Post-peak, the applied load stabilized at a residual load of 121.4 kips and was maintained until the end of the test. Crack patterns and concrete spalling were consistent with those observed and discussed for previous specimens. Visible damage and the deformation of the reinforcements can be seen in Figure 4.59 and Figure 4.60.

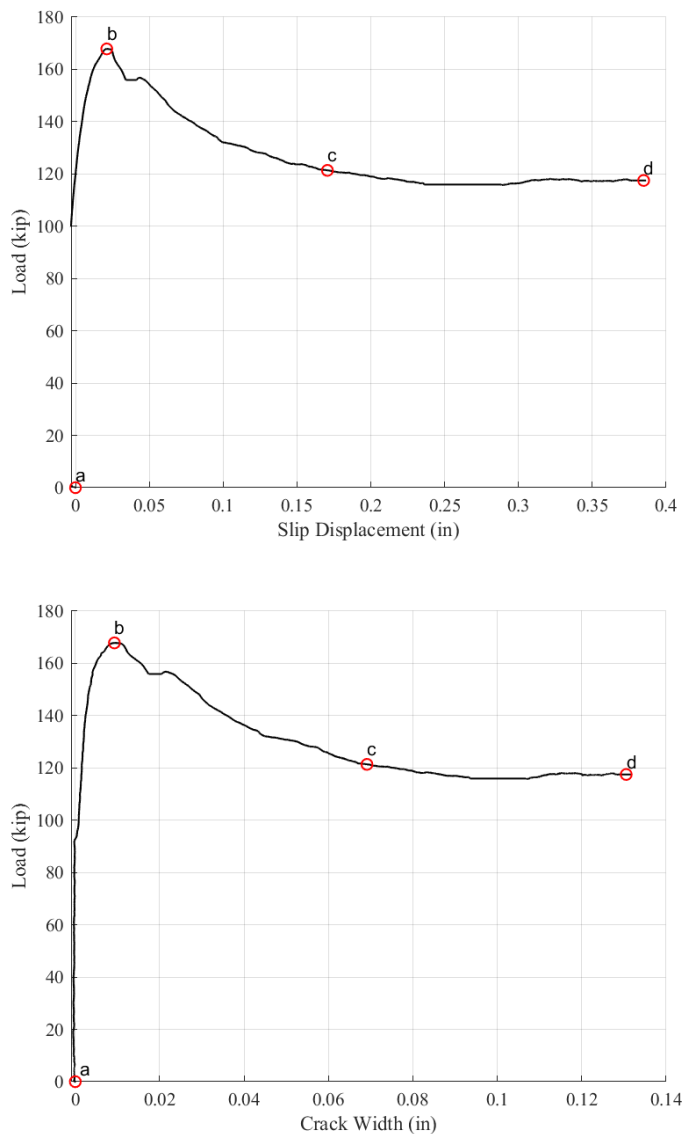


Figure 4.58: UW60R-8 Load-slip displacement (top) and load-crack width graph (bottom). The letters in the graphs reference different stages and photographs in Figure 4.59.

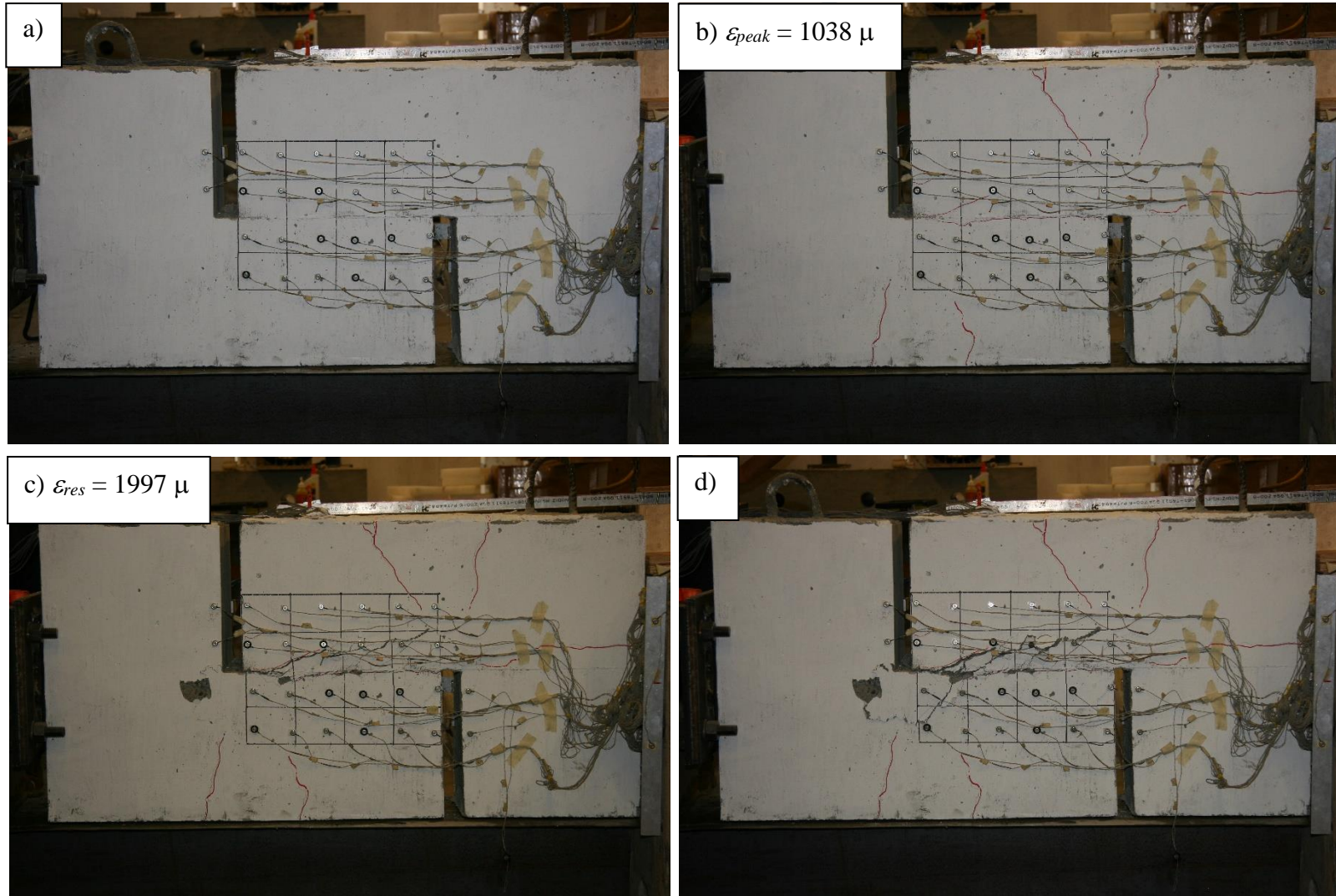


Figure 4.59: Photographs of UW60R-8 at different stages of the tests: a) start of test b) peak c) residual d) end of test. The average strain-gauge value at peak and at residual are included in the photographs.



Figure 4.60: Close up of the revealed reinforcement after test (UW60R-8 East side).

UW60R-10 had 10 No. 5 60 ksi reinforcing bars crossing a roughened interface, and the specimen displayed a typical pre-peak and peak response. The peak load was 169.6 kips, occurring at a slip displacement of 0.022 inch and an interface crack width of 0.0055 inch. Post-peak, the applied load stabilized at a residual load of 137.5 kips that was maintained until the end of test. Visible damages and reinforcement deformations were typical as shown in Figure 4.62 and in Figure 4.63.

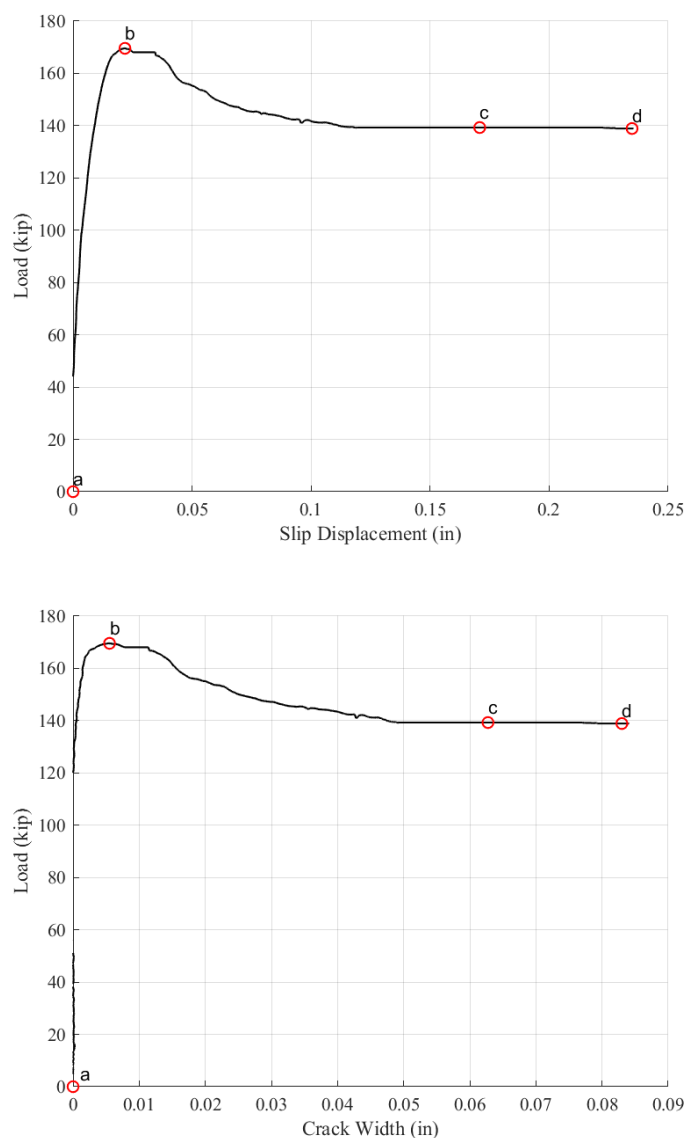


Figure 4.61: UW60R-10 Load-slip displacement (top) and load-crack width graph (bottom). The letters in the graphs reference different stages and photographs in Figure 4.62.

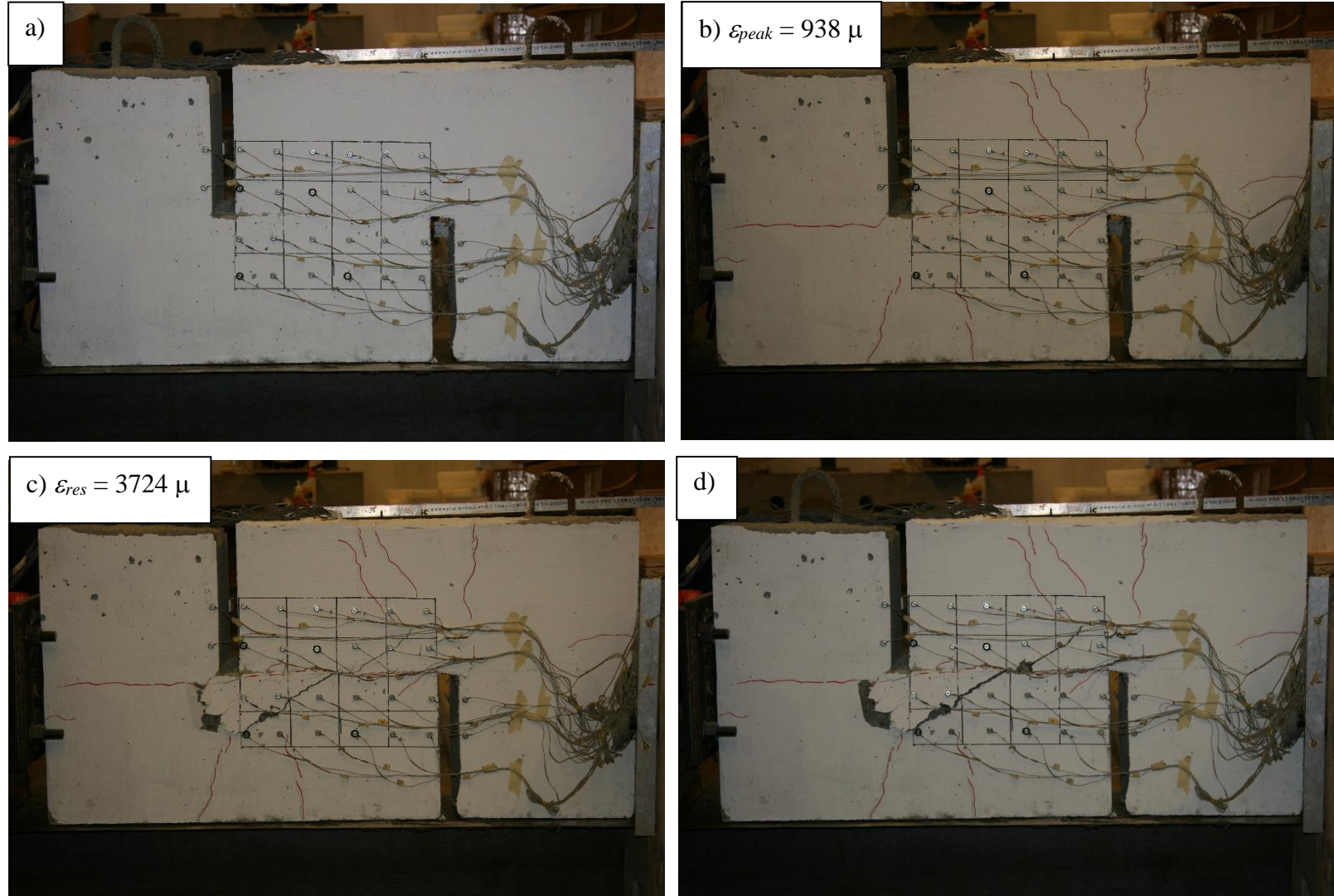


Figure 4.62: Photographs of UW60R-10 at different stages of the tests: a) start of test b) peak c) residual d) end of test. The average strain-gauge value at peak and at residual are included in the photographs.



Figure 4.63: Close up of the revealed reinforcement after test (UW60R-10 East side).

UW60R-12 had 12 No. 5 60 ksi reinforcing bars crossing a roughened interface. The peak load was 173.9 kips, occurring at a slip displacement of 0.022 inch and an interface crack width of 0.006 inch. Post-peak, the applied load stabilized at a residual load of 131.5 kips and was maintained until the end of test (point c in Figure 4.64). The post-peak behavior was analogous to that of most specimens and there was little visible damage outside of the critical interface region (Figure 4.65 and Figure 4.66).

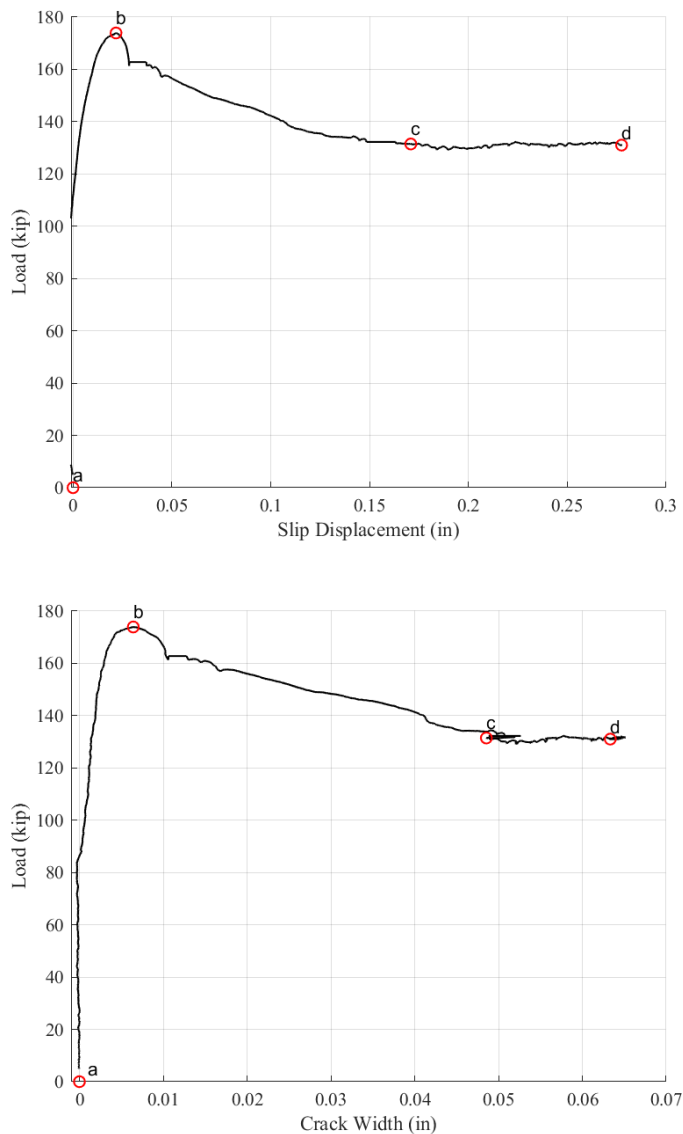
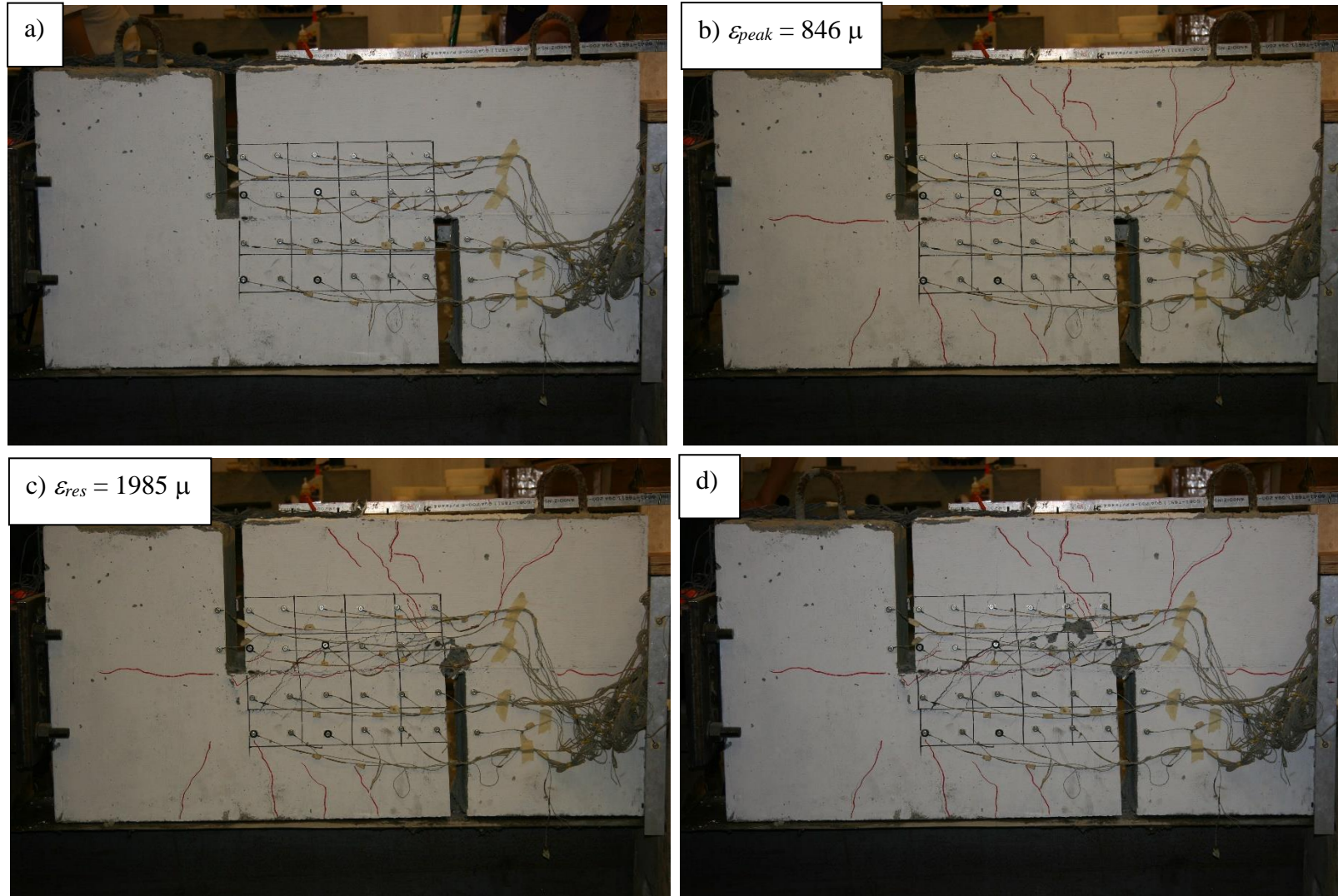


Figure 4.64 UW60R-12 Load-slip displacement (top) and load-crack width graph (bottom). The letters in the graphs reference different stages and photographs in Figure 4.65.



**Figure 4.65: Photographs of UW60R-12 at different stages of the tests: a) start of test
 b) peak c) residual d) end of test. The average strain-gauge value at peak and at residual are included in the photographs.**

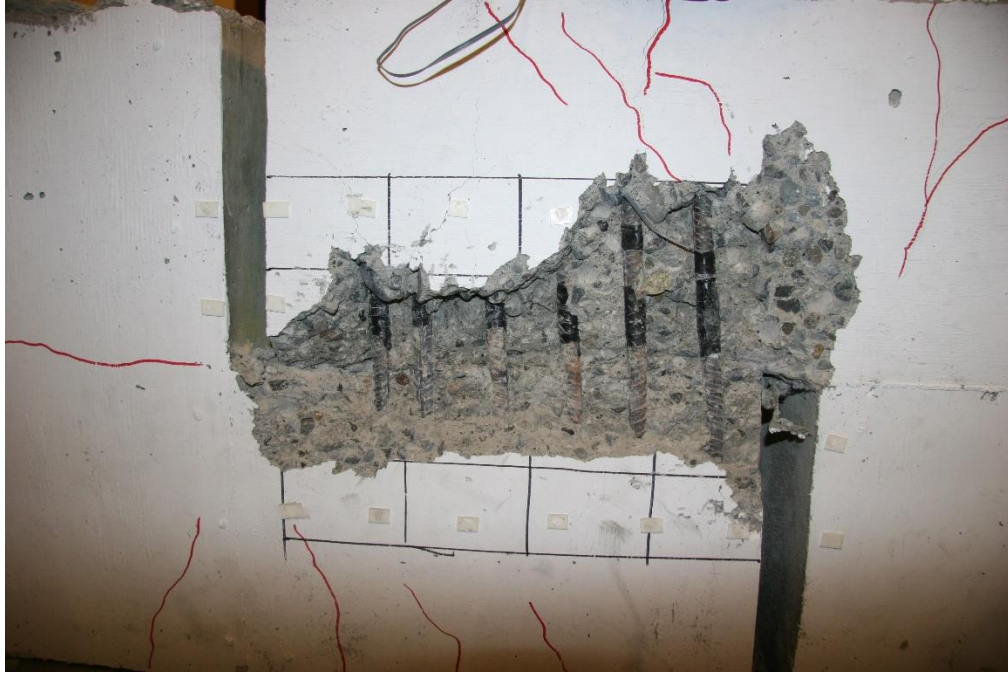


Figure 4.66 Photograph of the revealed reinforcement after test (UW60R-12 East side).

4.3.5 Test Series 80R: Specimens with 80 ksi Reinforcement Crossing a Roughened Interface

This series consisted of five specimens with 4 to 12 98.1 ksi (specified 80 ksi) steel reinforcing bars crossing a roughened interface. The theoretical clamping stress ranged from 765 psi to 2,286 psi

UW80R-4 had four No. 5 80 ksi reinforcing bars crossing a roughened interface. There was a sudden shift in the interface width at around 80 kips (Figure 4.67), suggesting that a primary crack formed at the interface before the peak load. The peak shear load was 131.0 kips, occurring at a slip displacement of 0.015 inch and an interface crack width of 0.012 inch. Post-peak, the applied load continued to gradually decline until the end of test shown in Figure 4.67. The residual load was 104.0 kips. The photographs below (Figure 4.68 and Figure 4.69) provide a qualitative sense of the specimen slip displacement, spalling, and reinforcement rotation.

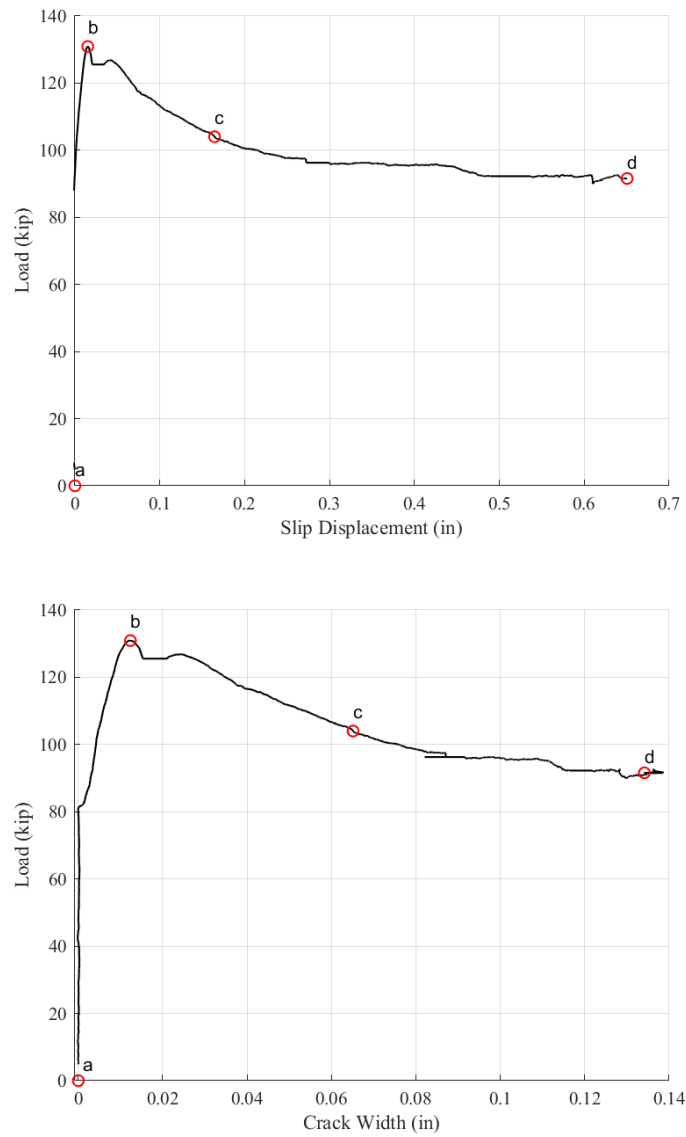


Figure 4.67: UW80R-4 Load-slip displacement (top) and load-crack width graph (bottom). The letters in the graphs reference different stages and photographs in Figure 4.68.

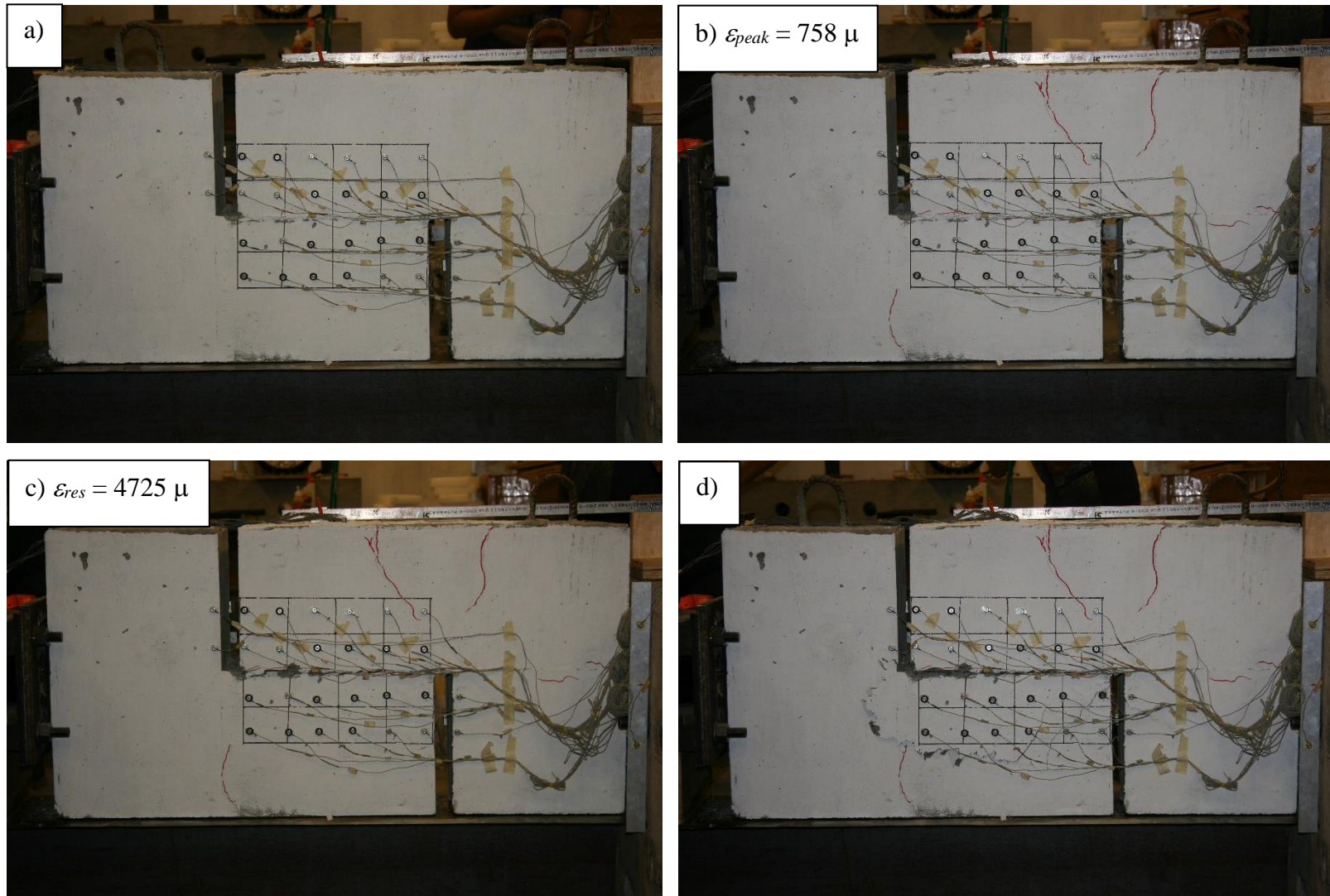


Figure 4.68: Photographs of UW80R-4 at different stages of the tests: a) start of test b) peak c) residual d) end of test. The average strain-gauge value at peak and at residual are included in the photographs.



Figure 4.69: Photograph of the revealed reinforcement after test (UW80R-4 East side).

UW80R-6 had six No. 5 80 ksi reinforcing bars crossing a roughened interface. The peak shear load was 119.0 kips, occurring at a slip displacement of 0.005 inch and an interface crack width of 0.002 inch. Post-peak, the applied load stabilized at a residual load of 98.1 kips and was maintained until the end of test as shown in the region between b and d in Figure 4.70. Overall, the specimen displayed the same qualitative response outlined for most specimens. Visible damages and reinforcement deformations were typical as shown in Figure 4.71 and in Figure 4.72.

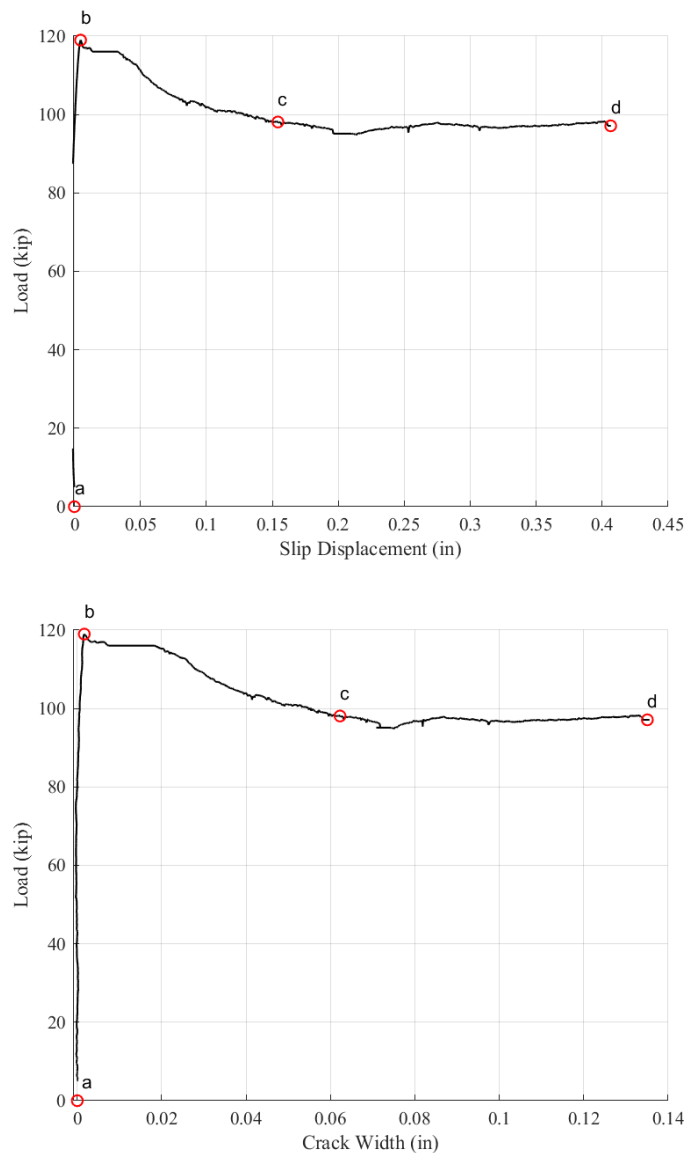


Figure 4.70: UW80R-6 Load-slip displacement (top) and load-crack width graph (bottom). The letters in the graphs reference different stages and photographs in Figure 4.71.

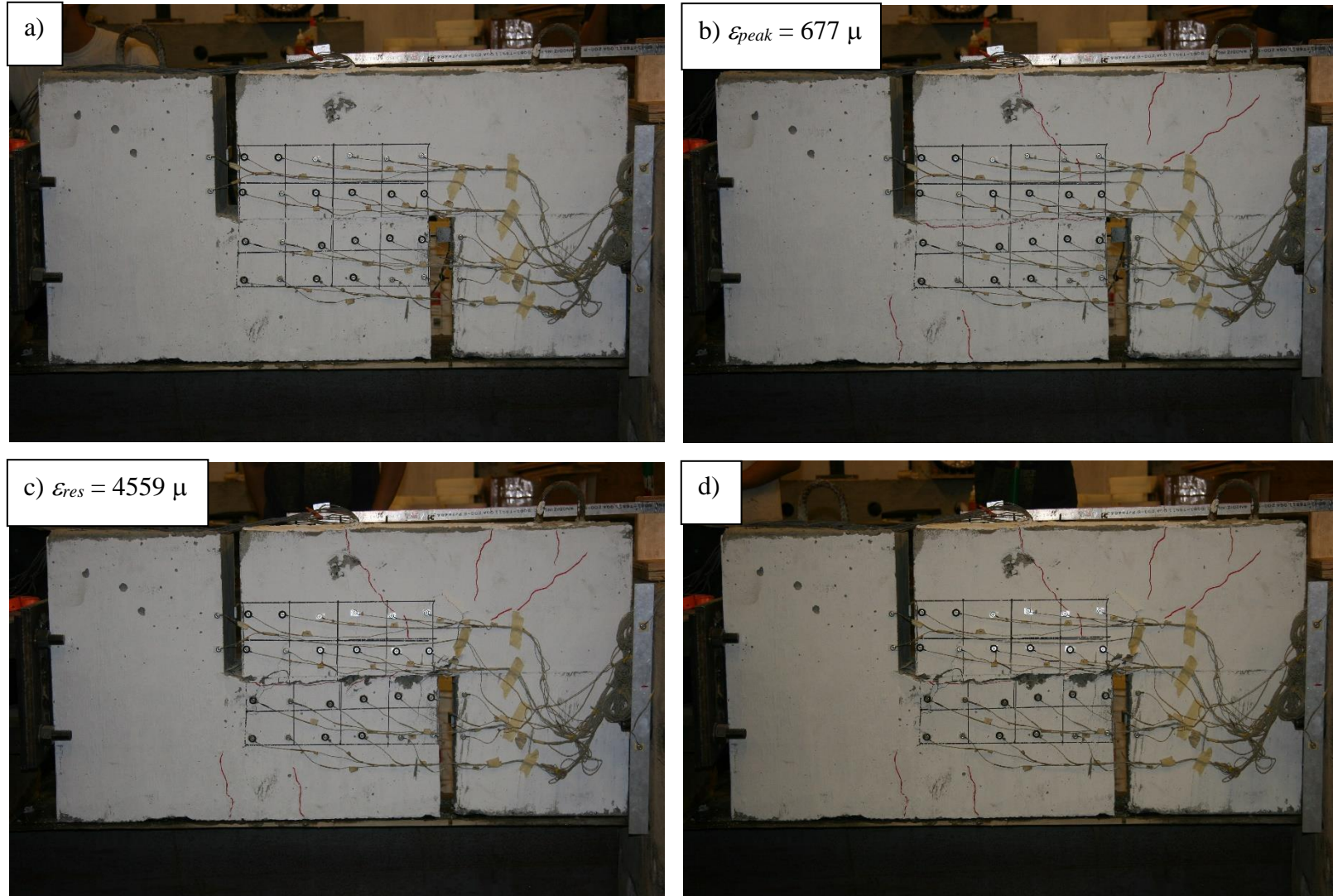


Figure 4.71: Photographs of UW80R-6 at different stages of the tests: a) start of test b) peak c) residual d) end of test. The average strain-gauge value at peak and at residual are included in the photographs.

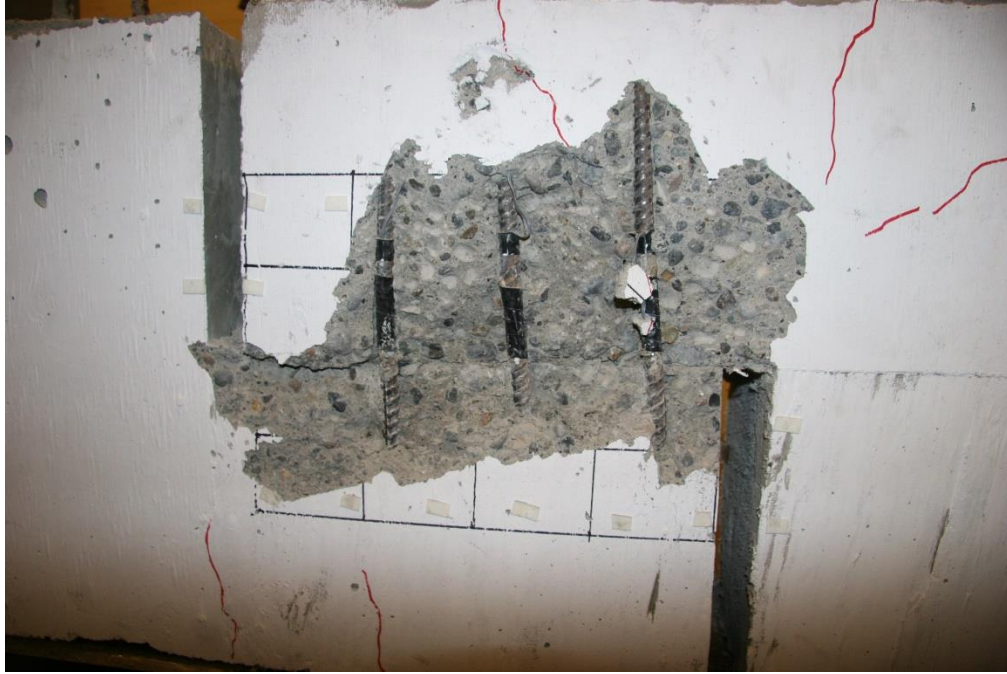


Figure 4.72: Photograph of the revealed reinforcement after test (UW80R-6 East side).

UW80R-8 had eight No. 5 80 ksi reinforcing bars crossing a roughened interface. The peak load was 174.7 kips, occurring at a slip displacement of 0.039 inch and an interface crack width of 0.022 inch. The residual load was 140.7 kips, and the applied load continued to drop until the end of test. Overall, the specimen exhibited typical post-peak response, without notable visible damage. However, a closer inspection performed after the test revealed the presence of some loose concrete in the vicinity of the gap was detected and removed. The extent of the damages is shown in Figure 4.75.

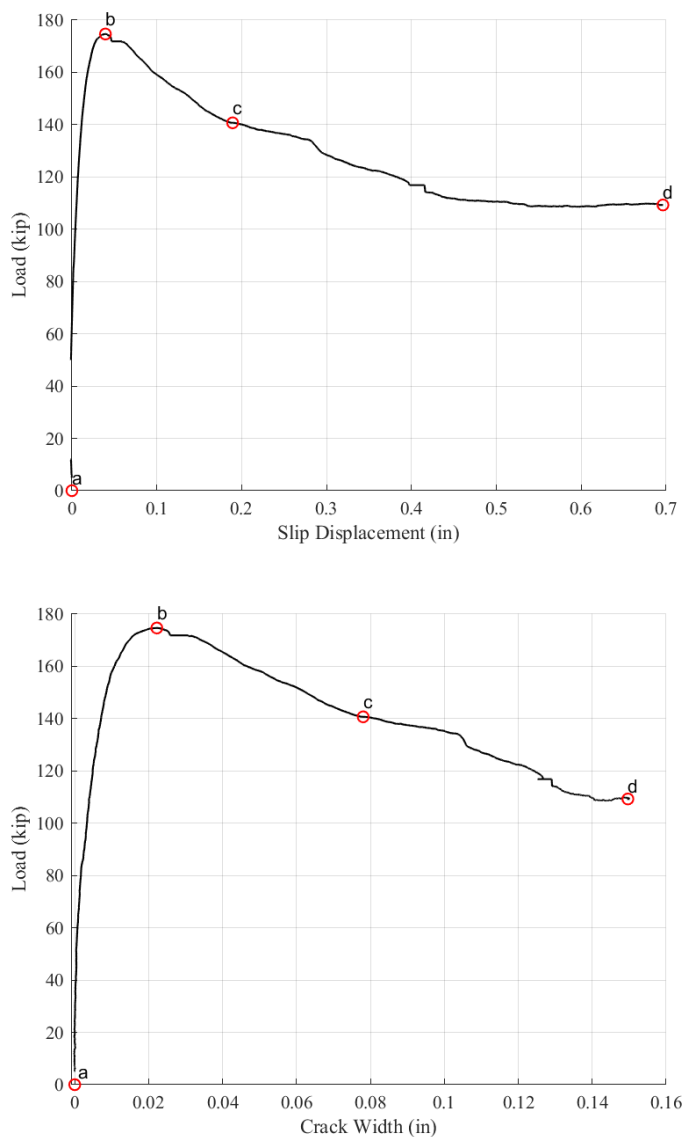


Figure 4.73: UW80R-8 Load-slip displacement (top) and load-crack width graph (bottom). The letters in the graphs reference different stages and photographs in Figure 4.74.

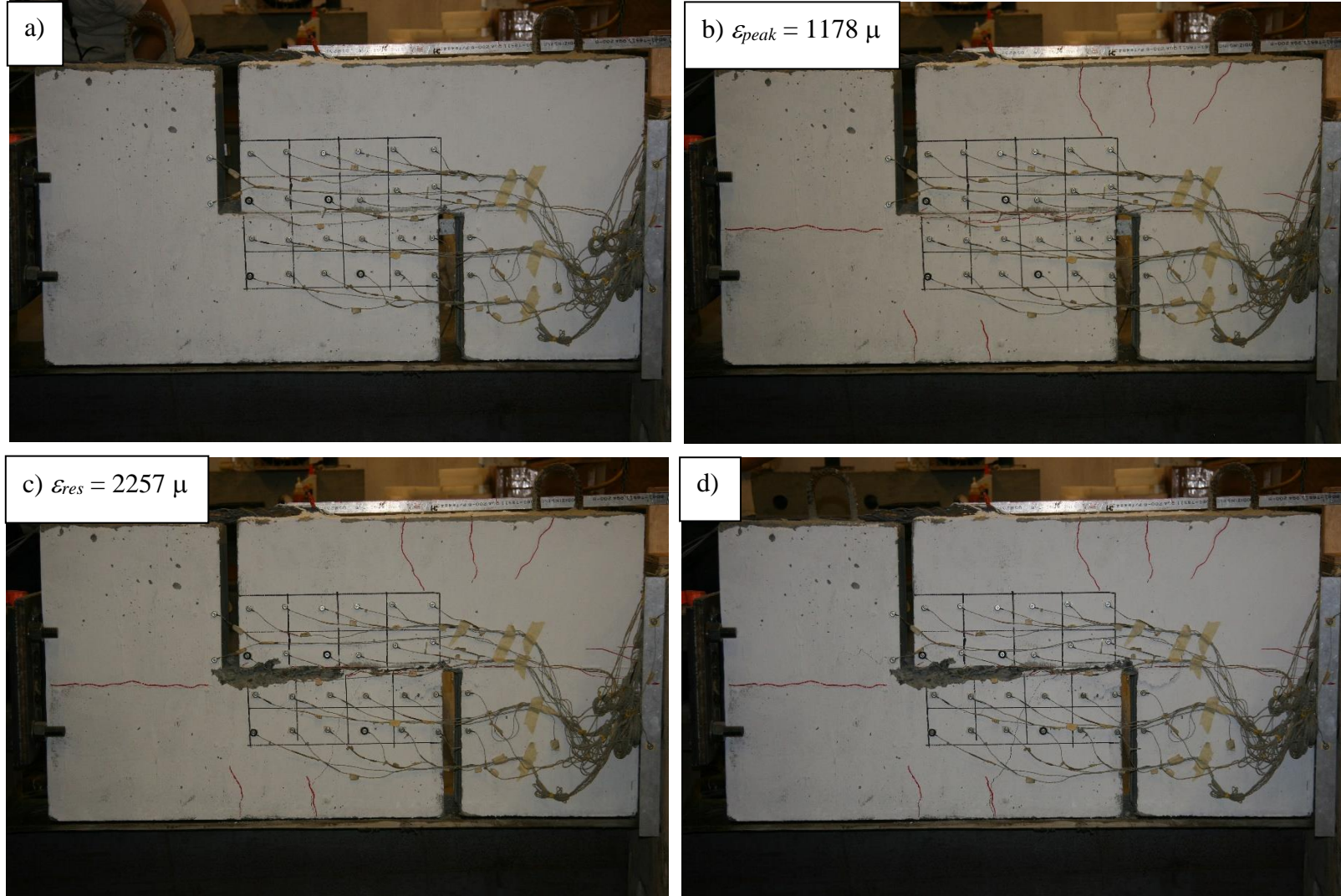


Figure 4.74: Photographs of UW80R-8 at different stages of the tests: a) start of test b) peak c) residual d) end of test. The average strain-gauge value at peak and at residual are included in the photographs.



Figure 4.75: Close up of the revealed reinforcement after test (UW80R-8 East side).

UW80R-10 had 10 No. 5 80 ksi reinforcing bars crossing a roughened interface. The specimen's peak shear load was 178.9 kips, occurring at a slip displacement of 0.023 inch and an interface crack width of 0.010 inch. The residual load was 133.4 kips, but the applied load continued to gradually decline until the end of the test as shown in Figure 4.76. The photographs below (Figure 4.77 and Figure 4.78) provide a qualitative sense of the specimen slip displacement, spalling, and reinforcement deformation.

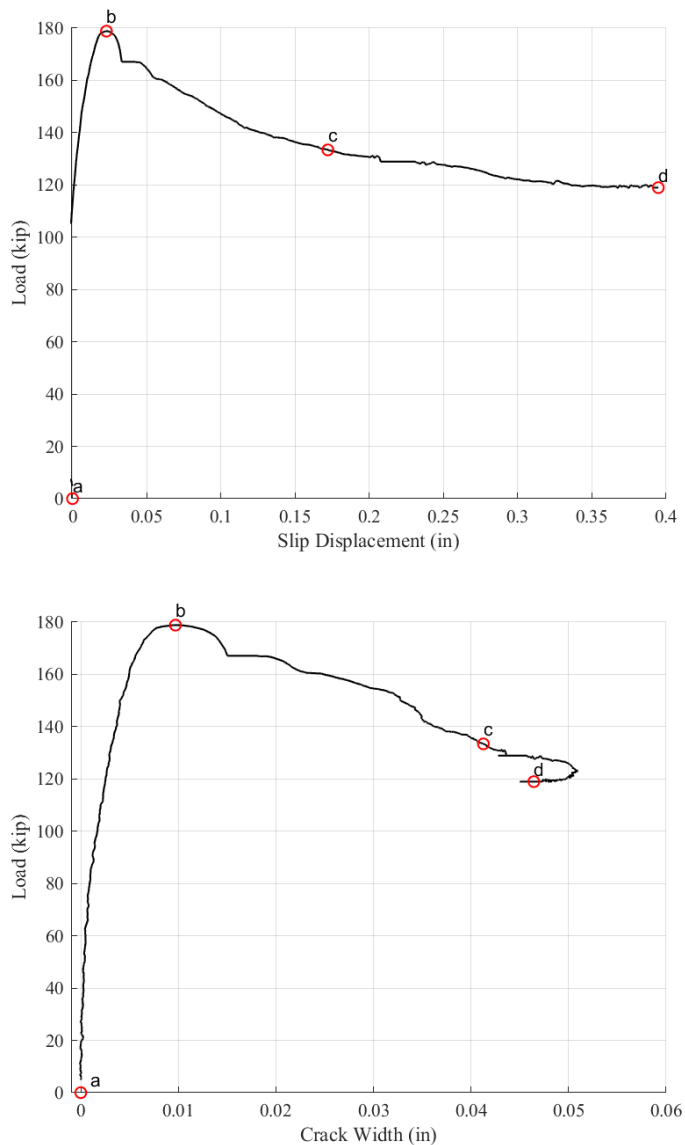


Figure 4.76: UW80R-10 Load-slip displacement (top) and load-crack width graph (bottom). The letters in the graphs reference different stages and photographs in Figure 4.77.

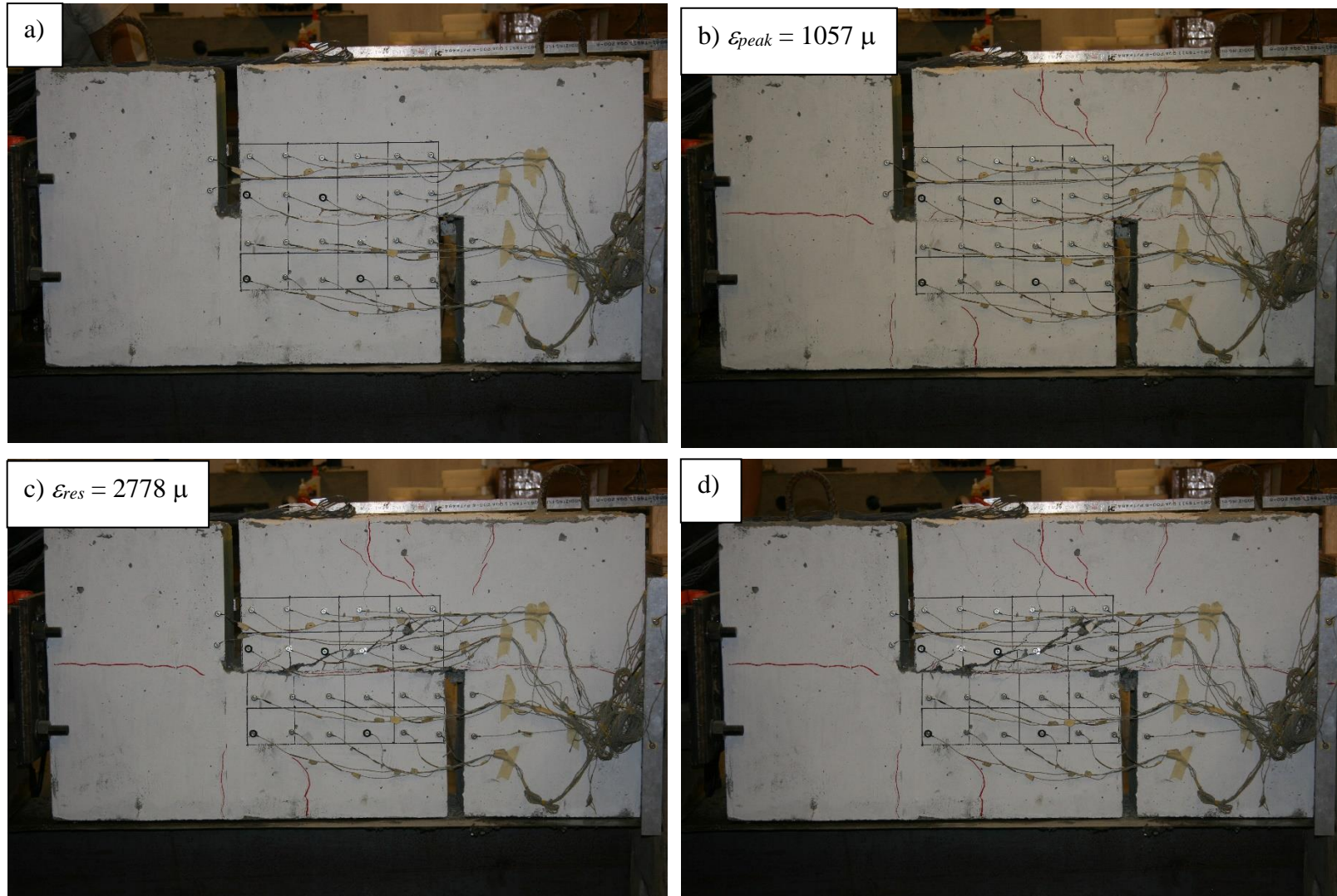


Figure 4.77: Photographs of UW80R-10 at different stages of the tests: a) start of test b) peak c) residual d) end of test. The average strain-gauge value at peak and at residual are included in the photographs.



Figure 4.78: Close up of the revealed reinforcement after test (UW80R-10 East side).

UW80R-12 had 12 No. 5 80 ksi reinforcing bars crossing a roughened interface. Its pre-peak and peak behaviors were typical except that there were more secondary vertical cracks: this is shown in Figure 4.80-b. The peak shear load was 153.9 kips, occurring at a slip displacement of 0.014 inch and an interface crack width of 0.004 inch. Load stabilized at a residual load of 109.8 kips and was maintained until the end of test shown in Figure 4.79. The photographs below (Figure 4.80 and Figure 4.81) provide a qualitative sense of the specimen slip displacement, spalling, and reinforcement deformation.

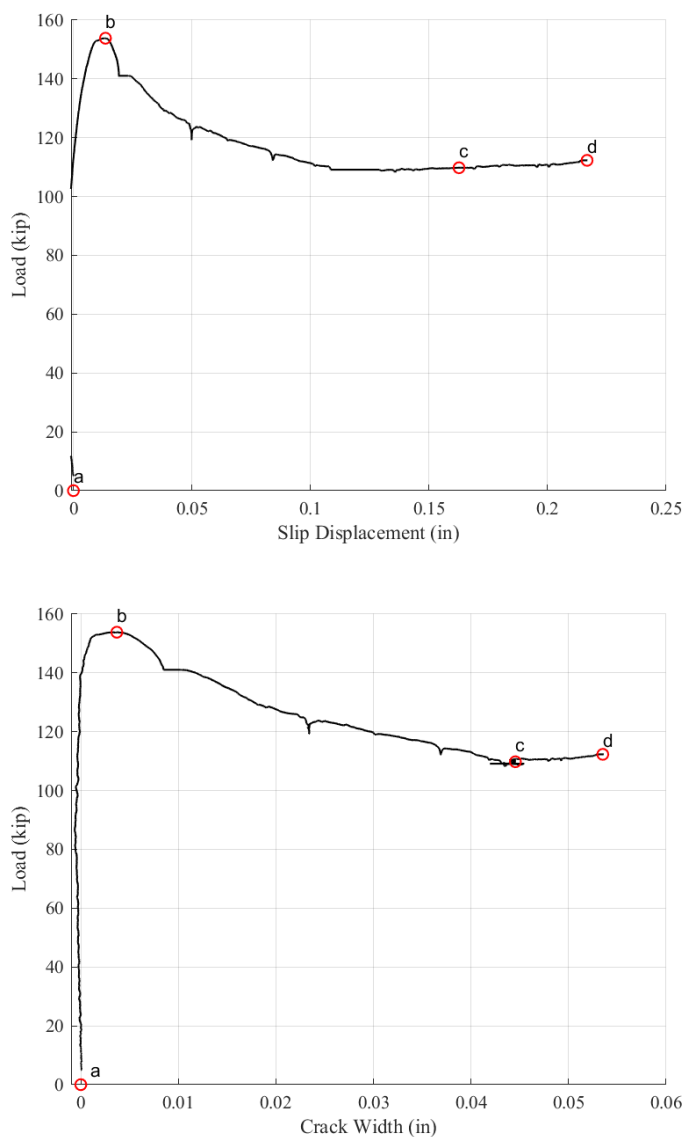


Figure 4.79: UW80R-12 Load-slip displacement (top) and load-crack width graph (bottom). The letters in the graphs reference different stages and photographs in Figure 4.80.

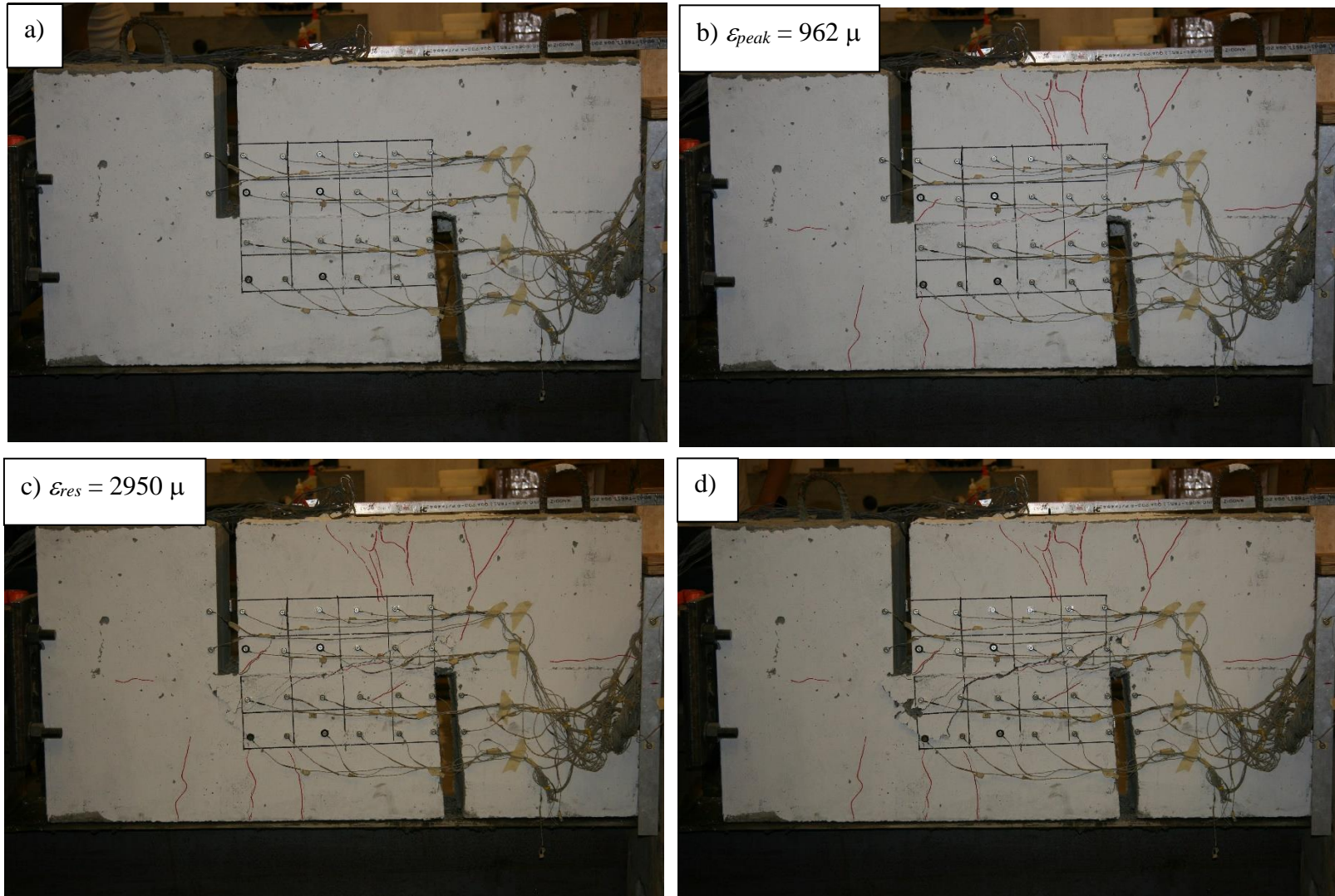


Figure 4.80: Photographs of UW80R-12 at different stages of the tests: a) start of test b) peak c) residual d) end of test. The average strain-gauge value at peak and at residual are included in the photographs.



Figure 4.81: Close up of the revealed reinforcement after test (UW80R-12 East side).

4.4 Summary of the Experimental Results

As mentioned before, most specimens showed similar behavior throughout the test. Aside from few specimens, no visible crack formed along the interface before reaching peak load. Post-peak, the applied load gradually decreased until it reached the residual load. Every specimen except for UW60S-2, UW80S-2, UW0S, and UW0R maintained a considerable residual load ranging from 86 kips to 144 kips. In most cases, roughened specimens had higher peak shear load, lower slip displacement and crack width at peak load. The quantitative effects of the roughness and theoretical clamping stress are discussed further in the following chapter. How the experimental results lead to the design of a more accurate shear friction model is discussed in Chapter 6.

Chapter 5: Data Analysis

The experimental results and the behavior of specimens discussed in the previous chapter are analyzed in this chapter. This chapter focuses on how different interface roughness and steel reinforcement parameters influence the overall shear-transfer capacity. More specifically, the three main parameters analyzed are surface condition, reinforcement ratio, and yield strength. Because these parameters are closely related to each other, the results are analyzed by isolating the effects of each variables. The main experimental used for the analysis include peak shear load, slip displacement at peak load, crack width at peak load, residual load, and the axial strain of the reinforcing bars. The impact of the surface conditions had on the shear-transfer capacity was more apparent, so its effects were analyzed and discussed first. After establishing the overall trends, the effects of the reinforcement ratio and yield strength are analyzed by separating the specimens in two groups, namely smooth and roughened specimens. Note that historically, these specimens are prone to natural scatter. Specimens with identical parameters often result in different behaviors and shear-transfer capacities. Any findings and conclusions discussed in this chapter are based on 24 unique specimens from the experimental program.

5.1 The Influence of Roughness

The impact of the interface roughness on the shear strength of the specimens can be seen in Figure 5.1, which provides a comparison between the results of the smooth specimens and the results of their roughened counterparts. As explained in Chapter 4, there were 10 pairs of specimens (each made of one smooth and one roughened specimen) with same reinforcement ratio and yield strength. In the sections that follow, the effect of interface roughness on the shear-transfer capacity of the specimens is presented first, with focus on peak and residual loads. This discussion is followed by the analysis of the slip displacement and crack width at peak load.

5.1.1 Peak Shear-Transfer Capacity

In general, smooth specimens reached a lower peak shear load than their roughened counterparts. For example, UW60S-8 reached a peak shear load of 157.6 kips, while UW60R-8 reached a peak shear load of 167.7 kips (6.4% increase in capacity). UW80S-10 reached a peak shear load of 158.8 kips, while UW80R-10 reached a peak shear load of 178.9 kips (12.7% increase in capacity).

The only smooth specimen that outperformed its roughened counterpart was UW80S-12, which appeared to be an anomaly. It was clear that the roughness level achieved from the application of the surface retarders discussed in Chapter 3, was sufficient to provide consistent increase in the peak shear-transfer capacity. Figure 5.1 presents the experimental peak shear loads as a function of the nominal clamping stress values:

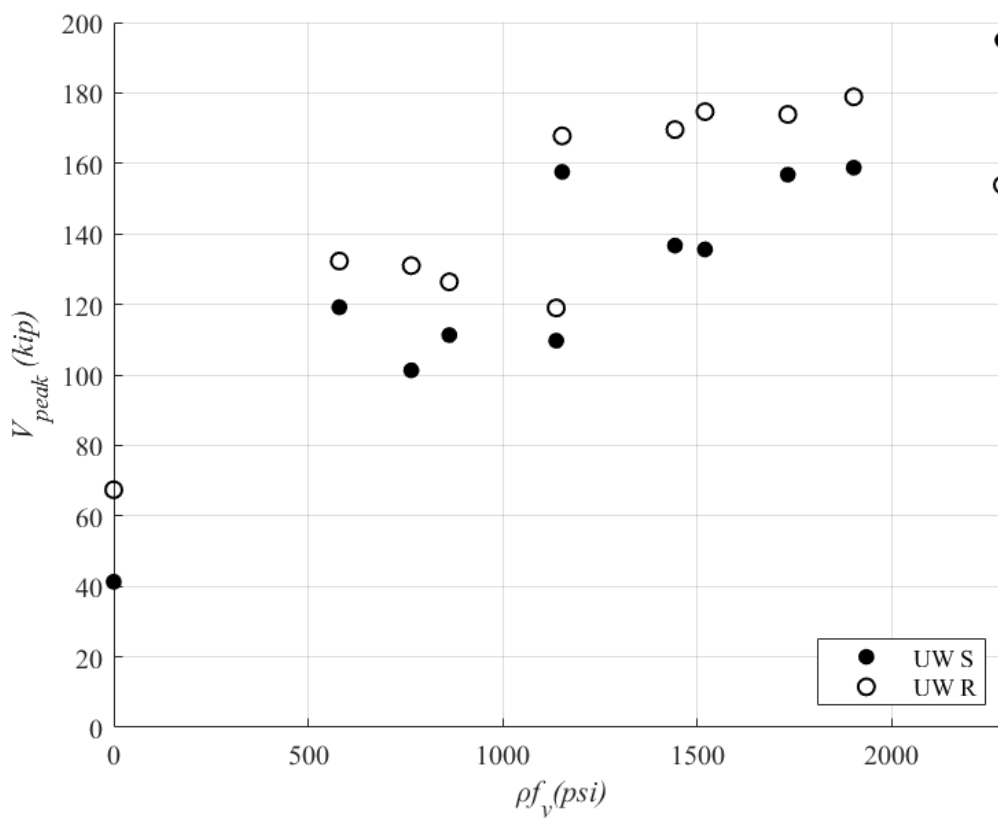


Figure 5.1: Peak shear load-theoretical clamping stress plot. Specimens are separated into two group: smooth and roughened. This plot does not include specimens that did not have roughened counterparts (i.e. UW60S-2 and UW80S-2).

The reinforcement ratio or the yield stress did not appear to affect the increase in capacity gained from roughening the interface, which meant that the increase in capacity was likely caused by the increase in cohesion. Comparing the percent increase of the peak shear load with the individual components of the clamping stress did not show any obvious trend. The 60 ksi specimens did not have a higher or lower percent increase in capacity compared to the 80 ksi specimens, and specimens with high reinforcement ratio did not have a higher or lower percent increase either. The comparisons are shown in Table 5-1.

The variables in

Table 5-1 are defined as follows:

- $V_{peak,S}$ is the recorded peak shear load of the smooth specimen.
- $V_{peak,R}$ is the recorded peak shear load of the roughened specimen.

Table 5-1: Comparison of the peak shear load between smooth and roughened specimens.

Specimen	ρ (%)	$V_{peak,S}$ (kip)	$V_{peak,R}$ (kip)	$V_{peak,R} - V_{peak,S}$ (kip)	% Difference
UW60-4	0.78	119.2	132.3	13.1	11.0%
UW60-6	1.16	105.4	126.4	21.0	20.0%
UW60-8	1.55	157.6	167.8	10.2	6.5%
UW60-10	1.94	136.7	169.6	32.9	24.1%
UW60-12	2.33	156.8	173.9	17.1	10.9%
UW80-4	0.78	101.3	131.0	29.7	29.3%
UW80-6	1.16	109.7	119.0	9.3	8.4%
UW80-8	1.55	135.6	174.7	39.1	28.8%
UW80-10	1.94	158.8	178.9	20.1	12.7%
UW80-12	2.33	195.0	153.9	-41.1	-21.1%

The specimens designed to isolate the effect of cohesion, UW0S and UW0R, were analyzed. The difference in peak shear load attributed to the different roughness conditions, ΔV_{surf} , was 26.2 kips. When this difference was added to the peak shear load of the smooth specimens, the shear load approached the peak shear load of the equivalent roughened specimens. For example, UW60S-6 reached a peak shear load of 105.4 kips, and UW60R-6 reached a peak shear load of 126.4 kips. When ΔV_{surf} of 26.2 kips was added to the peak shear load of UW60S-6, the ratio between peak shear load of UW60R-6 and the modified peak shear load of UW60S-6 was calculated as 0.96. The average of the ratio between the peak shear load of roughened specimens and the peak shear load of smooth specimen with ΔV_{surf} added was 0.97 with CV of 10.5% (These results are summarized in Table 5-2). This showed that the cohesion contribution was roughly consistent amongst specimens with similar interface conditions, suggesting that cohesion may be treated as an additive property to the overall shear-transfer capacity.

Table 5-2: Tables exploring the additive qualities of cohesion and roughness. Letters indicating the surface condition of the specimen in the specimen labels (S and R) are disregarded in this table.

Specimen	V_{peak} (kip)	
UW0S	41.3	
UW0R	67.4	
$\Delta V_{surf} =$	26.2	

Specimen	$V_{peak,S}$ (kip)	$V_{peak,S} + \Delta V_{surf}$ (kip)	$V_{peak,R}$ (kip)	$V_{peak,R}/(V_{peak,S} + \Delta V_{surf})$
UW60-4	119.2	145.4	132.3	0.91
UW60-6	105.4	131.6	126.4	0.96
UW60-8	157.6	183.8	167.8	0.91
UW60-10	136.7	162.8	169.6	1.04
UW60-12	156.8	183.0	173.9	0.95
UW80-4	101.3	127.4	131.0	1.03
UW80-6	109.7	135.9	119.0	0.88
UW80-8	135.6	161.7	174.7	1.08
UW80-10	158.8	184.9	178.9	0.97
UW80-12	195.0	221.1	153.9	0.70
Avg. =				0.97
CV =				10.5%

The additive property of cohesion was further supported by the analysis of the residual load of the specimens. Since cohesion's contribution to the shear-transfer capacity should be negligible after the peak load, the difference between the peak shear load and the residual load should show a clear distinction between smooth and roughened specimens with same reinforcement ratio and yield strength of the reinforcing bars. For example, the difference between peak and residual load, $\Delta V_{residual}$ of UW80S-6 was 16.4 kips, while the $\Delta V_{residual}$ of UW80R-6 was 34.0 kips. The roughened specimens consistently had a larger difference between peak and residual load. The average drop in load of smooth specimens, excluding UW60S-2 and UW80S-2 (later discussed in Section 5.2), was 18.2 kips with CV of 36%, and the average drop in load of roughened specimen was 36.1 kips with CV of 26%. The larger discrepancy was, again, attributed to the initial contribution from the cohesion being greater but not contributing after the peak shear load. Table 5-3 summarizes peak loads, residual loads, and differences between the two. Differences between peak and residual loads are also outlined in Figure 5.2.

Table 5-3: Comparing the difference in applied load at peak and at residual between specimens. Specimen UW60S-2 and UW80S-2 are bolded to note that these two specimens were not included in the average.

Specimen	V_{peak} (kip)	$V_{residual}$ (kip)	$\Delta V_{residual}$ (kip)
UW60S-2	99.1	48.2	50.8
UW60S-4	119.2	99.0	20.3
UW60S-6	111.3	96.8	14.5
UW60S-8	157.6	140.8	16.8
UW60S-10	136.7	125.5	11.1
UW60S-12	156.8	121.3	35.5
UW80S-2	88.1	49.2	38.9
UW80S-4	101.3	86.3	15.0
UW80S-6	109.7	93.4	16.4
UW80S-8	135.6	116.2	19.3
UW80S-10	158.8	143.6	15.2
UW80S-12	195.0	134.5	60.5
UW60R-4	132.3	88.1	44.2
UW60R-6	126.4	101.9	24.5
UW60R-8	167.8	121.4	46.5
UW60R-10	169.6	137.5	32.1
UW60R-12	173.9	131.5	42.5
UW80R-4	131.0	104.0	27.0
UW80R-6	119.0	98.1	20.9
UW80R-8	174.7	140.7	34.0
UW80R-10	178.9	133.4	45.5
UW80R-12	153.9	109.8	44.1

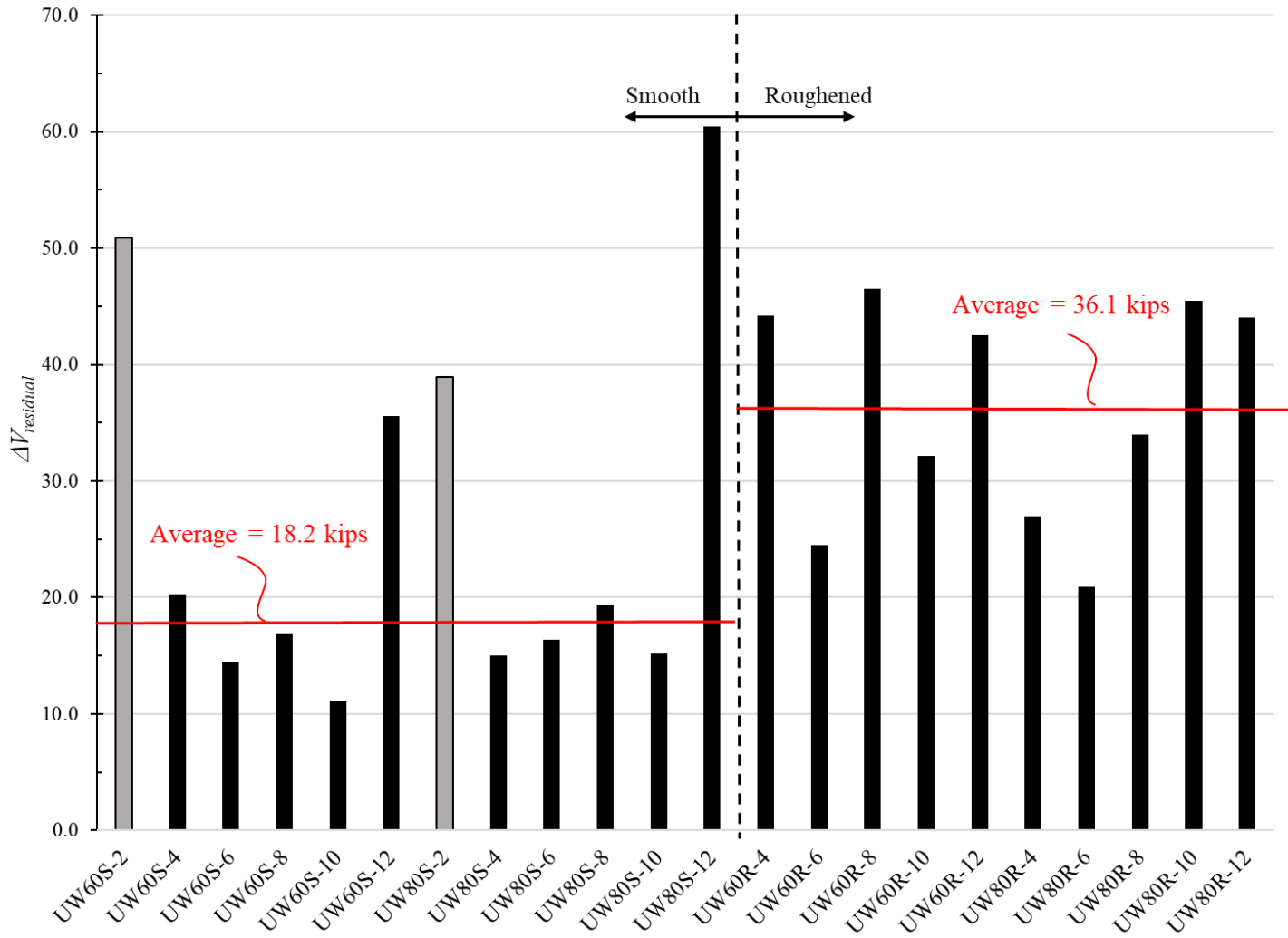


Figure 5.2: Drop in applied load from peak load to the residual load plotted for each specimens. The averages drop in load are shown. Specimen UW60S-2 and UW80S-2 are greyed out to note that these two specimens were not included in the average

5.1.2 Slip Displacement and Crack Width

The slip displacement and crack width data showed a consistent trend amongst pairs of specimens that had the same reinforcement ratio and yield strength but different interface roughness. In all cases except for the pair of specimens UW80S-6 and UW80R-6, roughened specimens had a lower slip displacement at peak load. In general, roughened specimens were stiffer, reaching higher peak loads at smaller slip displacements. In all cases, except for the pairs of specimens UW60S-6 and UW60R-6, and UW80S-8 and UW80R-8, crack width at peak load was also smaller for roughened specimens. Figure 5.3 and Figure 5.4 present the slip displacement-theoretical clamping stress plot and crack width-theoretical clamping stress plot, with the anomalies highlighted.

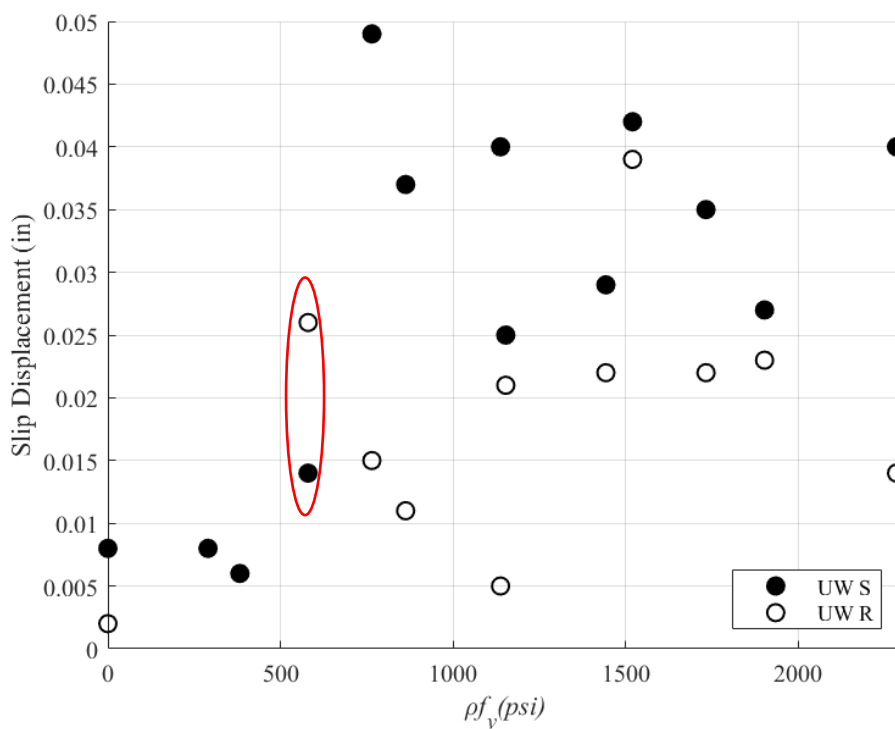


Figure 5.3: Slip displacement-theoretical clamping force plot. UW80S-6 and UW80R-6 are highlighted

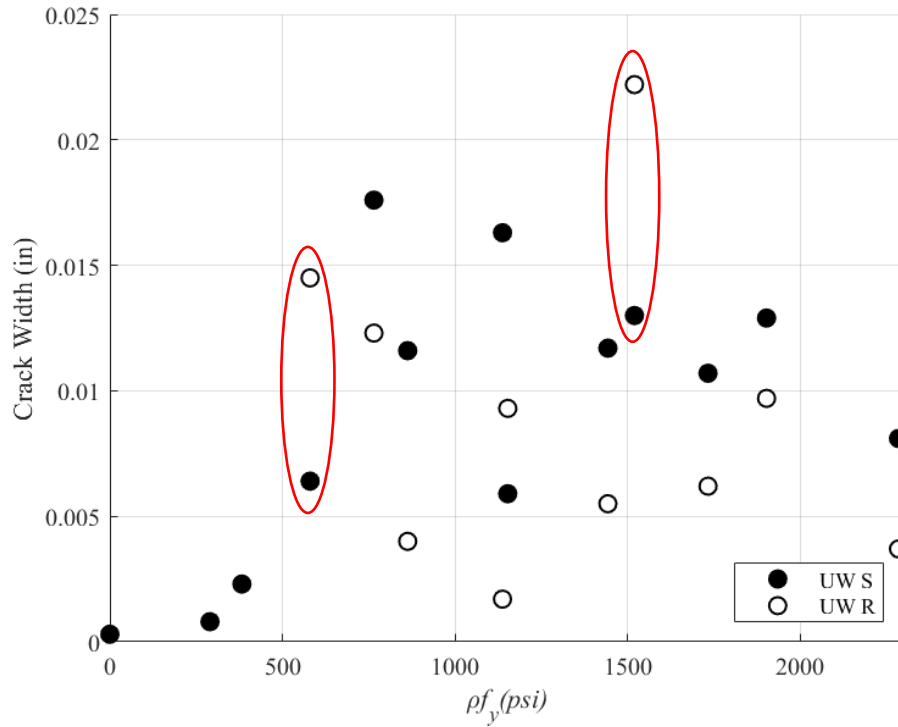


Figure 5.4: Crack width-theoretical clamping stress plot with UW60S-6, UW60R-6, UW80S-8, and UW80R-8 highlighted

Notable conclusions that can be drawn from the analysis of the experimental results outlined in this chapter include:

- The level of roughness achieved using surface retarders had a consistent effect on the peak shear load, slip displacement at peak load and crack width at peak load.
- Cohesion appears to have an additive quality to the shear transfer strength.

5.2 Influence of Reinforcement Ratio and Yield Strength

Considering that shear friction provisions rely heavily on the theoretical clamping stress of the reinforcement, ρf_y , to predict the peak shear load, theoretical clamping stress became the focal points of the analysis. The theoretical clamping stress is a function of two variables: the reinforcement ratio and the yield strength of reinforcing bars. These two variables were analyzed separately to study how they interact and influence both peak and post-peak shear-transfer capacity. The effects of the reinforcement parameters were also analyzed independently of the surface conditions of the specimens.

5.2.1 Peak Shear-Transfer Capacity

For the 12 smooth specimens, the peak shear load appeared to show a linear relationship with the theoretical clamping stress. This trend can be observed in Figure 5.5. Before normalizing the theoretical clamping stress by the yield stress, few observations were made regarding the impact of the reinforcement ratio. UW60S-8 reached a peak shear load 47.9 kips larger than the peak shear load reached by UW80S-6. The difference in peak shear load was significant for a pair of specimens sharing similar values of ρf_y (1,153 psi and 1,138 psi). This could be attributed to UW60S-8 having a higher reinforcement ratio (1.55% and 1.16%), but it could also be attributed to natural scatter of these specimens. Analyzing other pairs of specimens that share similar theoretical clamping stresses with different reinforcement ratios did not support the idea that reinforcement ratio alone had a significant affect on the peak shear-transfer capacity. Overall, smooth specimens that share similar theoretical clamping stresses reached similar peak shear loads. Few pairs of specimens that reached similar peak shear loads despite having different reinforcement ratios are highlighted in Figure 5.5.

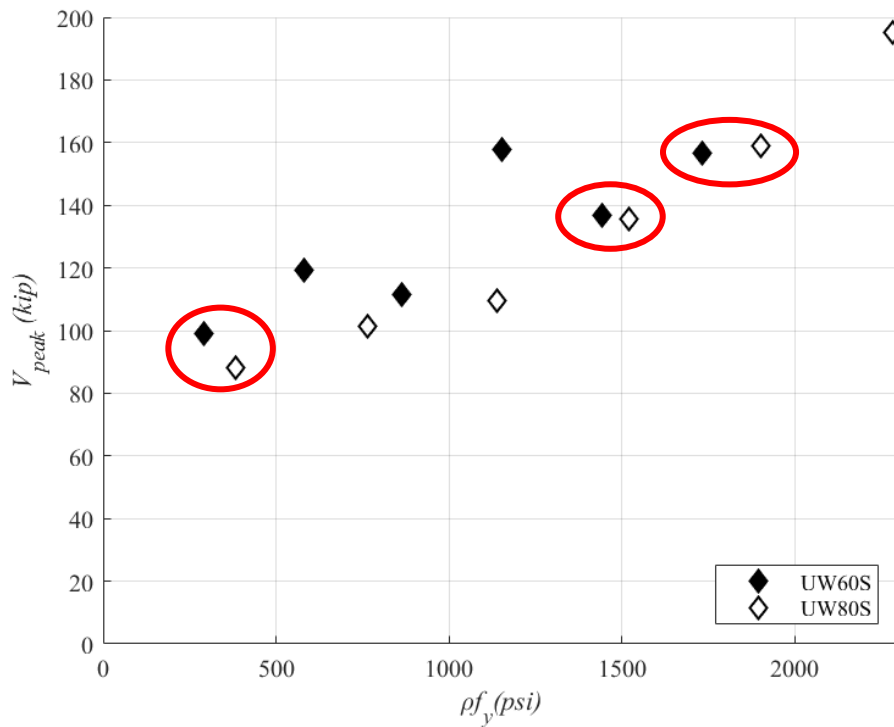


Figure 5.5: Peak shear load-theoretical clamping stress plot of smooth specimens

For the 10 roughened specimens, the peak shear load did not show a clear relationship with the theoretical clamping stress. The lack of trend can be observed in Figure 5.6. Again, comparing the pair of specimens UW60R-8 and UW80R-6 that share the similar values of ρf_y (1,153 psi and 1,138 psi) showed that the reinforcement ratio profoundly affected the peak shear-transfer capacity. The difference in peak shear load between the two specimens was 48.8 kips. Again, the different peak shear-transfer capacity could be attributed to UW60R-8 having a higher reinforcement ratio, but it could also be attributed to natural scatter. Similar to the group of smooth specimens, analyzing other pairs of specimens that share similar theoretical clamping stresses suggested that the reinforcement ratio alone did not significantly affect the peak shear-transfer capacity. Based on these results, it was difficult to support any definitive conclusions pertaining to the interaction between the reinforcement ratio and the yield strength, and their relationship with the interface shear strength. For the roughened specimens, upper stress limit appears to exist. Between five roughened specimens with nominal clamping stresses greater than 1,150 psi (UW60R-8, UW60R-10, UW60R-12, UW80R-8, and UW80R-10), the peak shear load only ranged from 167.7 kips to 178.8 kips. There was no clear explanation for why the peak shear load plateaued with the increasing theoretical clamping stress, but the existence of a strength upper limit agreed with

current shear friction provisions. The five specimens and the potential upper limit is highlighted in Figure 5.6.

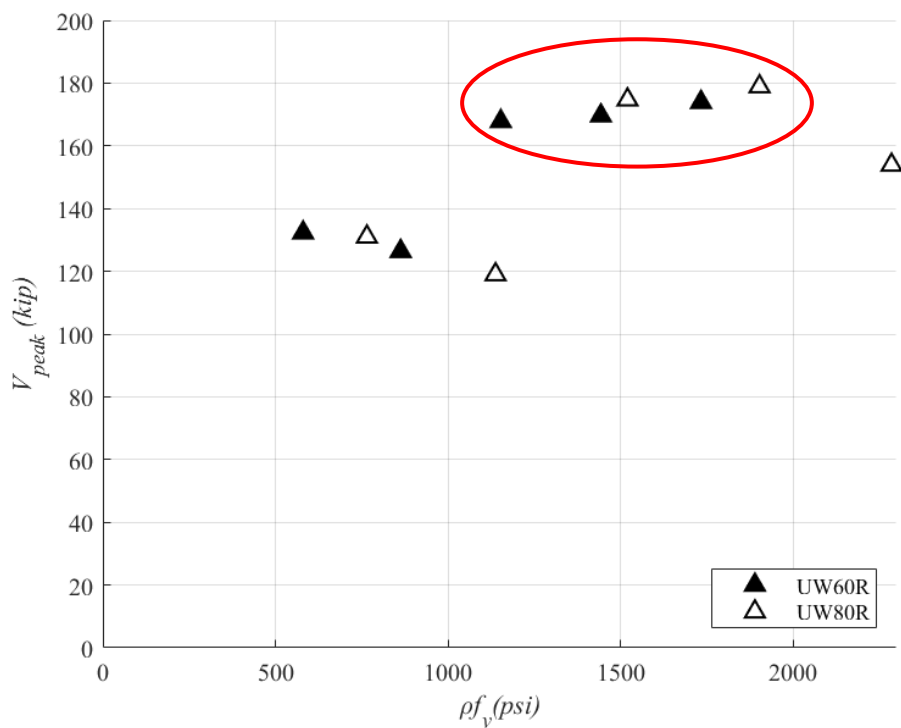


Figure 5.6: Peak shear load-theoretical clamping stress plot of roughened specimens

To further analyze the relationship between reinforcement ratio and yield strength, and the influence they have on the shear transfer capacity, Figure 5.5 and Figure 5.6 were normalized by the yield strength of the reinforcing bars. The resulting plots are shown in Figure 5.7 and Figure 5.8. Looking only at the group of smooth specimens, the yield strength of the bars did not increase the shear-transfer capacity notably. UW60S-6 and UW80S-6 reached similar peak shear loads despite UW80S-6 having a higher yield strength (74.4 ksi and 98.1 ksi) with the same reinforcement ratio. UW60S-6 reached a peak shear load of 111.3 kips and UW80S-6 reached a peak shear load of 109.7 kips. For all the specimens with reinforcement ratio less than 1.55%, 60 ksi specimens reached a higher peak shear load than the companion 80 ksi specimens. In contrast, for all specimens with reinforcement ratio greater than 1.55%, 80 ksi specimens reached a higher peak shear load than the companion 60 ksi specimens. Just from analyzing the smooth specimens, it was difficult to identify a trend between the yield strength and the peak shear load. However, again, there was a somewhat linear trend between reinforcement ratio and the peak shear load.

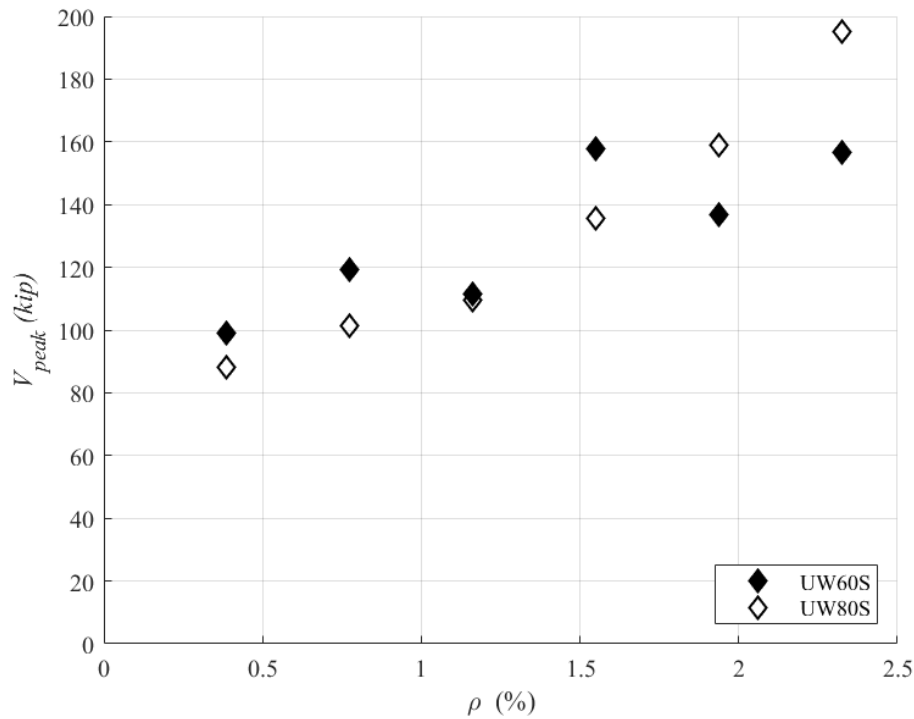


Figure 5.7: Peak-shear load-reinforcement ratio plot of the smooth specimens. 60 ksi specimens and 80 ksi specimens are marked differently.

Analyzing roughened specimens did not provide any additional insight. Most specimens with the same reinforcement ratio reached similar peak loads regardless of the yield strength. For example, UW60R-4 and UW80R-4 reached peak shear load of 132.3 kips and 131.0 kips, respectively. UW60R-8 and UW80R-8 reached peak shear load of 167.8 kips and 174.7 kips, respectively. The 80 ksi specimens from 2 of the 5 pairs reached a higher peak shear load than their respective 60 ksi counterparts. The other three pairs, 60 ksi specimens reached a higher peak shear load than their respective 80 ksi counterparts. The roughened specimens appeared to have been impacted by the upper stress limits, which made it more difficult to identify any direct relationship between the yield strength and the peak shear-transfer capacity.

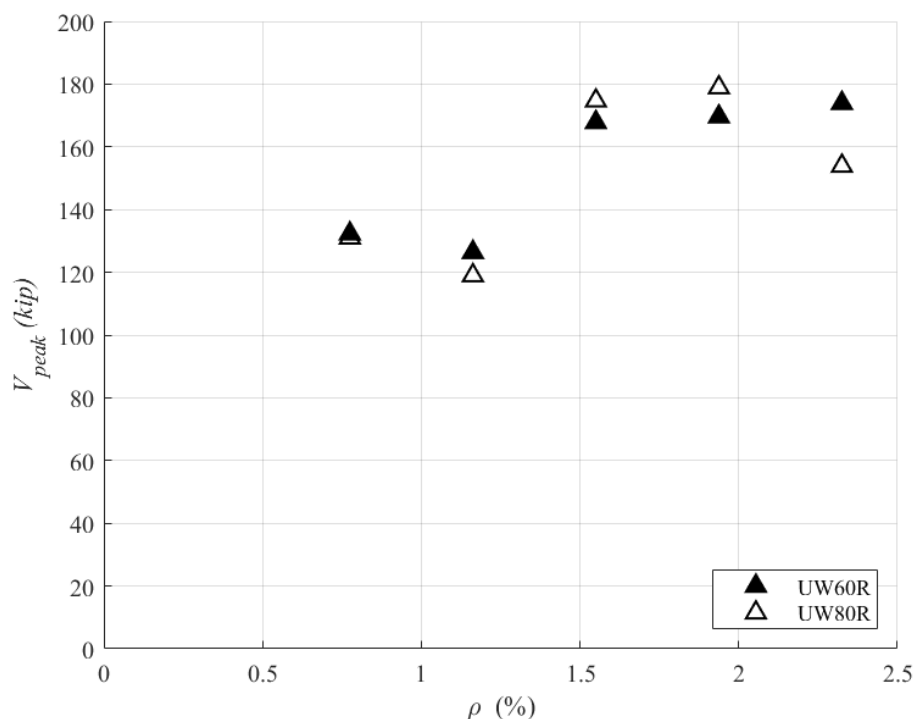


Figure 5.8: Peak-shear load-reinforcement ratio plot of the roughened specimens. The 60 ksi specimens and 80 ksi specimens are marked differently.

To better understand the role played by the steel reinforcement crossing the interface, with respect to the response of the specimens and their peak strength, the axial stress in the bars was analyzed more closely. This was done by estimating the axial stress levels in the bars, from the average strain gauge readings, summarized in Table 5-4. The readings collected revealed that none of the reinforcing bars yielded at peak, and that most bars were within 10% and 30% of their yield stress. This suggests that any strength related advantage gained from using higher strength reinforcement was not actualized at peak shear load. The reinforcement ratio likely influenced more of the peak shear-transfer capacity. UW60S-2, UW80S-2, and UW80S-4 appeared to be outliers in terms of the strain of the bars.

The low average strain of the bars in UW60S-2 and UW80S-2 was reflected on the overall behavior of the specimens as well. These two specimens behaved similarly to UW0S and UW0R. After reaching their respective peak shear load, their strength dropped sharply without showing any ductility. This suggested that there may be a minimum reinforcement ratio that must be provided to engage the reinforcing bars, so that they can contribute to the shear-transfer capacity.

Looking at the smooth specimens, the specified 80 ksi reinforcing bars consistently had higher axial strain than the specified 60 ksi reinforcing bars with the same reinforcement ratios. As a reminder, in all cases except for specimens with reinforcement ratio great than 1.55%, 60 ksi specimens had a higher peak shear load, so the reason behind 80 ksi reinforcing bars consistently reaching higher axial strain was unclear. For roughened specimens, both 60 ksi and 80 ksi reinforcing bars had similar axial strains, which again supported the idea that the yield strength of the reinforcing bars did not directly affect the peak shear-transfer capacity. Moreover, there was no obvious trend between the reinforcement ratio and the axial strain of the reinforcing bars. The lack of trend was reflected on both smooth and roughened specimens. Again, the strain data must be cautiously analyzed since the strain gauges were located 2 inches away from the interface. With such minimal overall movement of the specimens, the reinforcement must have been interacting locally.

Table 5-4 Average Strain and A at peak.

Specimen	f_y (ksi)	ϵ_y	Avg. ϵ_s
UW60S-2			0.0001
UW60S-4			0.0008
UW60S-6	74.4	0.0058	0.0010
UW60S-8			0.0006
UW60S-10			0.0009
UW60S-12			0.0009
UW80S-2			0.0003
UW80S-4			0.0023
UW80S-6	98.1	0.0040	0.0014
UW80S-8			0.0012
UW80S-10			0.0010
UW80S-12			0.0012
UW60R-4			0.0009
UW60R-6			0.0007
UW60R-8	74.4	0.0058	0.0010
UW60R-10			0.0009
UW60R-12			0.0008
UW80R-4			0.0008
UW80R-6			0.0007
UW80R-8	98.1	0.0040	0.0012
UW80R-10			0.0011
UW80R-12			0.0010

Strain gauges may not have captured any local behaviors, but the peak shear load results support the notion that the bars did not yield at peak. If the shear-transfer capacity was truly driven by the theoretical clamping stress, then the peak shear load of 80 ksi specimens should be 32% higher than the peak shear load of 60 ksi specimens based on the percent difference in the yield strength. However, this was not the case.

Normalizing the results by the yield strength showed that the yield strength of the reinforcing bars alone did not directly correlate to the shear-transfer capacity. But going back to a previous discussion on the relationship between theoretical clamping stress and peak shear-transfer capacity, analyzing both smooth and roughened specimens together showed that using higher strength reinforcement with smaller reinforcement ratio did not necessarily affect the shear-transfer capacity in a negative way. Only pairs of specimens that showed a big difference in the peak shear load were UW60S-8 and UW80S-6, and UW60R-8 and UW80R-6. The other specimens showed that within similar theoretical clamping stresses, the peak shear-transfer capacity was similar as well.

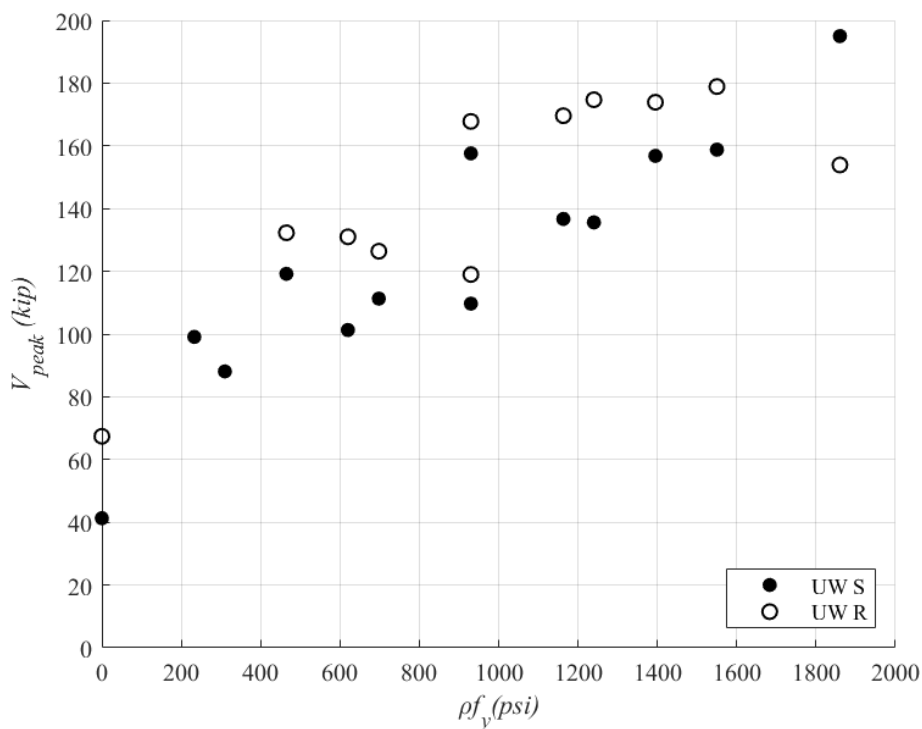


Figure 5.9: Peak shear load-theoretical clamping stress plot include all specimens.

5.2.2 Post-peak Shear-Transfer Capacity

Post-peak response of the specimen appeared to be governed by some mechanism related to the reinforcement ratio. The residual load was similar amongst specimens with same values of ρ . For example, UW60S-10, UW80S-10, UW60R-10 and UW80R-10 ($\rho = 1.94\%$) had residual load of 125.52 kips, 143.62 kips, 137.46 kips, and 140.70 kips, respectively, with an average of 135 kips and CV of 5%. The results pertaining to the average residual load of specimens that share the same reinforcement ratio are tabulated in Table 5-5 (note the low coefficient of variation). It should be noted that the residual load was reported as the recorded applied load corresponding to an arbitrary value of slip displacement from the peak load. The reported values of the residual load can change with a different definition of the residual load.

Table 5-5 Average residual load with respect to the reinforcement ratio

ρ (%)	Avg. $V_{residual}$ (kip)	St. Dev (kip)	CV (%)
0.39	48.7	0.5	1%
0.78	94.3	7.4	8%
1.16	97.6	3.1	3%
1.55	129.8	11.1	9%
1.94	135.0	6.6	5%
2.33	124.3	9.7	8%

Resistance to interface shear post-peak was often attributed to dowel action of the bars. However, dowel action is still a function of the yield strength, and as discussed, there was no clear distinction between 60 ksi and 80 ksi specimens. The resistance to applied load could potentially come from the concrete's ability to resist bearing pressure from the reinforcing bars. This theory would align well with reinforcement ratio having a positive correlation with the residual load. The photographs of the reinforcing bars after the test clearly show where the reinforcement used to be, and the bond failure can be clearly seen in Figure 5.10. There was no conclusive evidence to theorize where the bulk of residual capacity came from. Effects of bond and other concrete properties were outside of the scope of this experimental program, and any further comments regarding dowel action were not made.



Figure 5.10: Close up of the revealed reinforcement after test (UW80S-6 West side).

Several conclusions could be drawn from analyzing both reinforcement parameters:

- In most cases, when the value of the theoretical clamping stresses was similar, the peak shear-transfer capacity was similar as well. However, yield strength alone did not show a strong correlation with the shear-transfer capacity at peak and post-peak.
- The reinforcing bars did not yield at peak. Based on the strain gauges attached 2 inches away from the interface, most bars reached within 10% to 30% of the respective yield strength.
- There is a minimum reinforcement ratio that appears to be needed to activate the reinforcing bars so that they to provide resistance to shear. The specimens with low theoretical clamping stresses were very brittle and behaved analogously to specimens with no reinforcing bars crossing the interface. The reinforcing bars had negligible engagement as well.
- Post-peak response was mostly likely governed by the bond and the concrete's ability to resist the bearing pressure.

Chapter 6: Evaluation of ACI, AASHTO, and Proposed Shear Friction Provisions

In this chapter, the current ACI and AASHTO shear friction provisions were compared with the experimental results described in Chapters 4 and 5. Additionally, alternative ACI shear friction provisions from ACI318-11 and a shear friction provisions recently proposed by Davaadorj [9] were evaluated. To improve the accuracy of the prediction equation, a newly proposed equation was evaluated. These evaluations used both the experimental results from this study as well as a previously tested cold-joint specimens. Based on these evaluations, a modified version of the model from Davaadorj [9] is proposed.

The components of the model should reflect the experimental findings. The key observations made in Chapter 5 are as follows:

- The interface roughness increased the interface shear strength.
- The magnitude of increase in peak shear load was relatively consistent amongst all specimens. This increase in peak shear load was approximately the difference in shear capacity of the smooth and roughened specimens without reinforcement (i.e. UW0S and UW0R).
- The interface shear strength did not depend on the strength of the reinforcing bars but did depend on the theoretical clamping stress.
- The reinforcing bars did not yield at the peak strength of the specimen.
- Considering all the experimental tests indicates that there is a limit to the interface strength which depends on the concrete properties and interface properties and is independent of the steel reinforcement provided.

These observations were used to evaluate and improve existing models that estimate the interface shear strength.

6.1 Evaluation of the Current ACI and AASHTO Shear Friction Provisions with UW Specimens

The ACI 318-19 shear friction provisions are described in detail in Chapter 2. The key equation to assess the interface strength is reported below for convenience:

$$V_n = \mu A_{vf} F_y \quad \text{Eq. 6.1}$$

Where,

V_n = Nominal shear strength

μ = Coefficient of friction

A_{vf} = Area of the reinforcing bars crossing the interface

F_y = Yield strength of the reinforcing bars crossing the interface

Table 6-1: Table 22.9.4.4 from ACI 318-14 recreated

Condition	Maximum V_n	
Normal weight concrete placed monolithically or placed against hardened concrete intentionally roughened to a full amplitude of approximately 1/4 in.	Least of (a), (b), and (c)	$0.20f'_c A_c$ (a)
		$(480 + 0.08f'_c)A_c$ (b)
		$1600A_c$ (c)
Other cases	Lesser of (d) and (e)	$0.20f'_c A_c$ (d)
		$800A_c$ (e)

The AASHTO shear friction equation and upper stress limits are given below:

$$V_{ni} = cA_{cv} + \mu(A_{vf}f_y + P_c)$$

$$V_{ni} \leq K_1 f'_c A_{cv},$$

$$V_{ni} \leq K_2 A_{cv}$$

Eq. 6.2

Where,

V_{ni} = Nominal design shear strength

c = Cohesion factor

A_{cv} = Area of the interface

μ = Coefficient of friction

A_{vf} = Area of the reinforcing bars crossing the interface

f_y = Yield strength of the reinforcing bars crossing the interface

P_c = Externally applied clamping load

K_1 = Fraction of concrete strength available to resist interface shear (i.e. concrete strength limit).

K_2 = Limiting interface shear resistance (i.e. interface limit)

Table 6-2: AASHTO Prescribed values for cohesion factor, coefficient of friction and limit states

Interface Type	c (ksi)	μ	K_1	K_2 (ksi)
Monolithic	0.4	1.4	0.25	1.5
Cold joint (Rough)	0.24	1.0	0.25	1.5
Cold joint (Smooth)	0.075	0.6	0.2	0.8

For each specimen, the expressions and measured material properties were used to calculate the strength using the ACI and AASHTO shear friction provisions. The shear-transfer capacities were divided by the interface area ($A_{cv} = 160 \text{ in}^2$) to convert them to shear stresses. The predicted values and the average measured-to-predicted strength ratio, $\tau_{measured}/\tau_{ACI}$ and $\tau_{measured}/\tau_{AASHTO}$, are provided in Table 6-3. Most of the UW specimens had a high theoretical clamping stress that allowed the upper stress limit from ACI to govern the nominal shear strength ($0.6\rho f_y > 800 \text{ psi}$ for smooth and $\rho f_y > 950 \text{ psi}$ for roughened, given a value of f'_c below 6,000 psi). Therefore, evaluation of these specimens was useful in assessing the upper stress limits imposed in different shear friction provisions. Specimens from test series 0 were not included in the evaluation following the minimum reinforcement requirement in AASHTO.

Table 6-3: Table comparing test results with ACI's and AASHTO's predictions. Bolded numbers indicate the upper stress limits. Underline numbers highlight the ratios that fall below 1.0

Specimen	ρf_y (psi)	$\tau_{measured}$ (psi)	τ_{ACI} (psi)	$\tau_{measured}/\tau_{ACI}$	τ_{AASHTO} (psi)	$\tau_{measured}/\tau_{AASHTO}$
UW60S-2	290	619	174	3.56	249	2.49
UW60S-4	580	745	348	2.14	423	1.76
UW60S-6	863	659	518	1.27	593	1.11
UW60S-8	1153	985	692	1.42	767	1.28
UW60S-10	1443	854	800	1.07	800	1.07
UW60S-12	1734	980	800	1.23	800	1.23
UW80S-2	383	551	230	2.40	305	1.81
UW80S-4	765	633	459	1.38	534	1.19
UW80S-6	1138	686	683	1.00	758	<u>0.90</u>
UW80S-8	1521	847	800	1.06	800	1.06
UW80S-10	1903	992	800	1.24	800	1.24
UW80S-12	2286	1219	800	1.52	800	1.52
UW60R-4	580	827	580	1.43	820	1.01
UW60R-6	863	790	863	<u>0.92</u>	1103	<u>0.72</u>
UW60R-8	1153	1049	948	1.11	1393	<u>0.75</u>
UW60R-10	1443	1060	948	1.12	1463	<u>0.72</u>
UW60R-12	1734	1087	948	1.15	1463	<u>0.74</u>
UW80R-4	765	819	765	1.07	1005	<u>0.81</u>
UW80R-6	1138	744	948	<u>0.78</u>	1378	<u>0.54</u>
UW80R-8	1521	1092	948	1.15	1463	<u>0.75</u>
UW80R-10	1903	1118	948	1.18	1463	<u>0.76</u>
UW80R-12	2286	962	948	1.01	1463	<u>0.66</u>

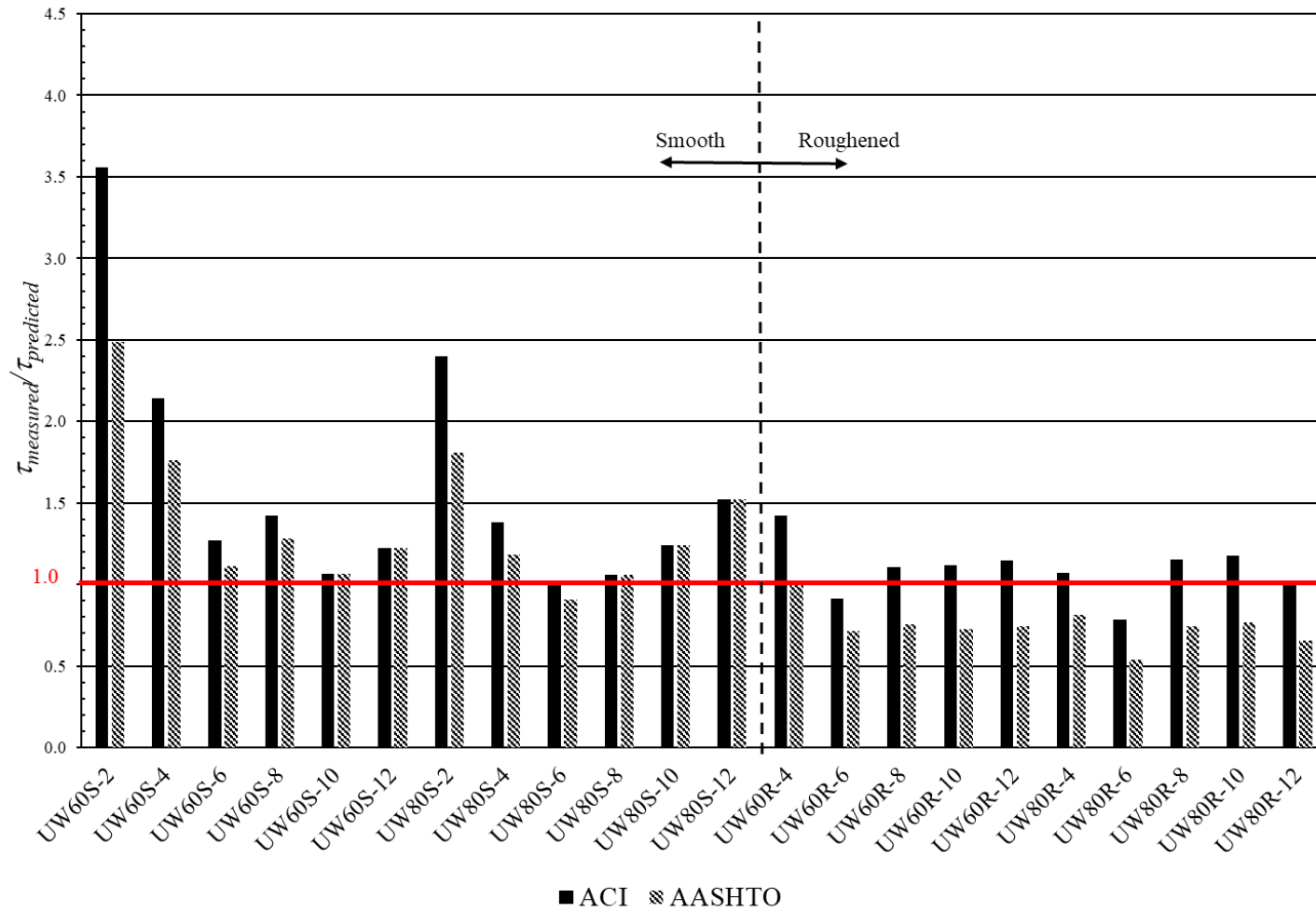


Figure 6.1: Charting the measured-to-predicted strength ratio of ACI and AASHTO models with UW specimens

The average of $\tau_{measured}/\tau_{ACI}$ of all smooth specimens was 1.61 and the average $\tau_{measured}/\tau_{AASHTO}$ of these specimens was 1.39. Both code provisions underestimated the capacity. AASHTO predictions were closer to the measured values because of the inclusion of the cohesion term. For smooth specimens with theoretical clamping stresses below 800 psi (the upper stress limit for smooth specimens in both ACI and AASHTO shear friction provision), both ACI and AASHTO further underestimated the capacity. The average of $\tau_{measured}/\tau_{ACI}$ of these specimens was 2.37, and the average of $\tau_{measured}/\tau_{AASHTO}$ of these specimens was 1.67. The average of $\tau_{measured}/\tau_{ACI}$ of smooth specimens with theoretical clamping stresses above 800 psi was 1.23 and the average of $\tau_{measured}/\tau_{AASHTO}$ of these specimens was 1.19. These ratios were closer to the desired ratio of 1.0, meaning that the upper stress limit in ACI and in AASHTO for smooth specimens were fairly accurate. Table 6-4 tabulates the average ratios from both ACI and AASHTO shear friction provisions. Figure 6.2 below shows the peak shear stress-theoretical clamping stress plot with UW specimens and the ACI and AASHTO upper stress limits when value of f'_c is 5,651 psi:

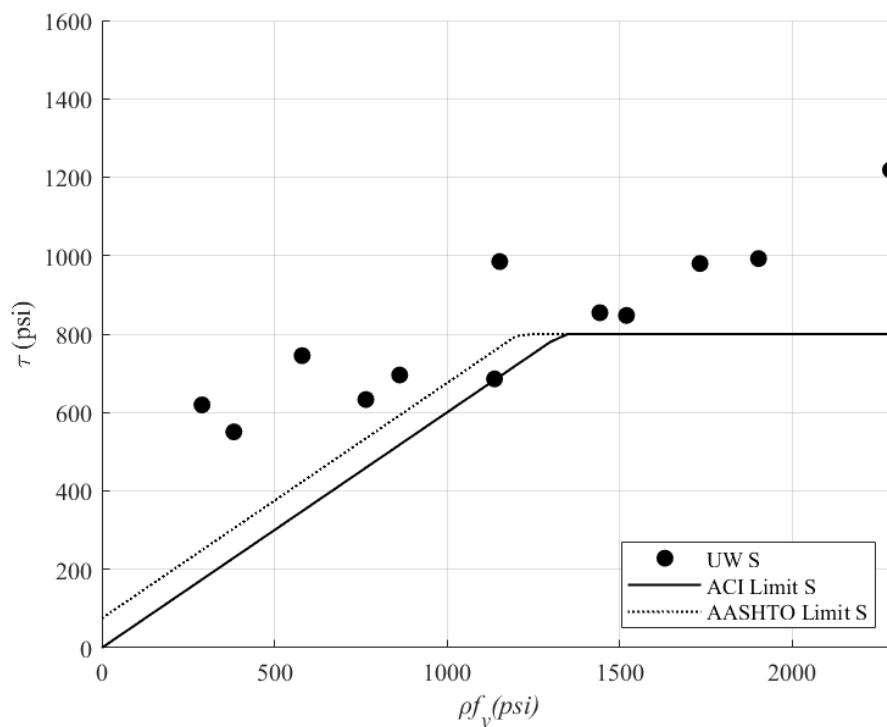


Figure 6.2: Peak-shear stress-theoretical clamping stress plot with UW specimens and ACI and AASHTO upper stress limits (smooth specimens only)

For all specimens with roughened interfaces, AASHTO overestimated the interface shear strength, while ACI provided reasonably accurate estimates of the measured stresses. The average of $\tau_{measured}/\tau_{ACI}$ was 1.09 and the average of $\tau_{measured}/\tau_{AASHTO}$ was 0.75. For roughened specimens with theoretical clamping stress below 950 psi (the upper stress limit for roughened specimens in ACI when value of f'_c is 5,850 psi), the average of $\tau_{measured}/\tau_{ACI}$ was 1.14 and the average of $\tau_{measured}/\tau_{AASHTO}$ of these specimens was 0.85. Both shear friction provisions were close to the measured values for specimens with low clamping stresses, but AASHTO fell below the desired ratio of 1.0. The ACI shear friction provision closely matched the measured peak shear stresses for specimens with higher theoretical clamping stresses ($\rho f_y > 950$ psi). The average $\tau_{measured}/\tau_{ACI}$ was 1.07. The AASHTO shear friction provision overestimated the peak shear stress values because the stress limits for roughened specimens with high theoretical clamping stress was higher. The average of $\tau_{measured}/\tau_{AASHTO}$ was 0.70. Figure 6.3 below shows the peak shear stress-theoretical clamping stress plot with UW specimens and the ACI and AASHTO upper stress limits when value of f'_c is 5,850 psi:

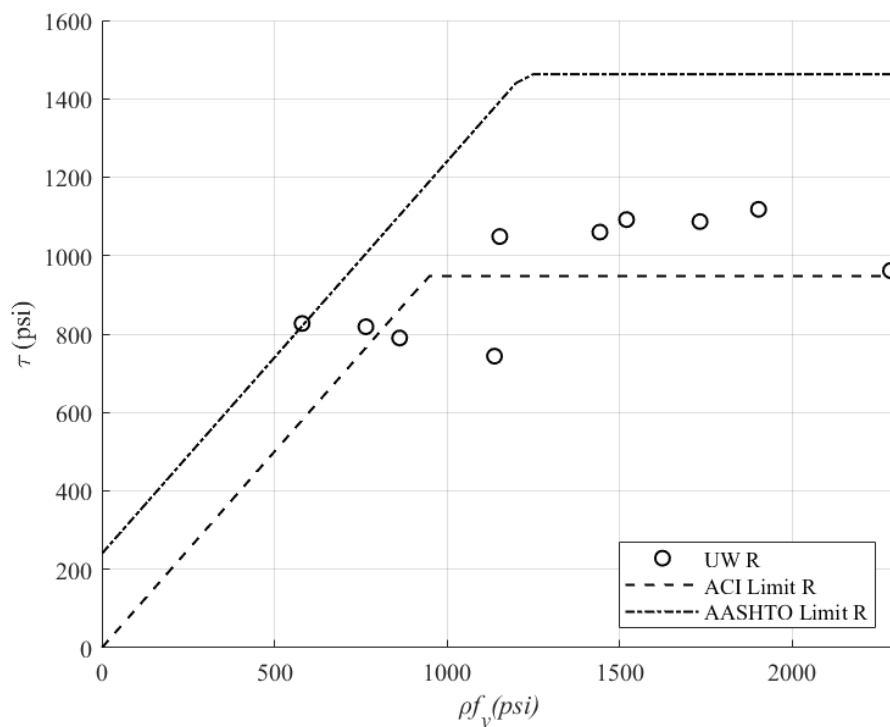


Figure 6.3: Peak-shear stress-theoretical clamping stress plot with UW specimens and ACI and AASHTO upper stress limits (roughened specimens only).

Table 6-4: Comparison of average measured-to-predicted strength ratio of UW specimens. Coefficients of variance are also tabulated.

Specimen Type	# of Specimens	ACI		AASHTO	
		$\tau_{measured}/\tau_{predicted}$	CV (%)	$\tau_{measured}/\tau_{predicted}$	CV (%)
CJ-S _{UW}	12	1.61	45%	1.39	31%
CJ-S _{UW, $\rho_f y < 800$}	4	2.37	33%	1.67	30%
CJ-S _{UW, $\rho_f y > 800$}	8	1.23	14%	1.19	16%
CJ-R _{UW}	10	1.09	15%	0.75	15%
CJ-R _{UW, $\rho_f y < 950$}	3	1.14	19%	0.85	14%
CJ-R _{UW, $\rho_f y > 950$}	7	1.07	12%	0.70	11%
CJ _{UW}	22	1.37	44%	1.10	41%

Previous discussion of the experimental results in Chapter 5 showed that, at least for the roughened specimens, the shear-transfer capacity was independent of the reinforcement ratio and yield strength beyond a certain value of the theoretical clamping stress. Both ACI and AASHTO upper stress limits are a function of the concrete compressive strength and the total interface area, which are in line with the findings. Both ACI and AASHTO design stress limits for smooth specimens were identical and provided adequately conservative estimates. ACI design limit for roughened specimens were comparable to the experimental results, but AASHTO design limits were not. The low ratio was mostly reflected on the K_I -factor, which represents the fraction of concrete strength available to resist interface shear (i.e. concrete strength limit). While the ACI provision uses 0.2 to represent that same constant, the AASHTO provision uses K_I -factor of 0.25 for cold joints with roughened surfaces, which significantly increases the AASHTO's upper stress limit from 1,180 psi to 1,475 psi.

6.2 Evaluation of the Current ACI and AASHTO Shear Friction Provisions with the Database

Both ACI and AASHTO provisions were evaluated using the combined database, which include the UW specimens. Most of the specimens in the database have a value of theoretical clamping stress below 1,000 psi, which is ideal for evaluating the shear friction equation itself. Figure 6.4 and Figure 6.5 plot the peak shear stress against theoretical clamping stress, and UW specimens are colorized to highlight that UW specimens had significantly higher theoretical clamping stress than the specimens in the database. Table including all the specimens in the database are in the appendix. The average ratios are outlined in Table 6-5.

Table 6-5: Comparing ACI and AASHTO to the database, with and without UW specimens

Specimen Type	# of Specimens	ACI		AASHTO	
		$\tau_{measured}/\tau_{predicted}$	CV (%)	$\tau_{measured}/\tau_{predicted}$	CV (%)
CJ-S _{UW}	12	1.61	45%	1.39	31%
CJ-S	20	1.75	38%	1.50	29%
CJ-R _{UW}	10	1.09	15%	0.75	15%
CJ-R	60	2.00	57%	1.19	32%
CJ _{UW}	22	1.37	44%	1.10	41%
CJ	80	1.94	54%	1.26	33%

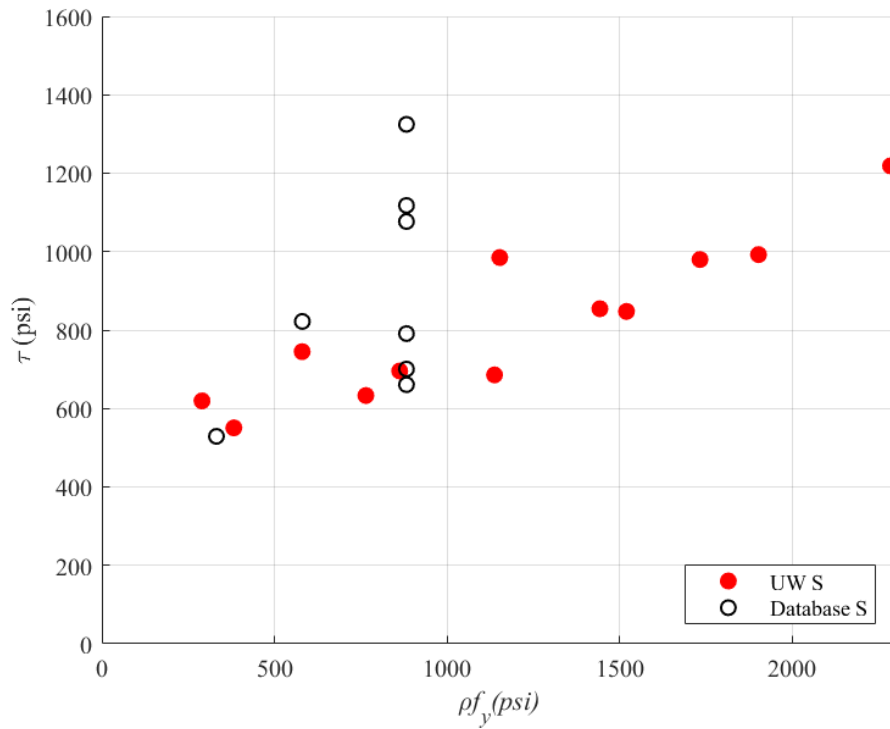


Figure 6.4: Peak shear stress-theoretical clamping stress plot for all smooth specimens

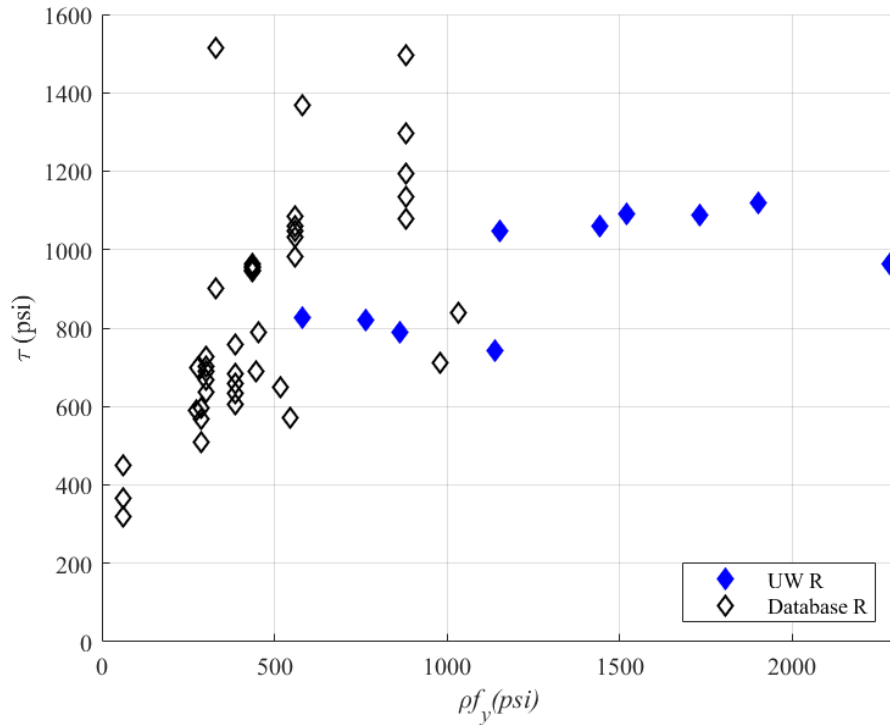


Figure 6.5: Peak shear stress-theoretical clamping stress plot for all roughened specimens

For all smooth specimens, the average of $\tau_{measured}/\tau_{ACI}$ ratio was 1.75, and the average of $\tau_{measured}/\tau_{AASHTO}$ ratio was 1.50. The average of $\tau_{measured}/\tau_{ACI}$ ratio for smooth specimens with clamping stress below 800 psi was 2.41, and the average of $\tau_{measured}/\tau_{AASHTO}$ ratio was 1.85. Both codes still underestimated the shear-transfer capacities of smooth specimens especially the specimens with low clamping stresses. For roughened specimens, the average of $\tau_{measured}/\tau_{ACI}$ was 2.00 and the average of $\tau_{measured}/\tau_{AASHTO}$ was 1.19. For roughened specimens with theoretical clamping stress below 950 psi the average of $\tau_{measured}/\tau_{ACI}$ was 2.19 and the average of $\tau_{measured}/\tau_{AASHTO}$ was 1.26. Focusing only on the roughened specimens with theoretical clamping stress above 950 psi, the average of $\tau_{measured}/\tau_{ACI}$ was 1.22 and the average of $\tau_{measured}/\tau_{AASHTO}$ was 0.90. Again, ACI underestimated the capacity of specimens with low clamping stresses. Overall predictions from AASHTO were more accurate for roughened specimens, but still fell below the ratio of 1.0.

6.3 Evaluation of Other Shear Friction Models

Two other shear friction models were evaluated for specific reasons. The first model discussed comes from ACI 318-11 [2]. It was an interesting model with a fixed value for the coefficient of friction factor. In this case, the coefficient of friction factor is better defined as the percentage of the shear-transfer capacity provided by the reinforcement. The second model discussed is the shear friction equation from Davaadorj [9] that was optimized based on the shear friction database with the UW specimens. The proposed model discussed in section 6.4 was based primarily off the second model for its accurate predictions of the peak shear-transfer capacity.

The shear friction equation from the commentary section in ACI318-11 (R11.6.3) is shown below:

$$V_n = 0.8A_v f_y + A_c K_I \quad \text{Eq. 6.3}$$

Where,

A_c = Area of concrete interface

K_I = Cohesion factor, 400 psi for normal-weight concrete

Other variables are defined previously in Eq. 6.1.

This equation was recommended by ACI if the designer desired a “closer estimate of the shear-transfer strength.” As observed in Chapter 5, the interaction between cohesion and reinforcement was largely independent. Then, having a separate cohesion term should account for the difference in the surface condition, meaning changing the coefficient of friction term would be redundant. This model had a fixed coefficient of friction term equal to 0.8, regardless of the interface conditions. The accuracy of this model was also assessed against the current experimental results and the database that includes the experimental results. The measured-to-predicted strength ratios obtained are shown in Table 6-6 and plotted in Figure 6.6.

Table 6-6: Average measured-to-predicted strength ratio of the model from ACI318-11

Specimen Type	# of Specimens	ACI318-11	
		$\tau_{measured}/\tau_{predicted}$	CV (%)
CJ-S	20	1.40	32%
CJ-R	60	1.17	28%
CJ	80	1.23	30%

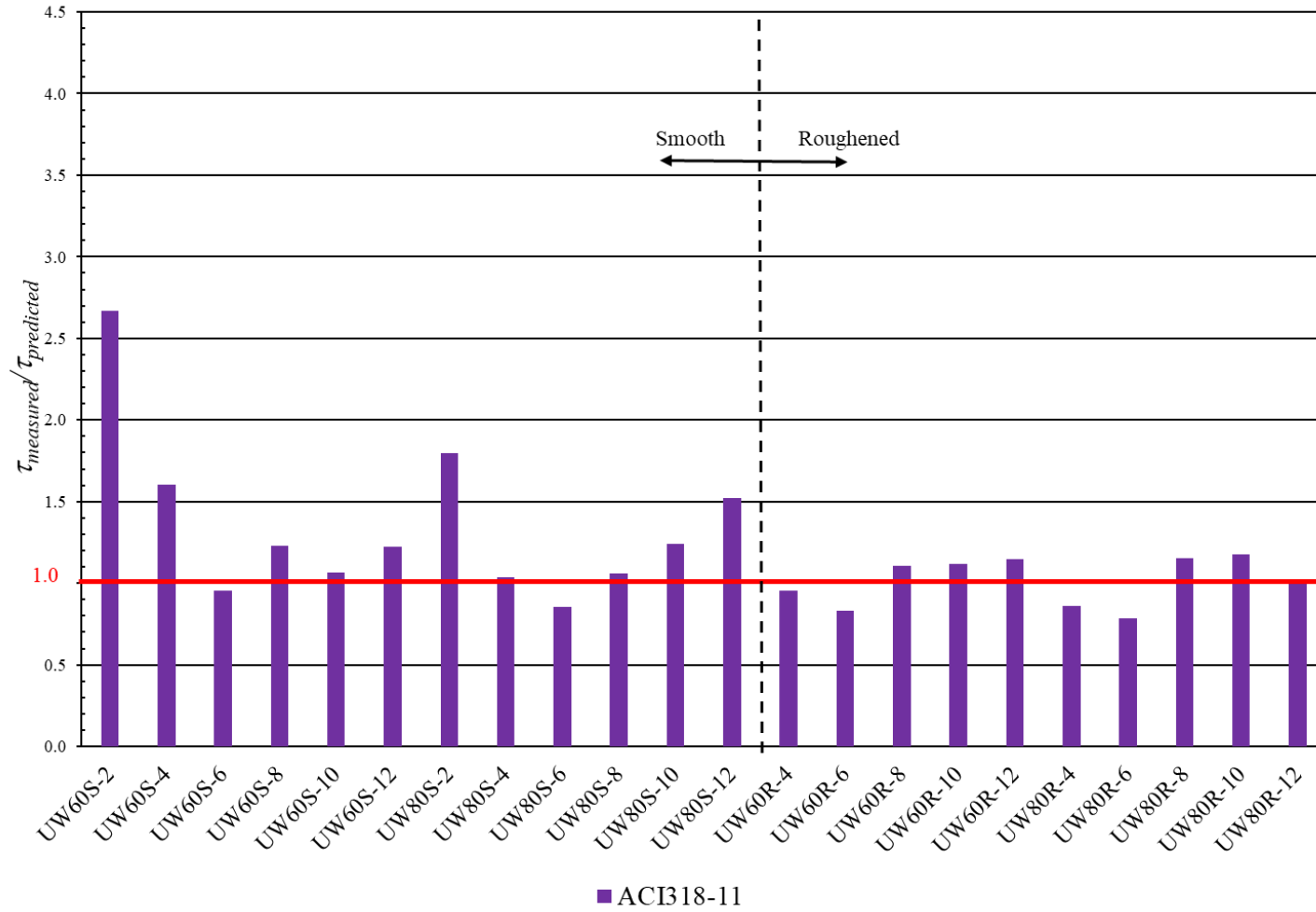


Figure 6.6: The average measured-to-predicted strength ratio of the model from ACI318-11 (UW specimens only)

Davaadorj [9] used a database of 509 specimens to identify trends related to concrete and reinforcement parameters. The key observations that the authors made are generally consistent with the key observations made based on the results of the current experimental program:

- Beyond a certain value of theoretical clamping stress, the concrete and the interface does not allow the utilization of additional reinforcement. Therefore, there should be an upper limit based on the concrete's compressive strength.
- Specimens with similar theoretical clamping stresses reached similar peak load regardless of the yield strength of the steel reinforcement (specified $f_y \leq 80$ ksi).

The paper by Davaadorj [9] compared 14 of the main strength models proposed by different authors and the current code provisions to assess their accuracy at predicting the shear-transfer capacity. Upon evaluation of the strength models, the authors concluded that AASHTO approach provided the best strength estimates. However, all models predicted poorly the response of CJ-S specimens, and it appeared that there was room for improving the strength equations for CJ-R specimens. Thus, Davaadorj proposed a modified shear friction equation (Eq. 6.4). The constant factors in the equation proposed by Davaadorj [9] was optimized based on the available database at the time. The results from the equation were compared to the experimental results. The equation is shown below:

$$\begin{aligned}\tau_n &= A_1 f'_c + A_2 \rho f_y \\ \tau_n &\leq K_1 f'_c, \\ \tau_n &\leq K_2 f'_c + K_3 \\ \tau_n &\leq K_4\end{aligned}\tag{Eq. 6.4}$$

Where,

A_1 = Cohesion factor

A_2 = Coefficient of friction

K_1 = Fraction of concrete strength available to resist interface shear

K_2 = Limiting interface shear resistance

K_3 = Arbitrary stress value that allowed limits from the interface and the concrete strength to intersect.

K_4 = Upper limit based on the highest shear stress available in the database

Table 6-7: Prescribed values for cohesion factor, coefficient of friction and limit states for Eq. 6.4

Interface Type	A_1	A_2	K_1	K_2	K_3 (psi)	K_4 (psi)
Cold joint (Rough)	0.04	1.2	0.25	0.17	330	2000
Cold joint (Smooth)	0.02	0.75	0.13	-	-	1000

The shear friction equation proposed by Davaadorj [9] provided improved strength predictions throughout all types of specimens. All the measured-to-predicted strength ratios approached 1.0 and coefficient of variation decreased. However, similar to the AASHTO code, the upper stress limits were set too high, causing the model to overpredict the roughened specimens with high theoretical clamping stress. The upper stress limit is addressed in the thesis, stating that specimens with theoretical clamping stress great than 1,000 psi need to be tested to better calibrate the shear friction equation. The measured-to-predicted strength ratios obtained are shown in Table 6-8 and plotted in Figure 6.7.

Table 6-8: Average measured-to-predicted strength ratio of the model from Davaadorj [9]

Specimen Type	# of Specimens	Davaadorj	
		$\tau_{measured}/\tau_{predicted}$	CV (%)
CJ-S	20	1.27	20%
CJ-R	60	1.06	23%
CJ	80	1.11	23%

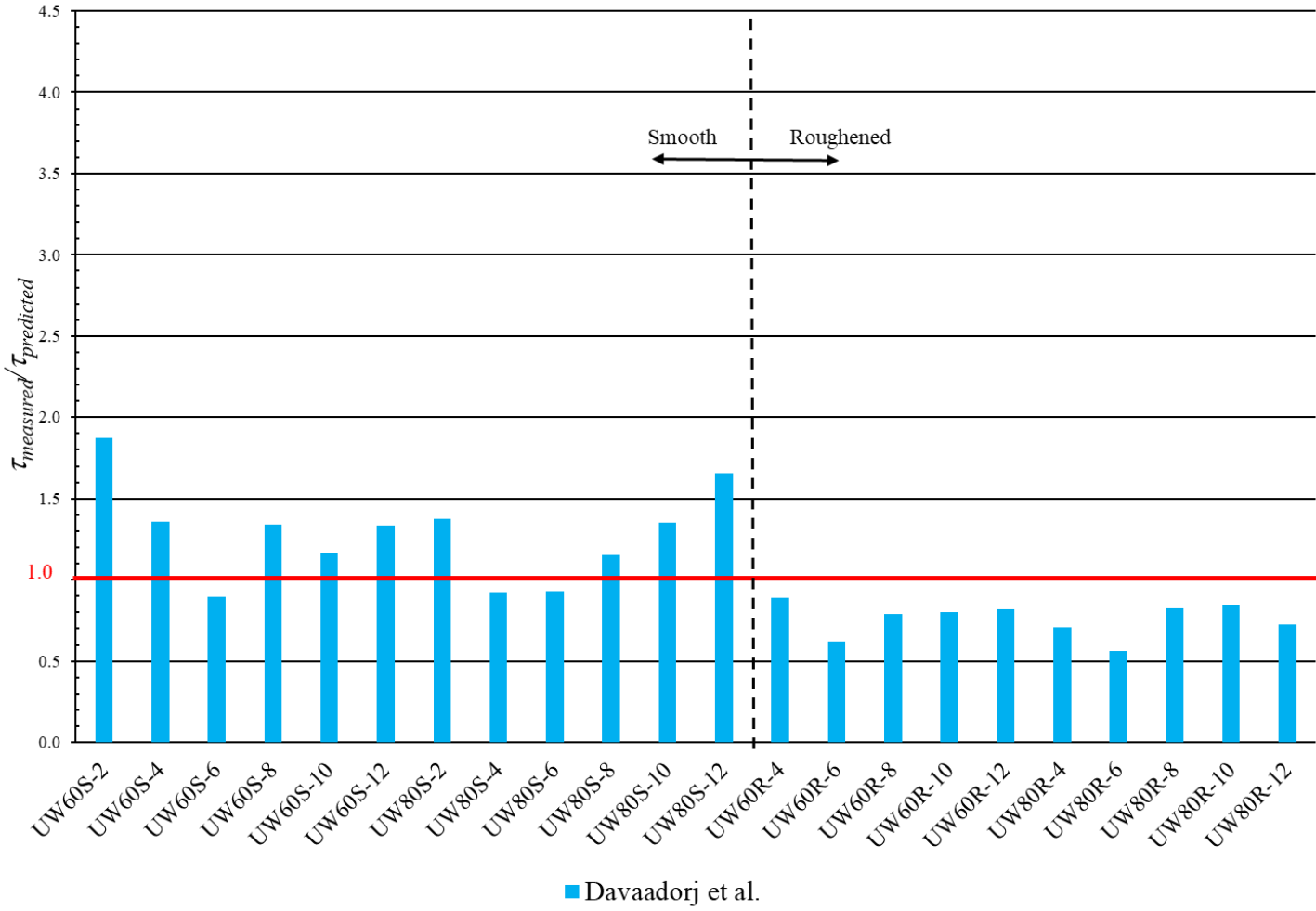


Figure 6.7: The average measured-to-predicted strength ratio of the model from Davaadorj [9] (UW specimens only)

6.4 Proposed Shear Friction Model

From the analysis of the experimental results regarding interface roughness, reinforcement ratio, and steel reinforcement strength in Chapter 5 and based on the evaluation of different shear friction models, a modified version of the model in Davaadorj [9] is proposed.

Models that included a separate cohesion term had a lower measured-to-predicted strength ratio than the shear friction equation from ACI. Findings suggesting the additive quality of cohesion to the peak shear-transfer capacity also meant that having a separate cohesion term is a better way to capture the specimen behavior. Of the three models that included a separate cohesion term, the model from Davaadorj [9] was the most accurate, aside from the fact that it overpredicted the roughened specimens with theoretical clamping stress beyond the upper stress limits. In terms of the upper stress limit, the model in ACI had the measured-to-predicted strength ratio closest to 1.0 without not falling below 1.0. The two shear friction models were combined to create the proposed shear friction shown below:

$$\begin{aligned}
 V_n &= cf'cA_{vc} + \mu A_{vf}F_y \\
 V_n &\leq K_1f'c, \\
 V_n &\leq K_2f'c + K_3 \\
 V_n &\leq K_4
 \end{aligned}
 \tag{Eq. 6.5}$$

Where,

c = Cohesion factor

μ = Coefficient of friction

K_1 = Fraction of concrete strength available to resist interface shear

K_2 = Limiting interface shear resistance

K_3 = Arbitrary stress value that allowed limits from the interface and the concrete strength to intersect.

K_4 = Upper limit based on the highest shear stress available in the database

Table 6-9: Prescribed values for cohesion factor, coefficient of friction and limit states for Eq. 6.5

Interface Type	c	μ	K_1	K_2	K_3 (psi)	K_4 (psi)
Cold joint (Rough)	0.03	1.0	0.20	0.08	480	1600
Cold joint (Smooth)	0.02	0.7	0.15	-	-	900

List of Changes from the model from Davaadorj [9]:

- The equation solves for the peak shear load, V_n , instead of the peak shear stress, τ_n
- The notation for the cohesion factor was changed from A_1 to c
- The notation for the coefficient of friction factor was changed from A_2 to μ
- The cohesion factor for roughened cold joint was changed from 0.04 to 0.03
- The coefficient of friction for smooth cold joint was changed from 0.75 to 0.7
- The K_1 -factor for roughened cold joint was lowered from 0.25 to 0.20
- The K_1 -factor for smooth cold joint was raised from 0.13 to 0.15
- The K_4 -factor for smooth cold joint was raised from 800 psi to 900 psi.
- The other K_2 , K_3 and K_4 -factors were changed to match upper stress limits in ACI for roughened cold joint.

The proposed shear friction equation was compared to the results from the database. The Table 6-10 below outlines the average measured-to-predicted strength ratio of three of the models discussed previously. The improvements to the overall predictions for all types of specimens are shown. The average measured-to-predicted ratio for roughened specimen is higher than the model from Davaadorj [9] because the proposed model no longer overpredicts the specimens with high theoretical clamping stresses. Even though the ratio is higher, the coefficient of variation is lower. The measured-to-predicted strength ratios obtained are charted in Figure 6.8.

Table 6-10 Table showing the measured-to-predicted strength ratio of the current ACI model and the proposed model.

Specimen Type	# of Specimens	ACI		Davaadorj		Proposed Model	
		$\tau_{measured}/\tau_{predicted}$	CV (%)	$\tau_{measured}/\tau_{predicted}$	CV (%)	$\tau_{measured}/\tau_{predicted}$	CV (%)
CJ-S	20	1.75	38%	1.27	20%	1.22	24%
CJ-R	60	2.00	57%	1.06	23%	1.34	21%
CJ	80	1.94	54%	1.11	23%	1.31	22%

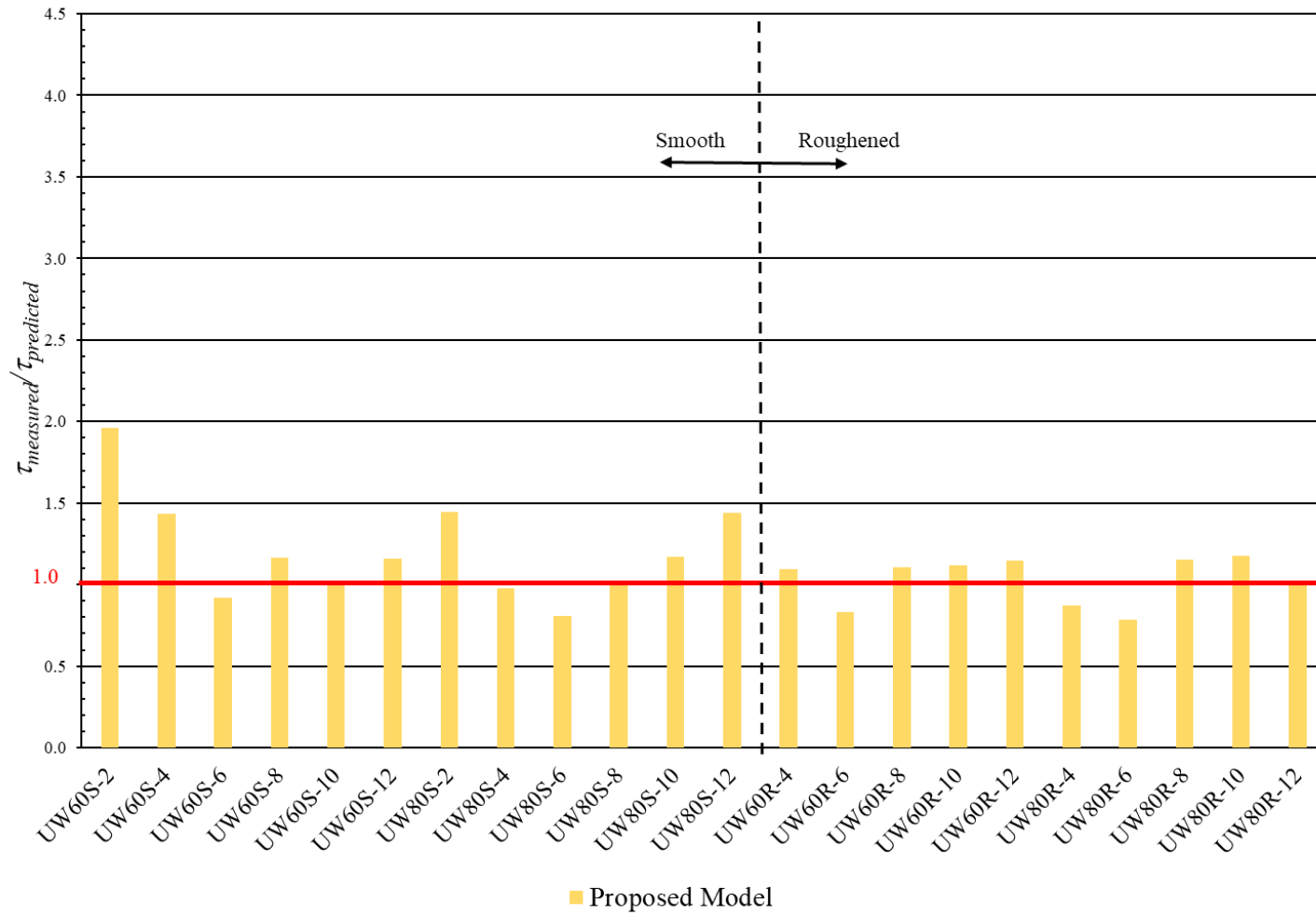


Figure 6.8: Chart showing the average measured-to-predicted strength ratio using the proposed model.

Chapter 7: Summary, Conclusion and Future Recommendation

7.1 Summary

This research program investigated the impact of interface roughness, reinforcement ratio and steel reinforcement strength, on the shear response of cold-joint specimens, using experimental methods. The results were combined with a previously compiled database to evaluate the accuracy of American codified expressions to estimate the shear strength of the interface. The data was used to develop a proposed equation that provides a better estimate of the shear strength for cold-joint specimens. The following summarizes the research approach.

- An initial study was undertaken to evaluate the interface roughening properties of different types of retarder.
- A total of 24 cold-joint specimens were designed and tested to investigate shear-transfer behavior. These specimens were divided into five test series, to study the following combinations of surface interface and reinforcement strength:
 - (1) Test Series 0: different surface roughness without reinforcement crossing an interface
 - (2) Test Series 60S: smooth interface with 60 ksi steel reinforcement crossing an interface
 - (3) Test Series 80S: smooth interface with 80 ksi steel reinforcement crossing an interface
 - (4) Test Series 60R: roughened interface with 60 ksi steel reinforcement crossing an interface.
 - (5) Test Series 80R: roughened interface with 80 ksi steel reinforcement crossing an interface.
- For each specimen, the total force-displacement response was measured. In addition, the reinforcing bar strains were monitored. This data was provided for each test.
- The experimental strength data were compared with ACI and AASHTO expressions for shear interface strength.
- A new expression, with a cohesion and a coefficient of friction was proposed and evaluated using a larger database.

7.2 Conclusions

The results of the research lead to the following conclusions:

- Roughness: roughening the interface of cold joints increases the peak shear-transfer capacity. To this end, using retarders appears to be an effective way of achieving adequate roughness levels.
- Yield Strength: the steel reinforcing bars through the interface did not yield in any of the specimens at the peak load. Therefore, steel reinforcement should be allowed to use in design for added practical benefits such as reducing reinforcement congestion.
- Upper stress limit: there appears to be an upper limit to the interface strength that is governed by the concrete properties and/or the interface properties and thus, independent of the steel reinforcement provided. The upper stress limits in ACI for smooth specimen was conservative, but the upper stress limits for roughened specimens appeared appropriate.
- Cohesion: the experimental results showed that different interface roughness affected the cohesion's contribution to the peak shear-transfer capacity. The difference in capacity caused by cohesion appeared to have an additive quality to the shear-transfer capacity. Thus, it was determined that shear interface equations with a separate cohesion term provide a better estimate of the strength.
- A new shear-friction equation is proposed that better predicts the peak shear-transfer capacity of both untreated (or smooth) and roughened cold-joint specimens. The new form of the equation is given below:

$$\begin{aligned}
 V_n &= cf'cA_{vc} + \mu A_{vf}F_y \\
 V_n &\leq K_1f'_c \\
 V_n &\leq K_2f'_c + K_3 \\
 V_n &\leq K_4
 \end{aligned}
 \tag{Eq. 7.1}$$

Where,

c = Cohesion factor

μ = Coefficient of friction

K_1 = Fraction of concrete strength available to resist interface shear

K_2 = Limiting interface shear resistance

K_3 = Arbitrary stress value that allowed limits from the interface and the concrete strength to intersect.

K_4 = Upper limit based on the highest shear stress available in the database

Table 7-1: Prescribed values for cohesion factor, coefficient of friction and limit states for Eq. 6.5

Interface Type	c	μ	K_1	K_2	K_3 (psi)	K_4 (psi)
Cold joint (Rough)	0.03	1.0	0.20	0.08	480	1600
Cold joint (Smooth)	0.02	0.7	0.15	-	-	900

7.3 Recommendations for Future Works: Interface Shear Transfer

- There was no consistency in how the roughness was achieved, measured, and reported between all the studies done on interface shear transfer. There is a need for developing a more methodical way of measuring, quantifying, and defining roughness.
- There is a need for a more accurate way of observing and capturing the local behavior of the reinforcement. Any data on the reinforcement crossing an interface is currently limited to the data from strain gauges attached one to two inches from the interface. Local yielding could occur at the peak load, but there is no way of quantifying it.
- Conduct further investigation on how different methods of roughening an interface affect the shear-transfer capacity (similar to the study done by Kono et al. [15] and Bass et al. [7] but including surface retarders). Interface treated with surface retarders could have lower shear-transfer capacity than interface roughened with jackhammers, meaning improved constructability could compromise the capacity.
- Conduct experimental tests of interface shear transfer using other types of specimens that better mimic real structural components. The current standardized push-off specimen does not accurately portray other structural components like the diaphragm-to-wall connections.
- Conduct experimental test of shear-friction specimens subjected to cyclic loading to create guidelines for designing for interface shear transfer under dynamic loading.
- Conduct further investigation on the post-peak mechanism. What mechanisms are contributing to the residual capacity is not clearly known. Investigating the post-peak mechanism can have huge implications on how interface shear transfer can be designed for dynamic loading.
- Create more numerical models of shear-friction cold-joint specimens. There currently is no prescriptive way of modeling a cold joint. Being able to accurately model the behavior of shear-friction specimens can lead to parametric studies using other concrete and reinforcement parameters (e.g. aggregate size, bar size, bar spacing, etc.).

References

- [1] AASHTO LRFD Bridge Design Specifications. 2007. American Association of State Highway and Transportation Officials, 4th edition, SI units edition, ISBN 1-56051-354-3, 1526 p.
- [2] ACI 318. 2011. Building Code Requirements for Structural Concrete (ACI 318-11) and Commentary, Committee 318, American Concrete Institute, PO Box 9094, Farmington Hills, MI 48333-9094, USA, 505 p.
- [3] ACI 318. 2019. Building Code Requirements for Structural Concrete (ACI 318-19) and Commentary, Committee 318, American Concrete Institute, PO Box 9094, Farmington Hills, MI 48333-9094, USA, 623 p.
- [4] ASTM A370-17. Standard Test Methods and Definitions for Mechanical Testing of Steel Products. Conshohocken, PA: ASTM International 2017.
- [5] ASTM C39/C39M-16. Standard Test Method for Compressive Strength of Cylindrical Concrete Specimens. ASTM International 2016.
- [6] Barbosa, A. R., Trejo, D., Nielson, D. 2017. "Effect of High-Strength Reinforcement steel on Shear Friction Behavior." *Journal of Bridge Engineering* 22.
- [7] Bass, R. A., Carrasquillo, R. L., and Jirsa, J. O. 1989. "Shear Transfer across New and Existing Interfaces." *ACI Structural Journal*, 86 (4): 383-393.
- [8] Birkeland, P. W., and Birkeland, H. W. 1966. "Connections in Precast Concrete Construction." *ACI Journal Proceedings*, Vol. 63, No. 3, pp. 345-368.
- [9] Davaadorj, O. 2018. "Shear Stress Transfer across Concrete-to-Concrete and Steel-to-Concrete Interfaces." Master's Dissertation, Department of Civil and Environmental Engineering, University of Washington, p, 264.
- [10] Davaadorj, O., Calvi, P. M., and Stanton, J. F. 2020. "Shear Stress Transfer across Concrete-Concrete Interfaces: Experimental Evidence and Available Strength Models." *PCI Journal*. July-August Issue. In Press.
- [11] Hanson, N. W. 1960. "Precast-Prestressed Concrete Bridges – 2 Horizontal Shear Connections." *Journal PCA Research and Development Laboratories* 2 (2): 345-368.
- [12] Harries, K. A., Zeno, G., Shahrooz, B. 2017. "Toward and Improved Understanding of Shear-Friction Behavior." *ACI Structural Journal* 109 (6): 835-843.

- [13] Hofbeck, J. A., I. O. Ibrahim, and A.H. Mattock. 1969. "Shear Transfer in Reinforced Concrete." *Journal of the American Concrete Institute* 66 (2): 119-128.
- [14] Kahn, L .F. and A. D. Mitchell. 2002. "Shear Friction Tests with High Strength Concrete." *ACI Structural Journal* 99 (1): 98-103.
- [15] Kono, S., Tanaka, H., and Watanabe, F. 2001. "Interface Shear Transfer for High Strength Concrete and High Strength Shear Friction Reinforcement." International Conference on High Performance Materials in Bridges, Kona, Hawaii, United States, pp. 319-328.
- [16] Loov, R. E., and Patnaik, A. K. 1994. "Horizontal Shear Strength of Composite Concrete Beams with a Rough Interface." *PCI Journal*, 39 (1): 48-69.
- [17] Mattock, A. H., and N. M. Hawkins. 1972. "Shear Transfer in Reinforced Concrete – Recent Research." *PCI Journal* 17 (2): 55-75.
- [18] Mattock, A. H. 1976. "Shear Transfer under Monotonic Loading Across an Interface Between Concretes Cast at Different Times." Department of Civil Engineering report SM 76-3. Seattle, WA: University of Washington.
- [19] Mattock, A. H., 1977. "Considerations for the Design of Precast Concrete Bearing Wall Buildings to Withstand Abnormal Loads." *PCI Journal* 22 (3): 105-106.
- [20] Moehle, Jack P., Hooper, John D., Kelly, Dominic J., and Meyer, Thomas R. (2010). "Seismic Design of Cast-in-Place Concrete Diaphragms, Chords, and Collectors: a Guide for Practicing Engineers,". *NEHRP Seismic Design Technical Brief No. 3*, produced by the NEHRP Consultants Joint Venture, a partnership of the Applied Technology Council and the Consortium of Universities for Research in Earthquake Engineering, for National Institute of Standard and Technology, Gaithersburg, MD, NIST GCR 10-917-4
- [21] Precast/Prestressed Concrete Institute. 2010. *PCI Design Handbook: Precast and Prestressed Concrete Institute. 7th ed*, Chicago: Precast/Prestressed Concrete Institute.
- [22] Shaw, D., and Sneed, L. J. 2014. "Interface Shear Transfer of Lightweight- Aggregate Concrete Cast at Different Times." *PCI Journal*, 59 (3): 130-144.
- [23] Walraven, J. C., and Reinhardt, H.W. 1981. "Theory and Experiments on the Mechanical Behavior of Cracks in Plain and Reinforced Concrete Subjected to Shear Loading." *HERON* 26 (1A): 1-68.

Appendix A: Figures and Tables

Appendix A-1: Experimental results from the database created by Davaadorj [9] with the inclusion of the UW specimens

Author1	Author2	Year	Surf	d_s (in)	ρ	f_y (ksi)	ρf_y (psi)	f'_c (psi)	τ_{peak} (psi)	w_{peak} (in)	Δ_{peak} (in)	$\mu \epsilon_{peak}$
Sneed	Shaw	2013	S	0.375	1.3	66.2	883	4860	661	0.015	0.057	1756
Sneed	Shaw	2013	S	0.375	1.3	66.2	883	4860	701	0.008	0.022	1317
Sneed	Shaw	2013	S	0.375	1.3	66.2	883	4860	791	0.007	0.031	4107
Sneed	Shaw	2013	S	0.375	1.3	66.2	883	7550	1325	0.006	0.010	2136
Sneed	Shaw	2013	S	0.375	1.3	66.2	883	7550	1077	0.005	0.010	2288
Sneed	Shaw	2013	S	0.375	1.3	66.2	883	7550	1118	0.006	0.001	2167
Kahn	Mitchell	2002	S	0.375	0.4	83.0	332	14326	529	N/A	0.009	N/A
Kahn	Mitchell	2002	S	0.375	0.7	83.0	581	12053	822	N/A	0.010	N/A
Jose		1998	S	N/A	N/A	N/A	N/A	7536	304	N/A	N/A	N/A
Jose		1998	S	N/A	N/A	N/A	N/A	6392	258	N/A	N/A	N/A
Jose		1998	S	N/A	N/A	N/A	N/A	5347	448	N/A	N/A	N/A
Jose		1998	S	N/A	N/A	N/A	N/A	6324	388	N/A	N/A	N/A
CTA		1974	S	N/A	N/A	N/A	N/A	5500	429	N/A	N/A	N/A
CTA		1974	S	N/A	N/A	N/A	N/A	4060	398	N/A	N/A	N/A
CTA		1976	S	N/A	N/A	N/A	N/A	4340	295	N/A	N/A	N/A
CTA		1976	S	N/A	N/A	N/A	N/A	4300	100	N/A	N/A	N/A
CTA		1976	S	N/A	N/A	N/A	N/A	4900	231	N/A	N/A	N/A
CTA		1976	S	N/A	N/A	N/A	N/A	3820	84	N/A	N/A	N/A
CTA		1976	S	N/A	N/A	N/A	N/A	4090	136	N/A	N/A	N/A
CTA		1976	S	N/A	N/A	N/A	N/A	3970	109	N/A	N/A	N/A
CTA		1976	S	N/A	N/A	N/A	N/A	3420	89	N/A	N/A	N/A
Calvi	Lehman	2020	S	0.625	0.4	74.4	290	5651	619	0.0008	0.008	133
Calvi	Lehman	2020	S	0.625	0.8	74.4	580	5651	745	0.0064	0.014	844
Calvi	Lehman	2020	S	0.625	1.2	74.4	863	5651	659	0.0116	0.037	1030
Calvi	Lehman	2020	S	0.625	1.6	74.4	1153	5651	985	0.0059	0.025	637
Calvi	Lehman	2020	S	0.625	1.9	74.4	1443	5651	854	0.0117	0.029	893
Calvi	Lehman	2020	S	0.625	2.3	74.4	1734	5651	980	0.0107	0.035	910
Calvi	Lehman	2020	S	0.625	0.4	98.1	383	5651	551	0.0023	0.006	317
Calvi	Lehman	2020	S	0.625	0.8	98.1	765	5651	633	0.0176	0.049	2311
Calvi	Lehman	2020	S	0.625	1.2	98.1	1138	5651	686	0.0163	0.040	1425
Calvi	Lehman	2020	S	0.625	1.6	98.1	1521	5651	847	0.0130	0.042	1158
Calvi	Lehman	2020	S	0.625	1.9	98.1	1903	5651	992	0.0129	0.027	1039
Calvi	Lehman	2020	S	0.625	2.3	98.1	2286	5651	1219	0.0081	0.040	1181
Calvi	Lehman	2020	S	N/A	N/A	N/A	N/A	5850	258	0.0003	0.008	N/A
Miller	Harries	2011	R	0.375	0.4	67.3	277	5800	700	0.008	0.025	238
Miller	Harries	2011	R	0.375	0.4	67.3	272	5800	590	0.007	0.027	405
Miller	Harries	2011	R	0.500	0.7	61.5	447	5800	690	0.009	0.037	515
Miller	Harries	2011	R	0.500	0.7	61.5	454	5800	790	0.008	0.038	410
Miller	Harries	2011	R	0.375	0.4	130.0	545	5800	570	0.007	0.027	222

Miller	Harries	2011	R	0.375	0.4	126.0	517	5800	650	0.008	0.031	527
Miller	Harries	2011	R	0.500	0.7	140.0	1034	5800	840	0.008	0.032	529
Miller	Harries	2011	R	0.500	0.7	131.3	980	5800	710	0.010	0.041	579
Sneed	Shaw	2013	R	0.375	1.3	66.2	883	4860	1193	0.007	0.013	2100
Sneed	Shaw	2013	R	0.375	1.3	66.2	883	4860	1079	0.006	0.010	1724
Sneed	Shaw	2013	R	0.375	1.3	66.2	883	4860	1080	0.007	0.012	1505
Sneed	Shaw	2013	R	0.375	1.3	66.2	883	7550	1496	0.008	0.010	2394
Sneed	Shaw	2013	R	0.375	1.3	66.2	883	7550	1133	0.005	0.008	1788
Sneed	Shaw	2013	R	0.375	1.3	66.2	883	7550	1296	0.005	0.007	2758
Kahn	Mitchell	2002	R	0.375	0.4	83.0	332	11734	900	N/A	N/A	N/A
Kahn	Mitchell	2002	R	0.375	0.7	83.0	581	11734	1368	N/A	0.028	N/A
Kahn	Mitchell	2002	R	0.375	1.1	83.0	913	12471	1838	N/A	0.054	N/A
Kahn	Mitchell	2002	R	0.375	1.5	83.0	1245	12471	2211	N/A	0.062	N/A
Kahn	Mitchell	2002	R	0.375	1.1	83.0	913	12953	1899	N/A	0.070	N/A
Kahn	Mitchell	2002	R	0.375	1.5	83.0	1245	12953	2101	N/A	0.061	N/A
Kahn	Mitchell	2002	R	0.375	0.4	83.0	332	14756	1515	N/A	0.052	N/A
Kahn	Mitchell	2002	R	0.375	0.7	83.0	581	14756	1653	N/A	0.059	N/A
Kahn	Mitchell	2002	R	0.375	1.1	83.0	913	15218	2245	N/A	0.074	N/A
Kahn	Mitchell	2002	R	0.375	1.5	83.0	1245	15218	2552	N/A	2.328	N/A
Jose		1998	R	N/A	N/A	N/A	N/A	5540	370	N/A	N/A	N/A
Jose		1998	R	N/A	N/A	N/A	N/A	5816	242	N/A	N/A	N/A
Jose		1998	R	N/A	N/A	N/A	N/A	5789	416	N/A	N/A	N/A
Jose		1998	R	N/A	N/A	N/A	N/A	5309	246	N/A	N/A	N/A
Jose		1998	R	N/A	N/A	N/A	N/A	5788	216	N/A	N/A	N/A
Jose		1998	R	N/A	N/A	N/A	N/A	5352	280	N/A	N/A	N/A
Jose		1998	R	N/A	N/A	N/A	N/A	5613	292	N/A	N/A	N/A
Jose		1998	R	N/A	N/A	N/A	N/A	6387	620	N/A	N/A	N/A
Jose		1998	R	N/A	N/A	N/A	N/A	6641	560	N/A	N/A	N/A
CTA		1976	R	N/A	N/A	N/A	N/A	4900	280	N/A	N/A	N/A
CTA		1976	R	N/A	N/A	N/A	N/A	3820	149	N/A	N/A	N/A
CTA		1976	R	N/A	N/A	N/A	N/A	4090	199	N/A	N/A	N/A
CTA		1976	R	N/A	N/A	N/A	N/A	3970	230	N/A	N/A	N/A
Scott		2010	R	N/A	N/A	N/A	N/A	6150	398	N/A	0.035	N/A
Scott		2010	R	N/A	N/A	N/A	N/A	6150	417	N/A	0.035	N/A
Scott		2010	R	N/A	N/A	N/A	N/A	6150	406	N/A	0.055	N/A
Scott		2010	R	0.500	0.1	60.0	63	6150	320	N/A	0.050	145
Scott		2010	R	0.500	0.1	60.0	63	6150	367	N/A	0.045	103
Scott		2010	R	0.500	0.1	60.0	63	6150	451	N/A	0.060	103
Scott		2010	R	0.625	0.5	60.0	288	6150	508	N/A	0.105	N/A
Scott		2010	R	0.625	0.5	60.0	288	6150	568	N/A	0.095	662
Scott		2010	R	0.625	0.5	60.0	288	6150	596	N/A	0.085	N/A
Barbosa	Trejo	2017	R	0.500	0.4	72.6	303	4481	727	0.040	0.047	1950
Barbosa	Trejo	2017	R	0.500	0.4	72.6	303	4481	668	0.035	0.042	1475
Barbosa	Trejo	2017	R	0.500	0.4	72.6	303	4198	637	note	0.050	2000

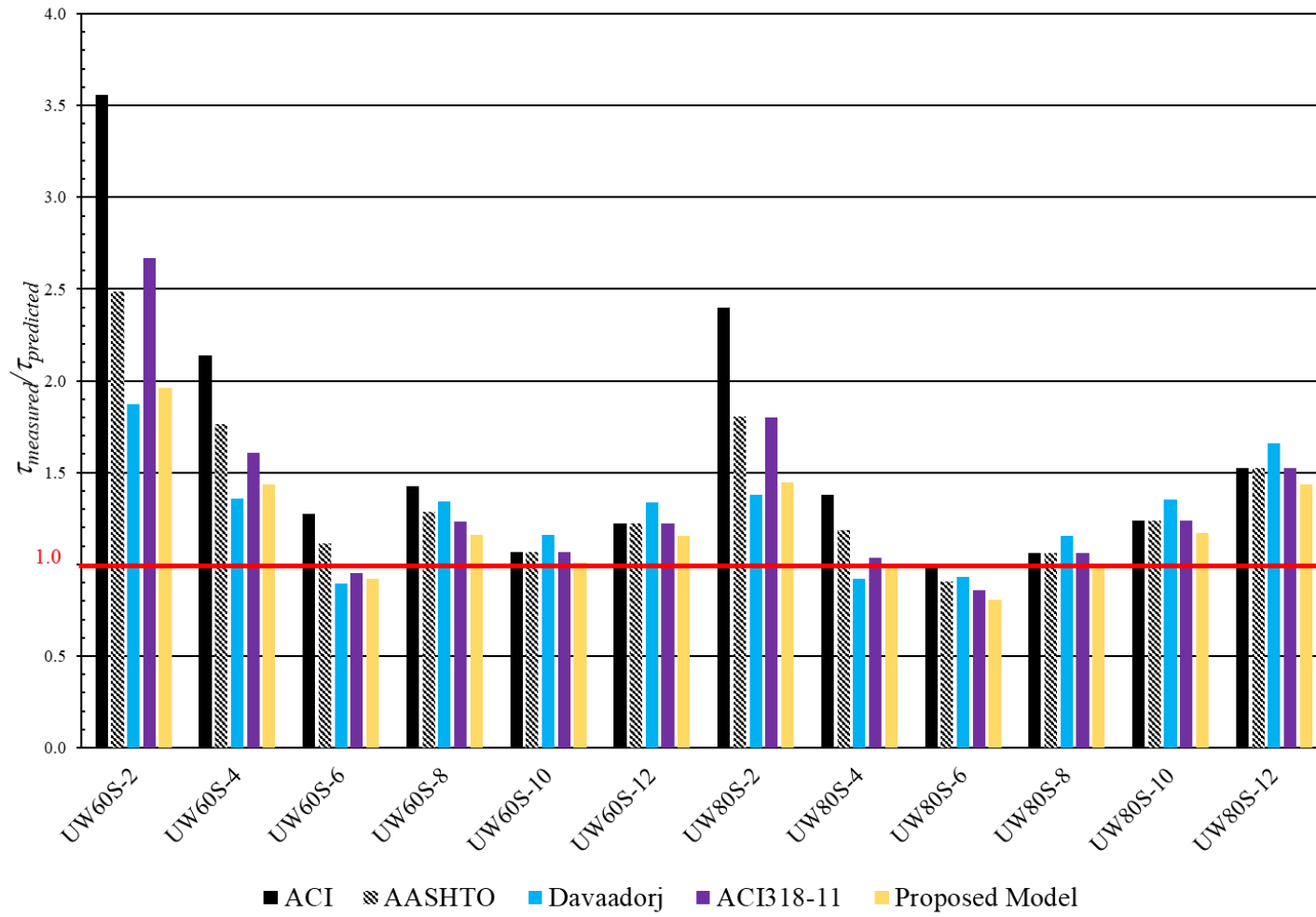
Barbosa	Trejo	2017	R	0.500	0.4	72.6	303	4198	688	0.03	0.039	1425
Barbosa	Trejo	2017	R	0.500	0.4	72.6	303	4198	703	note	0.042	1600
Barbosa	Trejo	2017	R	0.500	0.4	93.0	388	4372	606	N/A	0.032	N/A
Barbosa	Trejo	2017	R	0.500	0.4	93.0	388	4198	634	0.018	note	1400
Barbosa	Trejo	2017	R	0.500	0.4	93.0	388	4198	658	0.044	0.047	1550
Barbosa	Trejo	2017	R	0.500	0.4	93.0	388	4198	683	0.029	0.044	2075
Barbosa	Trejo	2017	R	0.500	0.4	93.0	388	4198	757	0.035	0.044	1675
Barbosa	Trejo	2017	R	0.625	0.6	67.6	437	4578	949	0.036	0.063	5557
Barbosa	Trejo	2017	R	0.625	0.6	67.6	437	4578	958	0.047	0.067	5833
Barbosa	Trejo	2017	R	0.625	0.6	67.6	437	4149	963	0.042	0.074	5187
Barbosa	Trejo	2017	R	0.625	0.6	67.6	437	4149	945	0.033	0.058	5073
Barbosa	Trejo	2017	R	0.625	0.6	67.6	437	4149	955	0.042	0.063	5907
Barbosa	Trejo	2017	R	0.625	0.6	86.8	561	4578	1048	0.043	0.072	4233
Barbosa	Trejo	2017	R	0.625	0.6	86.8	561	4149	1061	0.046	0.068	4103
Barbosa	Trejo	2017	R	0.625	0.6	86.8	561	4149	1085	0.040	0.065	4480
Barbosa	Trejo	2017	R	0.625	0.6	86.8	561	4149	981	0.033	0.058	4727
Barbosa	Trejo	2017	R	0.625	0.6	86.8	561	4149	1032	0.040	0.073	3310
Calvi	Lehman	2020	R	0.625	0.8	74.4	580	5850	827	0.0145	0.026	923
Calvi	Lehman	2020	R	0.625	1.2	74.4	863	5850	790	0.0040	0.011	744
Calvi	Lehman	2020	R	0.625	1.6	74.4	1153	5850	1049	0.0093	0.021	1038
Calvi	Lehman	2020	R	0.625	1.9	74.4	1443	5850	1060	0.0055	0.022	938
Calvi	Lehman	2020	R	0.625	2.3	74.4	1734	5850	1087	0.0062	0.022	846
Calvi	Lehman	2020	R	0.625	0.8	98.1	765	5850	819	0.0123	0.015	758
Calvi	Lehman	2020	R	0.625	1.2	98.1	1138	5850	744	0.0017	0.005	677
Calvi	Lehman	2020	R	0.625	1.6	98.1	1521	5850	1092	0.0222	0.039	1178
Calvi	Lehman	2020	R	0.625	1.9	98.1	1903	5850	1118	0.0097	0.023	1057
Calvi	Lehman	2020	R	0.625	2.3	98.1	2286	5850	962	0.0037	0.014	963
Calvi	Lehman	2020	R	N/A	N/A	N/A	N/A	5850	422	0.0003	0.002	N/A

Appendix A-2: Average strain of the reinforcing bars at residual load

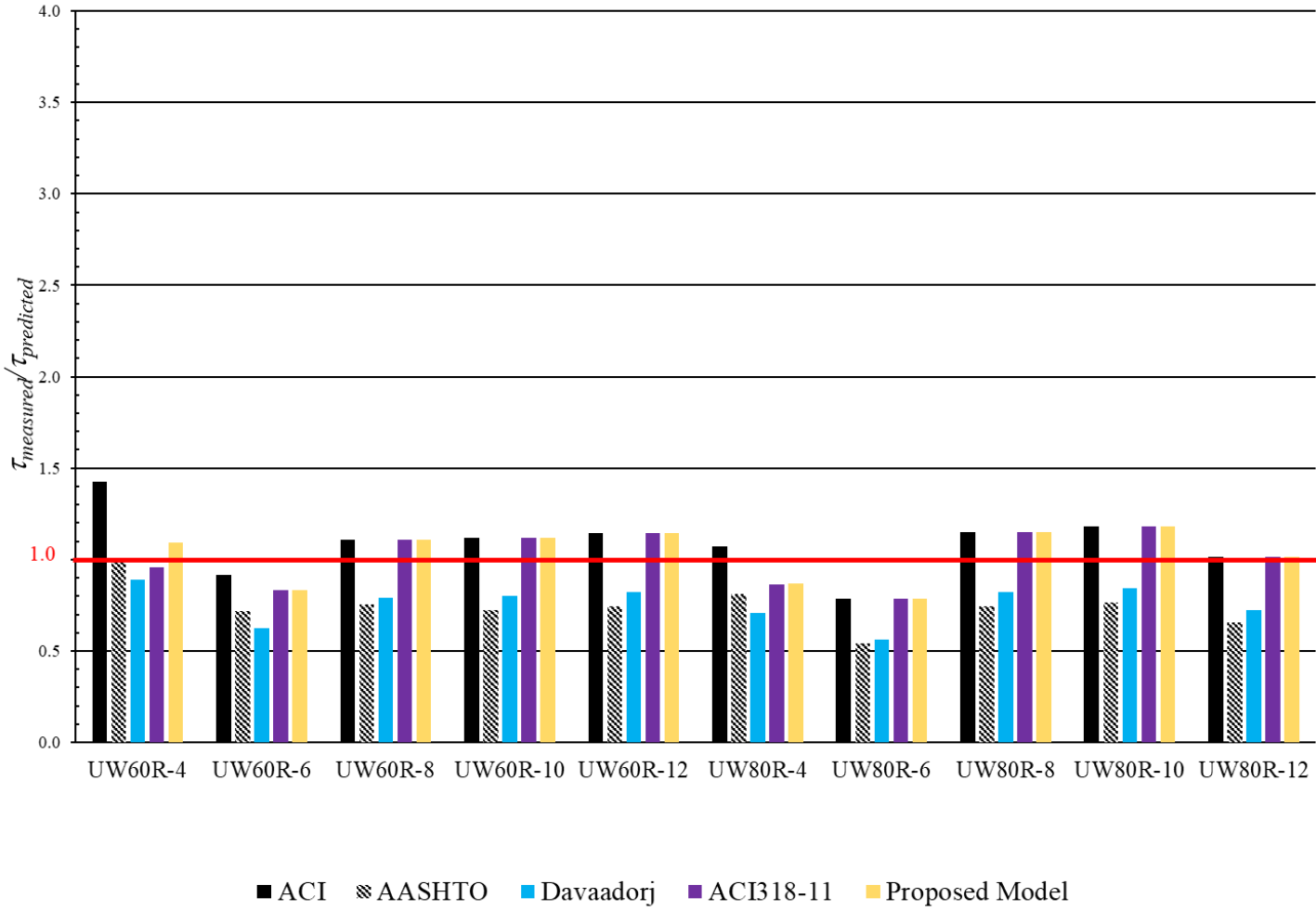
Specimen	f_y (ksi)	ϵ_y	Avg. $\epsilon_{residual}$
UW60S-2			N/A
UW60S-4			N/A
UW60S-6	74.4	0.0058	N/A
UW60S-8			0.0025
UW60S-10			N/A
UW60S-12			N/A
UW80S-2			N/A
UW80S-4			N/A
UW80S-6	98.1	0.0040	N/A
UW80S-8			0.0017
UW80S-10			N/A
UW80S-12			N/A
UW60R-4			N/A
UW60R-6			0.0031
UW60R-8	74.4	0.0058	0.0020
UW60R-10			0.0037
UW60R-12			0.0020
UW80R-4			0.0047
UW80R-6			0.0046
UW80R-8	98.1	0.0040	0.0023
UW80R-10			0.0028
UW80R-12			0.0030

Appendix A-3: Measured-to-predicted strength ratio of all the shear friction models discussed before. UW specimens only.

Specimen	$\tau_{\text{measured}}/\tau_{\text{predicted}}$				
	ACI	AASHTO	Davaadorj	ACI318-11	Proposed
UW60S-2	3.56	2.49	1.87	2.67	1.96
UW60S-4	2.14	1.76	1.36	1.61	1.44
UW60S-6	1.27	1.11	0.90	0.95	0.92
UW60S-8	1.42	1.28	1.34	1.23	1.16
UW60S-10	1.07	1.07	1.16	1.07	1.01
UW60S-12	1.23	1.23	1.33	1.23	1.16
UW80S-2	2.40	1.81	1.38	1.80	1.45
UW80S-4	1.38	1.19	0.92	1.03	0.98
UW80S-6	1.00	0.90	0.93	0.86	0.81
UW80S-8	1.06	1.06	1.15	1.06	1.00
UW80S-10	1.24	1.24	1.35	1.24	1.17
UW80S-12	1.52	1.52	1.66	1.52	1.44
UW60R-4	1.43	1.01	0.89	0.96	1.09
UW60R-6	0.92	0.72	0.62	0.83	0.83
UW60R-8	1.11	0.75	0.79	1.11	1.11
UW60R-10	1.12	0.72	0.80	1.12	1.12
UW60R-12	1.15	0.74	0.82	1.15	1.15
UW80R-4	1.07	0.81	0.71	0.86	0.87
UW80R-6	0.78	0.54	0.56	0.78	0.78
UW80R-8	1.15	0.75	0.82	1.15	1.15
UW80R-10	1.18	0.76	0.84	1.18	1.18
UW80R-12	1.01	0.66	0.73	1.01	1.01



Appendix A-4: Measured-to-predicted strength ratio of all the models discussed before. Smooth UW specimens only.



Appendix A-5: Measured-to-predicted strength ratio of all the models discussed before. Roughened UW specimens only.



Appendix A-6: Half of the reinforcement cage constructed



Appendix A-7: Photograph of UW0R before cast.



Appendix A-8: Photograph of UW60R-4 before cast.



Appendix A-9: Photograph of UW60R-4 and UW0R after first half was cast. The interfaces were treated with retarders.



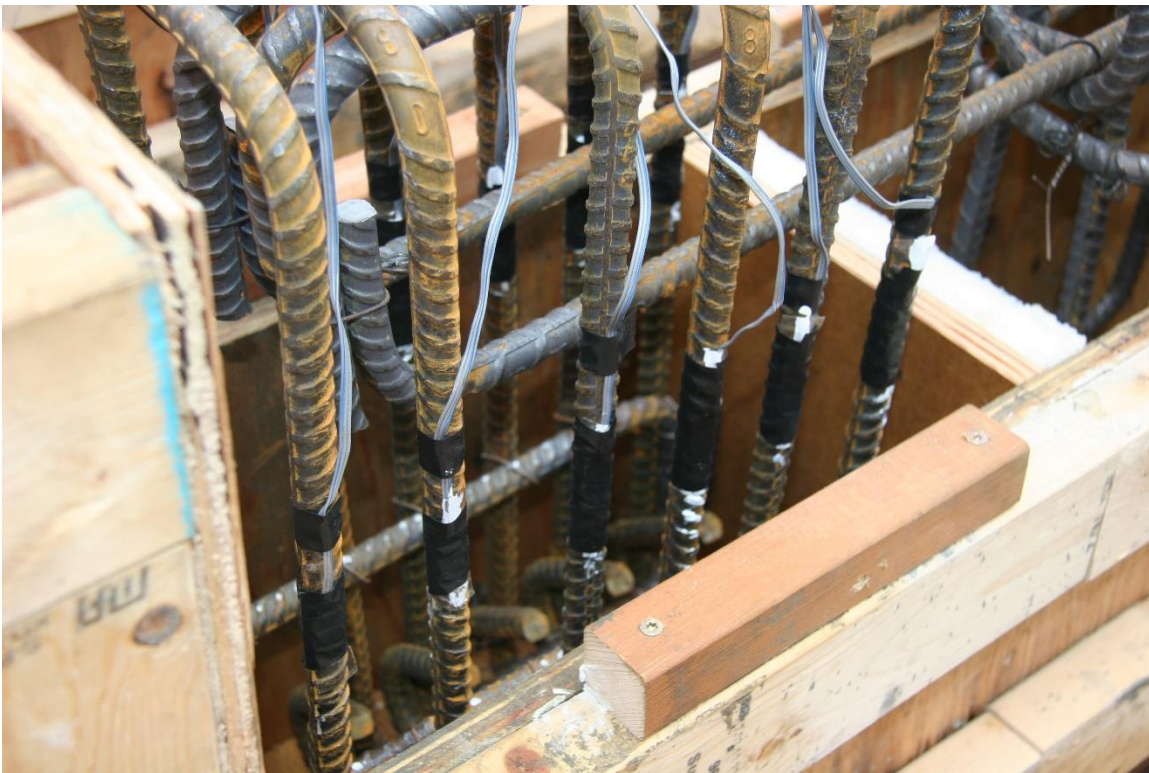
Appendix A-10: Surface of UW0R.



Appendix A-11: Surface of UW60R-4.



Appendix A-12: Surface of UW80R-8.



Appendix A-13: Photograph of strain gauges on UW80R-12



Appendix A-14: Photograph of UW60R-4 before second half was cast.



Appendix A-15: Photograph showing reinforcement congestion at a diaphragm-to-wall connection. Bigger reinforcing bars are collectors. Smaller reinforcing bars are shear friction reinforcement [20].